Transmission electron microscopy study of heterostructures grown on GaAs (110)

D i s s e r t a t i o n

zur Erlangung des akademischen Grades

d o c t o r r e r u m n a t u r a l i u m
(Dr. rer. nat.)
im Fach Physik

eingereicht an der
Mathematisch-Naturwissenschaftlichen Fakultät I
der Humboldt-Universität zu Berlin

von
Herrn M.Sc. Qian Wan
Chongqing, China

Präsident der Humboldt-Universität zu Berlin:
Prof. Dr. Jan-Hendrik Olbertz

Dekan der Mathematisch-Naturwissenschaftlichen Fakultät I:
Prof. Stefan Hecht, Ph.D.

Gutachter:
1. Prof. Dr. Henning Riechert
2. Prof. Dr. Thomas Schroeder
3. Prof. Dr. W. Ted Masselink

eingereicht am: 15.02.2013
Tag der mündlichen Prüfung: 29.04.2014

Abstract

In the work, we systematically investigate the microstructural properties of (110) oriented heterostructures on GaAs substrates by means of different transmission electron microscopy techniques. Three heterosystems are investigated as case studies including (Al,Ga)As/GaAs, MnAs/GaAs and CoAl/GaAs. These selected material systems cover three major lattice symmetries, i.e. fcc, hcp and bcc, and they differ from each other not only in the lattice mismatches with respect to GaAs(110), but also in their crystalline phases, from semiconductor compound over half-metal to metallic alloy. In order to verify the epitaxial alignment for the different cases, detailed investigations of the interfaces are carried out, including the atomic arrangements, the defect properties and the resulting strain states. The effect of different interface configurations on the microstructural properties of the layer is also researched.

Fcc-type (Al,Ga)As/AlAs/GaAs multilayer structure on GaAs (110) presents different mismatch strain accommodation mechanisms along the perpendicular in-plane directions. With the introduction of short period superlattices, pseudomorphical growth is realized far beyond the critical thickness. Defect-free structures are successfully acquired by an appropriate type of AlAs/GaAs short period superlattice. Finally, artificial defects are intentionally produced by nano-indentation to the defect-free sample to verify the effect of short period superlattices.

Hcp-type MnAs on GaAs (110) system is characterized by anisotropic lattice mismatches of -7.5% and 0.7% along the $[11\bar{2}0]$ and [0001] direction, respectively. A wetting layer is observed prior to the formation of islands, indicating a Stranski-Krastanov growth mode of MnAs. The strain corresponding to the 0.7% lattice misfit is accommodated elastically, whereas the mismatch stress along perpendicular direction is relived by the formation of a periodic array of perfect misfit dislocations with a stand-off position in MnAs lattice. The long range strain field associated with the dislocation array is constrained at the interface within a thickness of about 3.4 nm. An interfacial atomic configuration is also proposed based on the comparison between HRTEM image and the simulations. In addition, subsequent growth of GaAs on MnAs is three-dimensional with a huge amount of planar defects present.

B2-type intermetallic CoAl alloys are realized on (001) and (110) oriented GaAs substrates for comparison. They are both characterized by a coexistence of B2 phase and its disordered version bcc phase. The disordering is induced partially by the epitaxial strain and partially by the diffusion of point defects. Additionally, (110) oriented CoAl presents a large number of misoriented domains originated from the interface roughness. They further reduce the volume fraction of the ordered B2 phase.

The three case studies have pointed out the specific relevance of interfaces for the realization of tailored heterosystems and their resultant microstructure. The interface determines the epitaxial orientation geometry between the substrate and the epilayer, and accordingly the lattice mismatches along different in-plane directions as well as the specific ways of mismatch strain relaxation. Interface structure in a heterosystem generally describes a low-energy atom configuration, which is driven by the minimization of strain energy.

Keywords: Microstructure, interface, TEM, GaAs(110)

Zusammenfassung

In der Arbeit werden die mikrostrukturellen Eigenschaften von an (110)-Flächen orientierten Heterostrukturen auf GaAs-Substraten mittels verschiedener Techniken der Transmissionselektronenmikroskopie untersucht. Drei Heterosysteme sind exemplarisch betrachtet worden: (Al,Ga)As/GaAs, MnAs/GaAs und CoAl/GaAs. Diese gewählten Materialsysteme gehören zu drei Hauptgittersymmetrien-kubisch flächenzentriert (fcc), hexagonal dicht gepackt (hcp) und kubisch raumzentriert. Sie unterscheiden sich neben den Gitterfehlanpassungen bezogen auf GaAs(110) auch in ihren kristallinen Phasen, die von Verbindungshalbleitern über Halbmetalle bis zu metallischen Legierungen reichen. Um die epitaktische Beziehung in den verschiedenen Fällen zu verifizieren, sind detaillierte Untersuchungen der Grenzfläche durchgeführt worden, was die atomare Struktur, die Defekteigenschaften und den resultierenden Dehnungszustand beinhaltet. Der Einfluss der verschiedenen Grenzflächenkonfigurationen auf die Mikrostruktur der Schichten wird ebenfalls betrachtet.

Kubisch flächenzentrierte (Al,Ga)As/AlAs/GaAs Mehrschichtstrukturen auf GaAs (110) weisen in orthogonalen Richtungen parallel zur Substratoberfläche verschiedene Mechanismen zur Aufnahme der Verspannungen aufgrund von Fehlanpassungen auf. Durch kurzperiodische Übergitter wird ein pseudomorphes Wachstum weit über die kritische Dicke hinaus ermöglicht. Defektfreie Strukturen sind durch eine geeignete, kurz periodische AlAs/GaAs-Überstruktur erfolgreich realisiert worden. Abschließend sind künstliche Defekte per Nanoindentation in den defektfreien Proben erzeugt worden, um die Auswirkung kurzperiodischer Übergitter zu prüfen.

Das System aus hexagonal dicht gepacktem MnAs auf GaAs(110) zeichnet sich durch anisotrope Gitterfehlanpassung von -7.5% und 0.7% entsprechend der $[11\bar{2}0]$ und der [0001] Richtungen aus. Eine Benetzungsschicht, die der Entstehung von Inseln vorausgeht, wird beobachtet, was das Stranski-Krastanov-Wachstum von MnAs belegt. Die Dehnung durch die Gitterfehlpassung von 0.7% wird elastisch eingebaut, während die Spannung durch die Gitterfehlanpassung in der senkrechten Richtung durch die Entstehung einer periodischen Anordnung, vollständiger Gitterfehlanpassungsversetzungen abgebaut wird, die sich von der Grenzfläche entfernt im MnAs-Gitter befinden. Das aus der Versetzungsanordnung resultierende Dehnungsfeld ist auf eine Dicke von 3.4 nm um die Grenzfläche beschränkt. Eine atomare Struktur der Grenzfläche wird basierend auf dem Vergleich von HRTEM-Aufnahmen und Simulationen vorgeschlagen. Ferner stellt sich das anschließende Wachstum von GaAs auf MnAs als dreidimensional dar, wobei eine große Menge planarer Defekte auftritt.

Intermetallische CoAl-Legierungen in der B2-Phase sind zum Vergleich auf (001) und auf (110) orientierten GaAs-Substraten hergestellt worden. Beide Fälle weisen die Koexistenz der B2-Phase und der ungeordneten, kubisch raumzentrierten Variante auf. Die Unordnung wird teilweise durch die epitaktische Dehnung und teilweise durch Diffusion von Punktdefekten hervorgerufen. Außerdem zeigt CoAl in der (110)-Orientierung eine Vielzahl nicht ausgerichteter Domänen, was von der Grenzflächenrauigkeit herrührt. Des Weiteren verringern sie den Volumenanteil der geordneten B2-Phase.

Die drei Fallstudien belegen eindeutig die besondere Bedetung von Grenzflächen für die Bildung von massgeschneiderten Heterosystemen und ihrer resultierenden Mikrostruktur. Die Grenzfläche bestimmt die epitaktische Orientierungsbeziehung zwischen Substrat und Schicht, und legt folglich die Gitterfehlanpasssung entlang der verschiedenen in-plane Richtungen fest, sowie die Art und Weise des Spannungsabbaus. Üblicherweise beschriebt die Grenzflächenstruktur dabei eine nieder- energetische Atomkonfiguration, die durch die Minimierung der Dehnungsenergie beschrieben ist.

Stichwörte: Mikrostruktur, Grenzfläche, TEM, GaAs(110)

Abbreviations

2D/3D	Two dimensional/three dimensional
AFM	Atomic force microscope
bcc	Body centered cubic
CSL	Coincidence site lattice
DBR	Distributed Bragg reflector
fcc	Face centered cubic
FM	Frank-Van der Merwe
hcp	Hexagonal close packed
HR	High resolution
LED	Light emitting diode
NBD	Nanobeam diffraction
MB	Matthews and Blakeslee
MBE	Molecular beam epitaxy
MD	Misfit dislocation
MDM	Misoriented domain
MOSFET	Metal oxide semiconductor field effect transistor
PD	Planar defect
RHEED	Reflection high-energy electron diffraction
SAED	Selected-area electron diffraction
SPSL	Short period superlattice
SF	Stacking fault
SK	Stranski- Krastanov
TEM	Transmission electron microscopy
TD	Threading dislocation
UHV	Ultra high vacuum
VCSEL	Vertical-cavity surface emitting lasers
VW	Volmer-Weber
XRD	X-ray diffraction

Contents

Chapter 1

Introduction

General The world has been remarkably influenced by the emergence of the semiconductor technology. The capability of engineering the band structure by the fabrication of the artificial semiconductor structures leads to numerous possibilities in the areas of high-speed information processing, light detection and emission, and conversion of solar and thermal radiation into usable electrical energy. Facilitated by the advent of advanced growth techniques, such as molecular beam epitaxy (MBE), heterostructures composed of dissimilar materials can be realized with a high crystallinity and a precisely controlled layer thickness. This enables the fabrication of complicated multilayer systems, where novel electronic and optical properties are expected for both scientific research and industrial utilization, e.g. quantum well lasers and high mobility transistors. Following the success of Si-based microelectronics, which is still the prevailing commercialized materials system, much emphasis has been placed on developing devices involving GaAs to utilize the exceptionally high carrier mobilities and direct band gap of this material. Besides, more and more new materials, including but not limited to semiconductors, are synthesized to achieve new functionalities and to expand the role of the semiconductor industry.

The performance of the devices based on the heterostructures are critically influenced by their structural properties, including the crystalline epitaxial orientation, the bonding configuration of the interface, the atomic ordering, the extended defects and the residual strain state of the films. For instance, threading dislocations in the active layer acting as nonradiative centers strongly limit the performances of light emitting diodes (LED) [1, 2]. The spin transportation in the spintronic device is affected by the strain state of the system because the strain field may scatter and relax the spin of the electron [3, 4]. In addition, knowledge of microstructural properties of the heterostructure provides crucial information for the understanding of the physical principles of heteroepitaxy. Therefore, structural characterization of the heterosystem is of obvious necessity due to the interest in both the fundamental physics and device applications.

(110) oriented heterostructures The interests on (110) oriented heterostructures could date back to the 70's and are originally motivated by the manufacturing of GaAs devices on group IV semiconductors [5]. The (110) non-polar plane of the zinc-blende structure have been proposed as one of the preferred orientations for the epitaxial growth of zinc-blende films on group IV substrates, because of the absence of interface charge imbalance for this plane [6]. The optical anisotropy of the (110) quantum wells is another motivation for the device applications, e.g. optical modulators or vertical-cavity surface emitting lasers (VCSEL) [7]. Besides, the hole mobility in (110) oriented strained Si is higher than those in conventional devices based on Si (001) substrate [8], leading to a better performance of metal oxide semiconductor field effect transistors (MOSFET) with such orientation [9]. Moreover, an improved optical property is obtained for GaN when

realized on Si (110) due to the good crystallographic quality of GaN layer, which may offer a promising approach for the integration of GaN- based optoelectronic with silicon devices [10].

Recently, the emergence of spintronic technology [4] leads to the discovery of another merit of (110) oriented structures. In the spintronic device, it is not only the electron charge but also the electron spin carrying the information. Adding this degree of freedom to the conventional charge-based semiconductor electronics could add substantially more capability and performance to electronic products [11, 12]. A crucial factor of the spintronics is the spin lifetime, which must be sufficiently long for the transport and manipulation of the spins in heterojunctions. Comparing with the well-studied quantum wells with (001) orientation, it is found [13] that the spin relaxation time for GaAs (110) quantum wells is an order of magnitude longer than that of its (001) counterpart, from the picosecond range to the nanosecond range at room temperature. (110) oriented heterostructures is therefore of significant interest for spintronic device applications.

Motivation and outline The above mentioned topics have already outlined the objective of the present work. The main goal is to have a systematical microstructural study of the heterostructures epitaxially grown on GaAs (110). Three heterosystems are investigated as case studies including (Al,Ga)As/GaAs, MnAs/GaAs and CoAl/GaAs. These chosen materials cover three major lattice symmetries, i.e. face-centered cubic (fcc), hexagonal close-packed (hcp) and body-centered cubic (bcc)/B2, and they differ with each other not only in lattice mismatch with respect to GaAs, but also in the crystalline phases, from semiconductor compound, over half-metal to metal alloy. Interface properties are the main focus in the present study. We analyze for each system the epitaxial orientation relationship and the corresponding lattice mismatches. The respective ways to accommodate the strain related to the mismatches are studied on the basis of a detail investigation of the interfaces, including: *atomic arrangements, defect properties and strain states*. The effect of different interface configurations on the microstructural properties of the layer is also researched. Different techniques in transmission electron microscopy (TEM) are employed in the study including: bright-field and dark-field imaging, selected area and nanobeam electron diffraction, high-resolution TEM with the assistance of the phase contrast simulations.

The thesis is organized as follows. Chapter 2 describes the basic concepts of MBE and the growth modes in epitaxy. In addition, crystalline defects in the epitaxial layer, e.g. dislocations and stacking faults, are discussed with respect to plastic relaxation of the lattice misfit stress. Chapter 3 gives a brief introduction of different TEM techniques used in this work. These two chapters provide fundamental information in necessary detail for the understanding of other parts of the thesis.

A review of the general aspects of the heterostructures grown on GaAs (110) is given in Chapter 4. The elastic behavior, critical layer thickness and other intrinsic properties of the structure with (110) orientation are discussed in comparison with its well-studied (001) counterpart.

Chapter 5 addresses the structural properties of fcc-type (Al,Ga)As/GaAs multilayers on GaAs (110). The reduced number of slip systems leads to a distinct lattice mismatch strain accommodation processes between mutually perpendicular in-plane directions, resulting in anisotropic residual states. Short period superlattice (SPSL) is an effective way to stabilize the structure against the plastic relaxation. A defect-free structure is obtained with more SPSL introduced. The effect of SPSL is further verified by the

nano-indentation tests.

Chapter 6 treats hexagonal type MnAs epilayers on GaAs (110). Despite the different symmetries of the adjacent planes at the heterointerface and the extreme lattice mismatch, MnAs grows epitaxially via a layer plus island mode on GaAs (110) with its prism plane parallel to the substrate surface. The asymmetric interface character leads to an anisotropic process of the lattice mismatch accommodation, where the mismatches along perpendicular in-plane directions are accommodated by coherent strain and an array of interfacial misfit dislocations. The elastic distortion associated with this periodic dislocation array is confined within a thickness of about 3.4 nm away from the interface. An atomic interfacial model is proposed based on the comparison between the lattice images of the coherent region at the interface and the simulated high-resolution contrast. Finally, the overgrowth of GaAs on MnAs is discussed in detail.

Chapter 7 deals with the microstructural analysis of B2-type intermetallic CoAl alloys, where a comparison between (001) and (110) oriented heterostructure is performed. For both orientations, we find in the CoAl films the existence of bcc phase, which is a disordered version of B2 crystal lattice. Such local disordering is induced partially by the diffusion of vacancies and Co atoms and partially by the epitaxial strain. Unexpected misoriented domains are formed in CoAl/GaAs (110) originated from the interface roughness.

Chapter 2

Microstructural aspects of heteroepitaxy

Heteroepitaxy denotes the epitaxial growth of a layer or a thin film with a chemical composition, and usually also structural parameters, different from those of substrates. Different microstructural aspects of heteroepitaxy are presented in this chapter in sufficient detail for other parts of the thesis. We first give a brief introduction to molecular beam epitaxy, the method we use for growth. Different growth modes in epitaxy with their theoretical background are then outlined. Afterwards, we describe the extended defects in crystalline structure, e.g. dislocations and stacking faults. Finally, different kinds of interfaces in the heteroepitaxy are addressed in connection with their specific ways of mismatch strain relaxation.

2.1 Heteroepitaxial growth

To understand the microstructure, i.e. the defect microstructure, of the heterostructure and its related physical properties, the basic knowledge of the working principle of molecular beam epitaxy (MBE) as well as the possible growth modes of thin films is of obvious necessity.

2.1.1 Molecular beam epitaxy

The epitaxial growth technique employed in this thesis is MBE. MBE is a sophisticated and versatile technique for growing ultra thin epitaxial films of semiconductors, metals and other materials. This technique was invented in late 1960s at Bell Telephone Laboratory by J.R. Arthur [14] and Alfred Y. Cho [15]. With the development of the technology, MBE nowadays provides the possibility for the growth of many kinds of complex multilayer structure, metal-semiconductor hybrid systems and for the combination of large lattice mismatched and dissimilar materials. Comparing with other epitaxial growth techniques, e.g. liquid phase epitaxy and vapor phase epitaxy, MBE shows unique advantages, such as the precise control of thickness (accuracy down to monolayer), ability to produce extremely abrupt interface and the progressive smoothing of the growing surface for most substrate orientations [16]. What's more, with the employment of the in situ surface analysis method like reflection high-energy electron diffraction (RHEED), the growth condition could be adjusted and further maintained to favor the deposition of the desired structures.

Figure 2.1 schematically illustrates a typical MBE growth chamber. It is normally equipped with a certain number of effusion cells allowing the growth of a variety of materials. The base pressure of the chamber is maintained at about 7×10^{-10} mbar with the help of both an ion pump and a turbo-molecular pump. Because of the ultra high vacuum (UHV) conditions, the growth in MBE is generally conducted far from the thermodynamic equilibrium state but governed mainly by the kinetics of surface process [17].

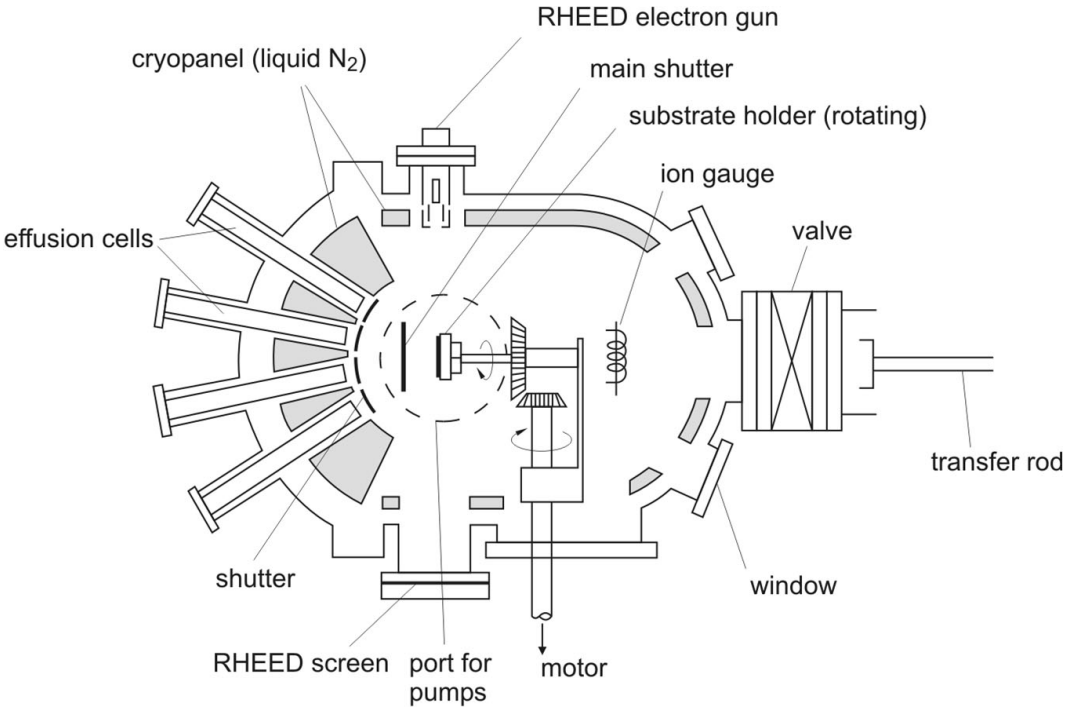

Figure 2.1: Schematic diagram of MBE growth chamber [17].

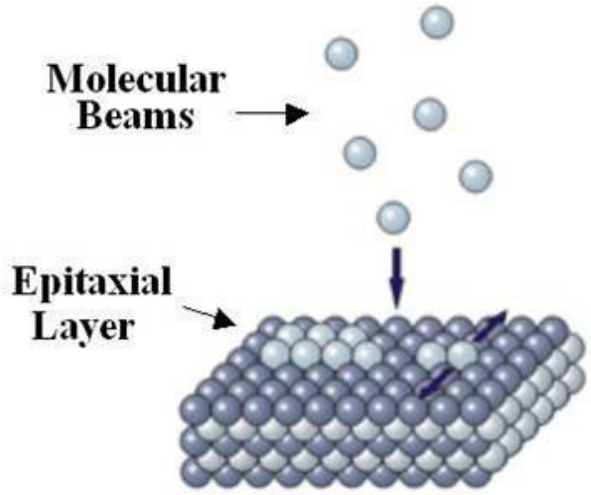

Figure 2.2: Epitaxial growth in MBE [127].

The basic principle of epitaxial growth is that atoms on a clean surface are free to move around until they find a correct position on the crystal lattice surface to bond. For the production of one atomic layer, as shown in Figure 2.2, ultra-pure elements are delivered to the substrate as a molecular beam made by the effusion cell. The atoms or molecules then deposit on the surface bonding with adatoms. Beam fluxes of each effusion cell may be turned on and off rapidly with a shutter, which enables to precisely control the layer compositions.

2.1.2 Growth mode

In a simple fashion, growth of dissimilar materials onto the substrate could be divided into two steps: initial nucleation and consequent growth. The initial step is essentially important for the determination of the growth modes. With the consideration of energetic equilibrium criteria [19, 20], the growth mode is dominated by the surface free energies of substrate (γ_s), overlayer (γ_o), the interface energy (γ_i) and the strain energy (γ_ε). When

$$\gamma_o + \gamma_i - \gamma_s + \gamma_\varepsilon \leqslant 0 \tag{2.1}$$

the formation of two dimension (2-D) wetting layer is preferable, which is in favor of layer by layer or Frank-Van der Merwe (FM) growth as shown in Figure 2.3(a). If

$$\gamma_o + \gamma_i - \gamma_s + \gamma_\varepsilon > 0 \tag{2.2}$$

island growth mode will be preferred, which is known as Volmer-Weber (VW) growth [17, 20] as depicted in Figure 2.3(c). Figure 2.3(b) shows an intermediate case where FM growth is followed by VW growth. In this case, after the first monolayer or few monlayers accomplished by 2-D growth, FM mode is not favored because the strain energy increases with the growing layer and finally violates (2.1). Islands then form to minimize the total energy by expanding in the interface plane [21]. This layer-island mode is known as Stranski-Krastinov (SK) growth, it is frequently observed during the growth of InAs/GaAs [22].

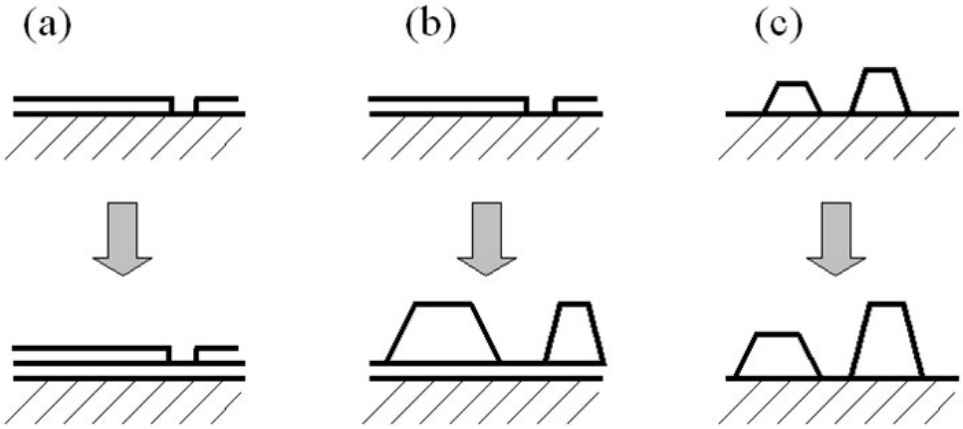

Figure 2.3: Schematic diagram representing three most frequent growth modes: (a) layer by layer mode (Frank-van der Merwe) (b) layer-island mode (Stranski-Krastanov) (c) island mode (Volmer-Weber).

2.1.3 Lattice misfit and strain

Combination of dissimilar materials by means of heteroepitaxy faces the difficulty of accommodation of different structural lattice parameters between the overlayer and the substrate, known as lattice mismatch. The term "mismatch" is usually used to refer to the disregistry of the equilibrium interfacial atomic arrangements of the substrate and

the unstrained epilayer, which is defined as

$$f = (d^f_{hkl} - d^s_{h'k'l'})/d^f_{hkl} \tag{2.3}$$

where d^f_{hkl} and $d^s_{h'k'l'}$ denote the unstrained natural spacings of the corresponding atomic planes in the film and substrate, respectively. The mismatch could be anisotropic, as in the case of MnAs/GaAs (cf. Chapter 6). For the other two cubic systems (CoAl/GaAs and (Al, Ga)As/GaAs) in this thesis, it is isotropic.

The epi-strain ε in a 2-D layer is the in-plane strain by which it is elastically deformed from the natural value, which is given by:

$$\varepsilon = f - \varepsilon^p \tag{2.4}$$

where ε^p is the plastic strain corresponding to a reduction in ε by the introduction of suitable dislocations at the interface. As noticed, ε is equal to $\varepsilon^0 = f$ in a pseudomorphic growth, while it is 0 when the mismatch strain is totally relaxed plastically. Normally, ε will lie between 0 and f.

According to the calculation result of R. Hull [23], for a typical heteroepitaxial material system, a mismatch of 1% between the overlayer and substrate generates a stress of about 2 GPa in the overlayer. Consequently, except for the quite unusual incoherent growth where both overlayer and substrate crystals retain their lattice parameters, the epilayers have to find ways to coordinate this enormous lattice mismatch stress, elastically or plastically.

2.2 Extended defects in epitaxial layers

Epitaxially grown layers usually contain many crystalline extended defects. In most cases, they have a deleterious effect on minority-carrier lifetimes and radiative recombination rates, which further affect the device's electronic and optical properties. In order to find ways to eliminate the defects, or in some case to restrict the defect density under a tolerable value, it is essential to know their properties and the way they originate.

Extends defects here refer to one-dimensional line defects, i.e. dislocations, two-dimensional planar defects, i.e. stacking faults and twins, and three-dimensional volume defects, i.e. precipitates and voids.

2.2.1 Dislocations

A dislocation is a crystallographic defect or irregularity within a crystal structure. It is created when planes of atoms are distorted out of their natural position. There are mainly two types of dislocations: edge dislocation and screw dislocation, depending on the geometry of local distortion. Dislocations are frequently observed in the heteroepitaxial systems, and the possible formation scenarios are [51]:

- the extension of substrate dislocations,
- the accommodation of translational and rotational displacements between islands,
- the formation of dislocation loop by the aggregation of point defects,
- plastic deformation of the epilayer.

Dislocation can be categorized by its line direction **u** and Burgers vector **b**, which is geometrically defined by a Burgers circuit constructed around the dislocation as indicated by blue arrows in Figure 2.4. Formed by introducing an extra half-plane of atoms mid way through the crystal, the edge dislocation is characterized by its Burgers vector **b** normal to its line direction **u** defined by the boundary of the inserted extra half plane. Screw dislocation's Burgers vector **b** is parallel to its line direction **u**, and atoms are connected in a helix (spiral staircase) around the screw dislocation. In the most general case, however, the arbitrary angle between the Burgers vector **b** and the line direction **u** is neither 0° nor 90° and the dislocation line has a mixed edge and screw character.

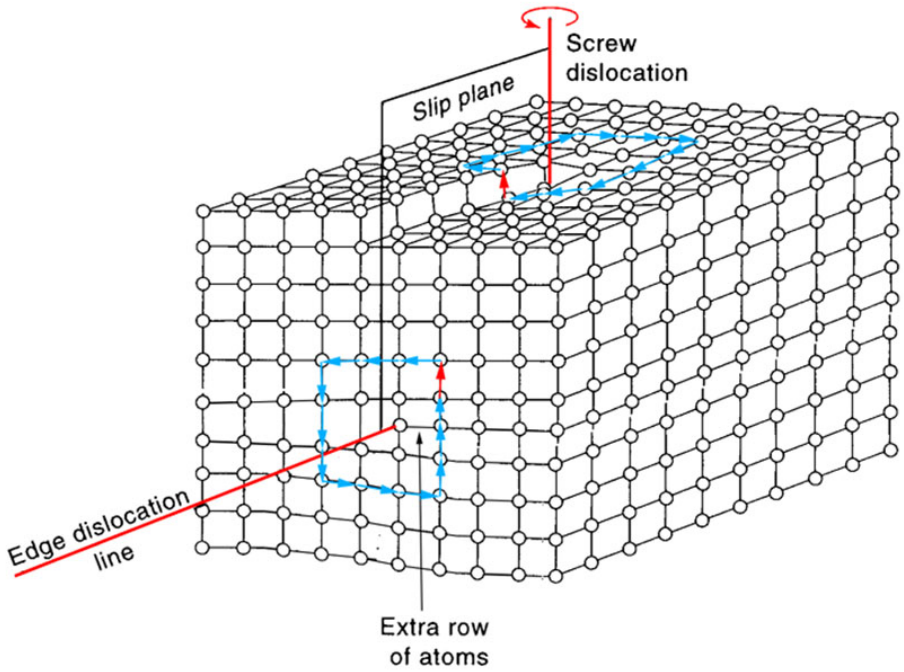

Figure 2.4: The diagram of an edge dislocation and a screw dislocation in a cubic crystal with Burgers circuits indicated by blue arrows. The red arrows represent the Burgers vector [29].

Dislocations that can move by pure slip are called glissile dislocations. They slip in planes containing both the dislocation line and the Burgers vector. For a screw dislocation, the line direction and the Burgers vector are parallel, so the dislocation may slip in any plane containing itself. For an edge dislocation, the dislocation and the Burgers vector are perpendicular, so there is only one plane in which the dislocation can slip. The slip plane is normally the plane with the highest density of atoms and the direction of slip is the direction in the slip plane in which are most closely packed. For example, face-centered cubic crystals have four $\{111\}$ close-packed planes with three $\langle 110 \rangle$ directions each, making twelve $\{111\}\langle 110 \rangle$ slip systems. Resolved shear stress τ is another important factor for slip. It represents the effective stress applied onto the dislocation and is defined by [30]:

$$\tau = \sigma \cos\beta \cos\phi \tag{2.5}$$

where σ represents external stress, ϕ is the angle between the normal to the glide plane and the stress axis and β is the angle between the Burgers vector and the normal in the interface to the dislocation line direction. The perfect dislocation under certain condi-

tion can dissociate into two partial dislocations, both of which mutually repel each other and glide apart on the slip plane, producing a ribbon of stacking fault in between. This dissociation is possible because it is energetically favorable according to $|\mathbf{b}|^2$ criteria [24, 30]. The energy cost of stacking fault somehow balances the energy difference between the perfect dislocation and partial dislocations. Glissile dislocations are observed and discussed in detail in (Al, Ga)As/GaAs case (cf. Chapter 5).

Dislocations that cannot glide, but have to move by some form of mass transport are called sessile dislocations. They are generally formed during the growth at the nucleation stage. For instance, sessile edge-type dislocation is instantaneously formed via the incorporation of extra lattice planes into the edge of the growing nuclei of the island during the epitaxial growth of GaN on GaAs (001) [45]. In this study, sessile dislocations are found in MnAs/GaAs heterostructure, and their formation mechanisms are discussed in Chapter 6.

2.2.2 Stacking fault

The perfect lattice can be described as a stack of identical atom layers arranged in a regular sequence. The local region in the crystal where the sequence is interrupted is called two dimensional or planar defects. Depending on the status of misstacking, the planar defects could be categorized into stacking faults and nanotwins.

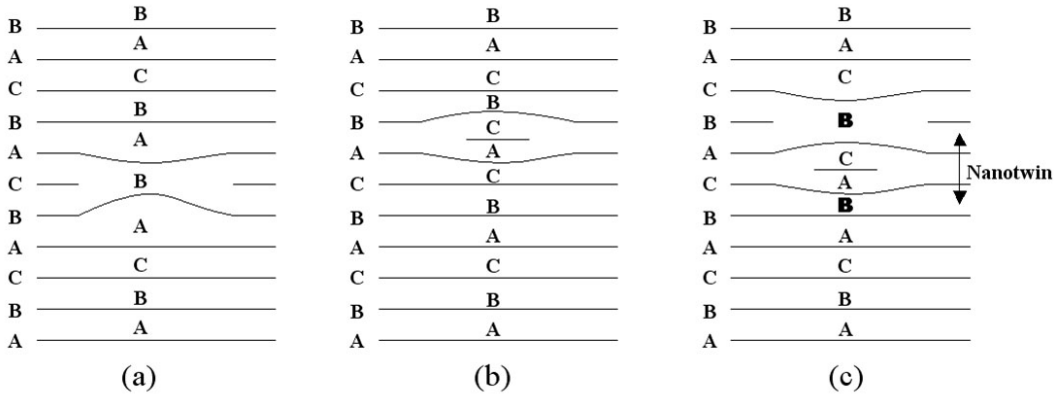

Figure 2.5: Planar defects in fcc lattice (a) intrinsic stacking fault (b) extrinsic stacking fault (c) nanotwin. The normal sequence of {111} planes are denoted by ABCA...

Stacking faults occur in a number of crystal structures, but the common example is in close-packed structures. Face-centered cubic (fcc) structures differ from hexagonal close-packed (hcp) structures only in stacking order. When stacking one of these layers on top of another, the atoms are not directly on top of one another — the first two layers are identical for hcp and fcc, and labeled AB. If the third layer is placed so that its atoms are directly above those of the first layer, the stacking will be ABA — this is the hcp structure, and it continues ABABABAB. However there is another location for the third layer, such that its atoms are not above the first layer. Instead, the fourth layer is placed so that its atoms are directly above the first layer. This produces the stacking ABCABCABC, and is actually a cubic arrangement of the atoms. A stacking fault is a one or two layer interruption in the stacking sequence, for example if the sequence ABCABABCAB were found in an fcc structure. In an fcc crystal, two types of stacking faults are possible, known as intrinsic and extrinsic stacking faults, which are best described by change in

the sequence resulting from the removal or insertion of an extra layer, respectively. For instance, ABCABABC contains an intrinsic stacking fault while ABCABCACBC have an extra atomic layer C inserted resulting in extrinsic stacking fault, as illustrated in Figure 2.5(a) and (b).

When a crystal is composed of parts that are oriented with respect to one another according to a symmetrical manner, the crystal is regarded to be twinned [35]. The plane that separates these two parts is called twin boundary. If the width of the twin is of nanometer size, it is called nanotwin, as shown in Figure 2.5(c). From the defect-free fcc lattice, the stacking sequence changes to ABCABACBCABC, containing a nanotwin BACBC of five atomic layers thick.

The origin of the stacking fault and twin frequently coincides with the dissociation process of the perfect dislocation described in the previous section. Other than that, the deposition error during the growth is also a possible reason of their formation [45-47]. In the initial nucleation stage, atoms in high-energy sites are preferentially emitted to a low-energy site, which leads the nuclei faceted due to the variable surface energy of different crystallographic orientation. For instance, the zinc-blende materials exhibit two low energy facets 001 and 111. If during the deposition, an atom cluster sits in an incorrect position as shown in Figure 2.6(a), it will spread all over the facet and result in the formation of stacking fault. Nanotwin could be further formed in the same manner, and its thickness will be simply determined by the next stacking inversion. The schematic diagram of stacking fault and nanotwin are illustrated in Figure 2.6(b) and (c), respectively. Furthermore, during the island coalescence stage in the epitaxial growth, stacking fault could also happen if the stacking sequences of two adjoining islands are not in phase with each other. The above-mentioned growth related planar defects have been discussed in detail in Chapter 6.

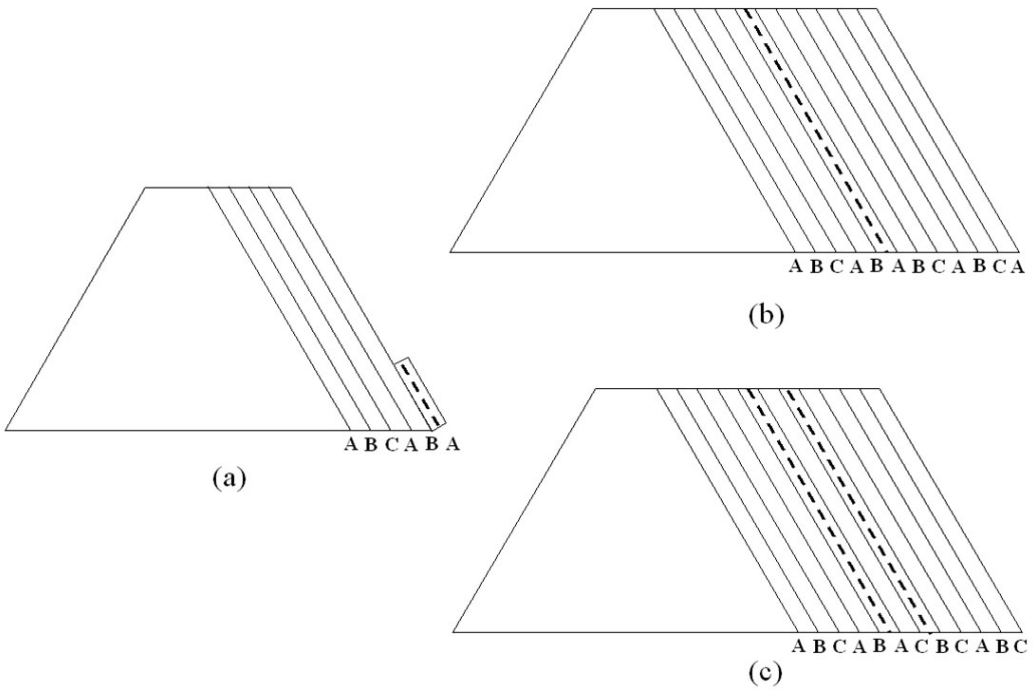

Figure 2.6: When deposition error occurs (a), it could grow laterally and lead to the formation of stacking fault (b) and nanotwin (c). Dashed line represents stacking fault [46].

2.2.3 Volume defect

Volume defects in a crystal such as voids and precipitates are also known as three-dimensional defects. They can occur under certain circumstance and have important effect of properties of crystalline solids. Voids refer to the absence of a number of atoms to form internal surface in the crystal. Precipitates mean the formation of another phase of different structure or composition by precipitating the impurity atoms. Precipitates are considered undesirable because they have been known to act as sites for the generation of dislocations. Dislocations arise as a means of relieving stress generated by the strain exerted by precipitates on the lattice.

The volume defect may be introduced by interfacial reaction between the reactive epilayer and substrate at a relative high temperature. In strained layer heteroepitaxy, high misfit stress is also possible to induce the formation of volume defects. For instance, in the case of $(GaAs)_n/(InAs)_n$ short period superlattice grown on InP(001) [48], an alternative In-rich domain and Ga-rich domain exist in the superlattice region. The driving force for this lateral modulation is attributed to the surface strain generated in the initial stages of heteroepitaxial growth of superlattices. It is demonstrated that the modulated layer was more thermodynamically stable than its unmodulated counterpart under such strained condition [49], and rather than generating a periodic dislocation array, the lateral composition modulation is preferable. Structural modulation is also observed in the MnAs/GaAs(001) heterosystem [18]. In the bulk, the β-phase MnAs changes to α-phase at a temperature of 40°C and this transition is abrupt with a thermal hysteresis of about 10°C. However, it is found that both phases coexist over a very wide temperature range in the heterosystem. This is explained using the energy minimization by strain redistribution [50]. Since MnAs film is compressively strained along the $[11\bar{2}0]$ direction and tensile in the [0001] direction [44], the free energy minimum is reached through the coexistence of domains of the two phases with different strain. In the present thesis, the epitaxial misfit stress in CoAl/GaAs leads to a phase transformation of CoAl from B2 to a disordered bcc, which is described in detail in Chapter 7.

2.3 Interface and relaxation

Interface is a key factor in heteroepitaxy. It determines the epitaxial orientation geometry between the substrate and the epilayer, and accordingly the lattice mismatches along different in-plane directions as well as the specific ways of mismatch strain relaxation. As a result, interface could considerably affect the structural properties of the subsequent growth and the corresponding performance of devices based on such heterostructure.

Generally speaking, there are three distinct types of interface structures: coherent, semi-coherent and incoherent, as schematically shown in Figure 2.7. A coherent interface between two crystals is defined as one for which corresponding atom planes are continuous across the interface, i.e. the atomic structure is characterized by an atom-by-atom matching across the interface. Conversely, if there is no continuity of planes across the interface, i.e. if a one-on-one atomic matching does not exist even locally, the interface is referred to as incoherent. The incoherent interface with weak interfacial interaction does not seem consistent with the ability to form a unique epitaxial-oriented layer and is therefore a more unusual situation in the epitaxy. Semi-coherent interface, terminologically, represents an interface configuration in between these two extremes. Figure 2.7(b) illustrates a typical semi-coherent interface, where large areas of preserved coherency are

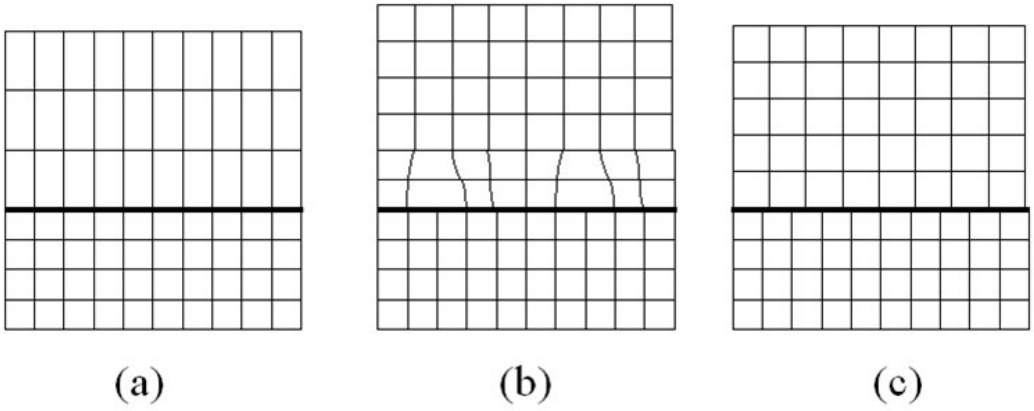

Figure 2.7: Schematic illustrations of (a) coherent, (b) semi-coherent and (c) incoherent interfaces.

separated by localized misfit dislocations.

In case of heteroepitaxy, the interface structure often describes a low-energy configuration. For low lattice-mismatched system, the low-energy criterion is simply fulfilled either by accommodating the small lattice mismatch elastically by biaxial strain and tetragonal distortion of the lattice (coherent interface), or by misfit dislocations between isostructural materials (semi-coherent interface). However, when it comes to the general heteroepitaxy where both lattice parameter and symmetry can be arbitrarily large, the low-energy interfaces are often discussed in terms of the geometry criteria, mostly based on structural coincidences between the adjoining crystal lattices [36]. In the following, we will discuss the different interfacial configurations and their related mismatch relaxation mechanisms in detail for these two conditions.

2.3.1 Nearly lattice-matched heterostructures

When the mismatch f is sufficiently small, the first atomic monolayers deposited will be strained to match the substrate with a one-to-one correspondence of atom positions at the interface (coherent interface). This is so called pseudomorphical growth as illustrated by Figure 2.7(a) with the entire mismatch accommodated elastically by the tetragonal distortion of the epilayer lattices. A biaxial stress is imposed on the film to elastically deform it to fit the dimensions of the substrate. This geometry stores a high amount of elastic strain energy, because interatomic bond length in the epilayer are significantly stretched or compressed with respect to their natural value. In an anisotropic material system, the stress $\sigma_{[hkl]}$ along the $[hkl]$ direction is given by [31]:

$$\sigma_{[hkl]} = M_{[hkl]}\varepsilon^0_{[hkl]} \tag{2.6}$$

where $M^0_{[hkl]}$ and $\varepsilon^0_{[hkl]}$ is the biaxial elastic modulus and strain of the film along the $[hkl]$ direction, respectively. When the growth exceeds certain thickness, called the critical thickness h_c [25], it is energetically favorable for the introduction of the misfit dislocation.

Critical thickness Two theories have been developed to calculate the equilibrium critical thickness. The first is based on the principle of energy minimization by Ball [106],

while the second is proposed by Matthews and Blakeslee (MB) [33] known as force balance theory. If accurately described, two theories are equivalent and always give identical numerical value of h_c. Here in this thesis, MB method is adopted. In MB model, a preexisting threading dislocation is present crossing the interface of the structure. The dislocation tends to propagate through the layer depositing misfit dislocation if the driven force from the lattice mismatch is sufficiently high. However, the generated misfit dislocation length will have self-energy, which produces a restoring stress against the motion. The critical thickness is defined at the point when the driven force is identical to the restoring force. In an elastic anisotropic heterosystem, the critical thickness is direction dependent and the value corresponding to $\varepsilon^0_{[hkl]}$ is given by [24]:

$$h_c^{[hkl]} = \frac{\mu b(1-\nu\cos^2\theta)}{4\pi(1-\nu)M_{[hkl]}\varepsilon^0_{[hkl]}\cos\beta}\ln(\frac{\alpha h_c^{[hkl]}}{b}) \tag{2.7}$$

where b is the magnitude of Burgers vector, α is the core energy parameter, θ is the angle between the Burgers vector and the dislocation line direction, ν is Poisson's ratio for the overlayer and μ is the shear modulus of elasticity. However, it is well known that there is discrepancy between the experimentally determined h_c and the MB prediction in semiconductor materials. Generally speaking, this discrepancy could come from two factors. The first is that MB method neglects the Peierls-Nabarro friction stress [20, 34], which strongly reduces the mobility of dislocations. Secondly, MB method assumes preexisting dislocations, however, with the advances in semiconductor technology, the number of available threading dislocations might not be sufficient and nucleation must be taken into account. Nevertheless, MB method is still widely accepted as standard approach to estimate h_c. In this thesis, we consider it as a rough estimation of the lower limit of the critical thickness.

Lattice mismatch strain relaxation Mismatch strain relaxation can be realized by the formation of misfit dislocations. A misfit dislocation has its line direction to lie approximately parallel to the epitaxial interface and its Burgers vector containing an edge component for the mismatch relaxation. They are introduced either by the bowing of preexisting substrate dislocations which penetrate into the epilayer, or by expansion of half loops nucleated at the film surface, as schematically illustrated in Figure 2.8. Dislocations are glissile in the slip planes of the crystal. When the applied resolved shear stress is larger than a certain value, the dislocation can move through the film to the interface, where they form misfit dislocations. If the density of threading dislocation is not sufficiently high for the relaxation, half loops will nucleate at the surface of the film and expand to the interface and misfit dislocation can be formed in the same manner. Both mechanisms lead to the formation of the dislocation segments as shown in Figure 2.8(c). The strain ε^p that is relaxed by the misfit dislocation could be obtained when the mean distance D between dislocations is available according to [36]:

$$\varepsilon^p = \frac{b^i}{D} \tag{2.8}$$

where b^i is the in-plane Burgers vector which is effective to relieve the mismatch strain.

The perfect dislocation is energetically favorable to split up into two different partials, known as Shockley partial dislocations. An intrinsic stacking fault is possible to

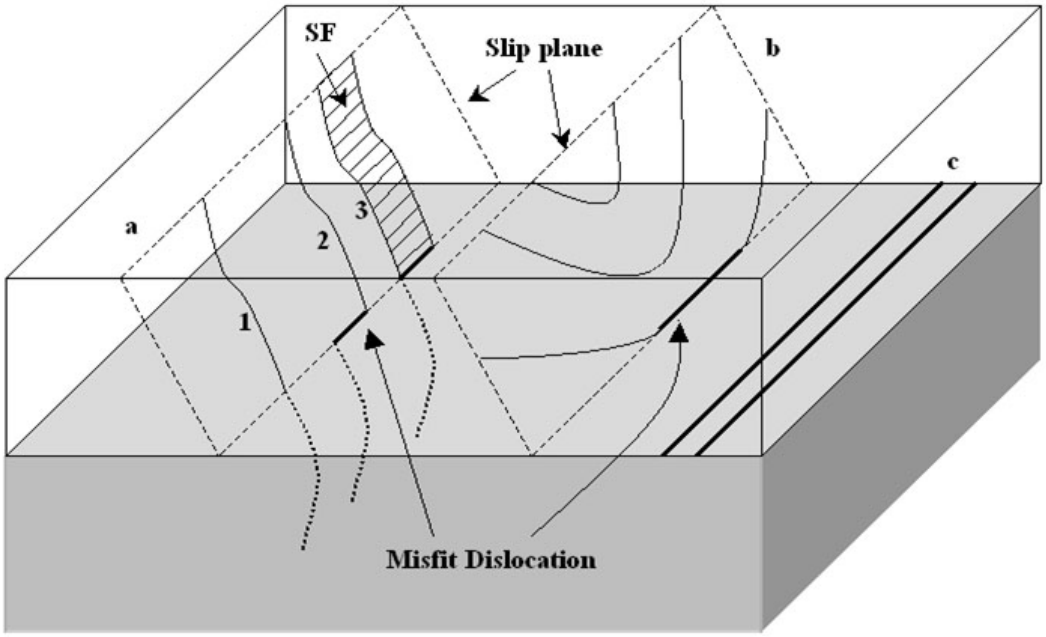

Figure 2.8: Schematic diagram indicating how to generate misfit dislocations by the glide of (a) a threading dislocation and by the expansion of (b) a half loop in the slip planes. The misfit dislocation could be dissociated into two partials, repelling each other and resulting in stacking fault (SF) in between. (c) misfit dislocation segments formed in the interface.

be formed in the slip plane when two partials separate under the influence of the repulsive force between them. The geometry and the strain state of the epilayer determine which partial can nucleate first and which partial is leading. For zinc-blende-type crystal growing on GaAs (001), as an example, a perfect 60° misfit dislocation could decompose into a 30° Shockley partial and a 90° Shockley partial. For a given mismatch stress, 90° partial experiences force twice as large as that on 30° partial. If the stress field is tensile, the 90° dislocation nucleates first and experiences largest force thus forming a stacking fault. If the stress field is compressive, passage of 30° dislocation is required to produce a low-energy stacking fault. However, after the nucleation of 30° dislocation, it will be instantly followed by 90° dislocation driven by higher force as well as the force related to stacking fault, which will finally annihilate the stacking fault [24, 37]. In contrast, for (011) and (111) substrate orientations, the geometrical arrangement of the atoms on the glide planes requires leading 90° partial dislocation for the formation of stacking faults if the strain field is compressive [38]. The misfit strain relaxation is carried out by these leading 90° partial dislocations.

Nanotwin may be considered as a continuous disruption of the stacking sequence of the crystal. It could be formed by gliding of a group of partial dislocations along parallel successive slip planes. Similar to the stacking fault, the partial dislocations bounding the twin are responsible for the relaxation [39, 40].

2.3.2 Heteroepitaxy of dissimilar materials

For the heteroepitaxy of highly mismatched materials possibly with different lattice symmetry, the interface structure is more complex and the way of misfit strain accommo-

dation can't be simply predicted by the classic relaxation mechanisms. Since the strain energy represents the most important part of the interfacial energy in this case, the interface fulfilling the low-energy criterion is often explained by an extended coincidence model [36]. This model is based on the theory of coincidence site lattice (CSL). To describe the interface configuration in general epitaxy accurately, the CSL model has to be extended. According to CSL model, a perfect coincidence sites (best fit positions) between substrates and overlayer occur when

$$ma_s = na_o \tag{2.9}$$

where m and n are positive integers. Once (2.9) is satisfied, the atomic positions on both sides of the interface are long-range ordered, and a common planar unit cell exists describing the periodic structure. The one unit cell-one unit cell correspondence leads to a quasi-coherent interface, which is also called commensurate as shown in Figure 2.9(a).

The interfacial energy could be further reduced by a local coherence stress relaxation within each coincidence unit cell (Figure 2.9(b)). The interface specific dislocations do not have to be equivalent to bulk ones. They are mostly pure edge dislocations of highly efficiency of strain relaxation. As an example, only edge-type dislocations are observed in the interface of InAs/GaAs [41] even in the initial nucleation stage, and the linear density of this 90° dislocation increases with the island expansion. As the slip system of a crystal with the sphalerite structure is $\frac{1}{2}\langle 110\rangle\{111\}$, the observed dislocations are unlikely to be introduced by the classic glide process. These dislocations are formed at the edge of growing islands [42] to relax the mismatch strain in the coincidence unit cell of $14a_{InAs}/15a_{GaAs}$.

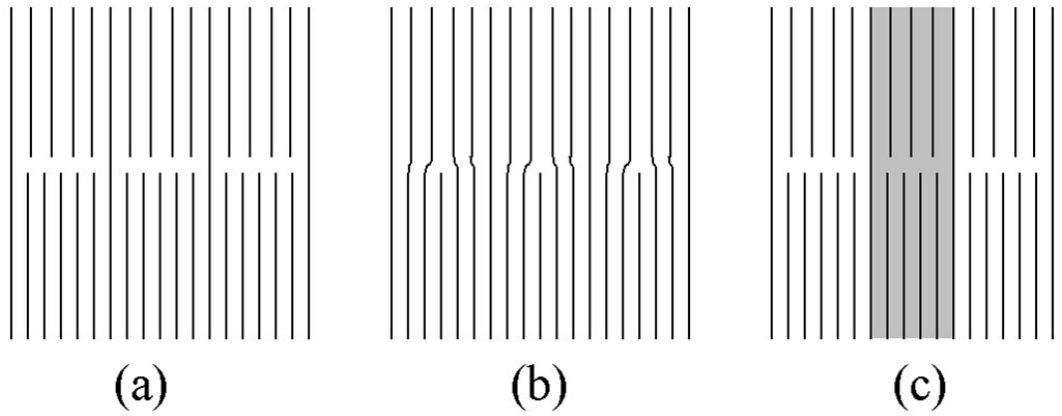

Figure 2.9: Coincidence site lattice (CSL) models of the interface between dissimilar materials (a) perfect coincidence (b) relaxation within each unit cell (c) perfect coincidence with a deviation forming a new unit cell.

In general epitaxial system, (2.9) cannot be fulfilled and a coincidence lattice misfit arises determining the amount of deviation. This deviation introduces strain into each unit cell, however its amount is much smaller than the bulk lattice mismatch, therefore, the interface energy will be low and epitaxy is favored. The deviation from the perfect coincidence is accommodated by the coincidence lattice misfit dislocations or secondary defect (Figure 2.9(c)), which generally depends on the symmetry of the interface, the bonding type and the amount of deviation. Such interface is termed semi-commensurate interface in comparison with the semi-coherent interface in the near lattice-matched sys-

tem. As in the case of MnAs/GaAs (001) [43, 44], the lattice mismatch along $[1\bar{1}0]$ direction is reduced to about 5% from the natural value 30% by 4 MnAs 0002 planes corresponding to 6 GaAs 220 planes. This 5% deviation is accommodated by the secondary dislocation that is characterized by an additional MnAs 0001 plane in one coincidence mesh extending its ratio from 8 to 6.

2.3.3 Physical principles

The most convenient classification of planar interfaces formed during epitaxial growth is based on minimizing the interfacial energy of the system. Away from the chemical part of the interfacial energy, e.g. adhesion energy and bonding geometry, the physical part is more related to the lattice misfit and the corresponding elastic or plastic contributions. To maintain a continuous epitaxial growth, a reduction of strain energy, i.e. a cancellation of long-range strain field is necessary.

In case of pseudomorphical growth of nearly lattice-matched materials, a long-range strain field is present in the system due to the tetragonal distortion of the epilayer lattice for the elastic accommodation of the lattice misfit (cf. Figure 2.7(a)). By the formation of interfacial dislocation array, the strain energy associated with the long-range strain fields is reduced since the long-range displacements are cancelled by these dislocations (cf. Figure 2.7(b)). However, localized strain fields corresponding to the dislocations are introduced to the area close to the interface.

The situation for the general epitaxy of dissimilar materials is similar. Based on the extended CSL model, if the lattice plane matching across the interface happens every ma_s and na_0 for the substrate and overlayer, respectively, the interface is commensurate where unit cells with the dimensions of ma_s for the substrate and na_0 for the overlayer describing the periodic structure. Once there is coincidence lattice misfit existing, the heterosystem will also present a long-range strain field due to the elastic distortion of the unit cells. The strain relaxation within each unit cell (cf. Figure 2.9(b)) is possible, and however, has no impact on the long-range strain field in the heterostructure. The strain energy corresponding to this long-range strain field can be reduced by the formation of the secondary interfacial dislocations (c.f Figure 2.9(c)), which introduce local strain fields close to the interface.

Chapter 3

Transmission Electron Microscopy

This chapter gives a brief introduction to TEM and covers different TEM techniques used in this work. We first concisely outline the structure of our microscope. Then, the theoretical background is presented for conventional TEM techniques including electron diffraction, bright-field and dark-field imaging. High-resolution TEM and nanobeam diffraction are introduced afterwards. At last, the sample preparation procedure is given.

3.1 Introduction

The structure and composition of the specimen could be determined on a microscopic scale by means of many surface analysis techniques. They are characterized by the radiation used to probe the specimen (electrons, X-rays, etc) and the radiation emitted from the specimen. In electron microscopes, only electrons or the radiation related to the electrons are employed to probe the sample. Figure 3.1 shows the signals emitted when a specimen is bombarded with electrons and the techniques that use these signals. When the incident electron beam passes through the electron transparent thin specimen, there is interaction with the electron cloud and positive nucleus in the crystal. These transmitted electrons carry the structural and chemical information of the specimen, which enables TEM as one of the most efficient tools for the characterization of materials.

TEM contains an electron gun and a series of electromagnetic lenses as shown schematically in Figure 3.2. An electrically heated Tungsten or LaB_6 filament or a field-emission electron gun is mounted on a ceramic insulator behind a Wehnelt cup. The emitted electrons are accelerated by a positive electrical potential and then enter the illumination system consisting of several condenser lenses and a condenser lens aperture. The illumination system transfers the electrons to the specimen giving either a broad beam or a focused beam. After interaction with the specimen, the electrons transmit through the heart of the microscope, i.e. objective lens, which governs the image resolution of the microscope. An image or a diffraction pattern of the specimen is finally acquired onto a fluorescent screen or a charge-coupled device (CCD) camera via a magnification system consisting of intermediated and projector lenses. TEM data in this thesis are obtained by a JOEL 3010 UHR microscope. It uses a LaB_6 filament, which can be operated at up to 300 kV accelerating potential. The microscope uses a fluorescent screen for imaging and a CCD camera is for acquisition of digital images. The point resolution for this microscope is 0.17 nm.

3.2 TEM techniques

The basis of electron microscopy is the electron scattering process in the materials. This process can be categorized into elastic scattering and inelastic scattering according to

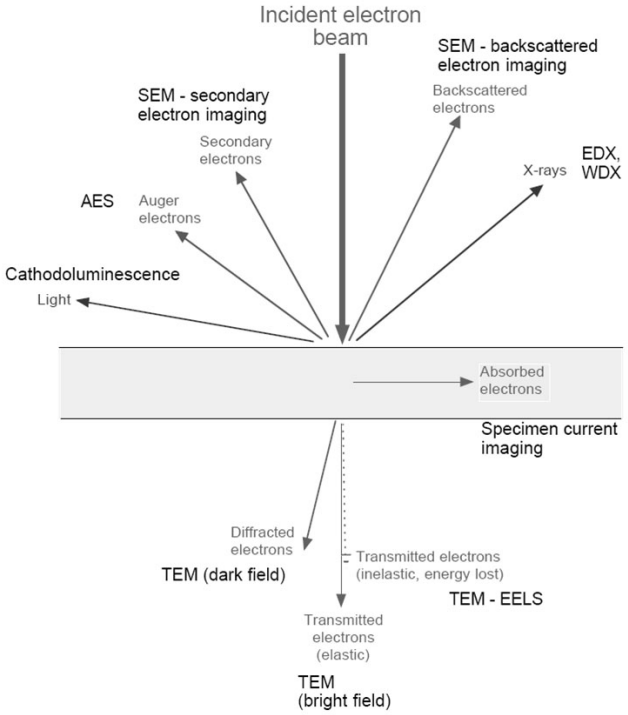

Figure 3.1: Techniques with respect to the signals generated by the electron bombardment of a thin specimen.

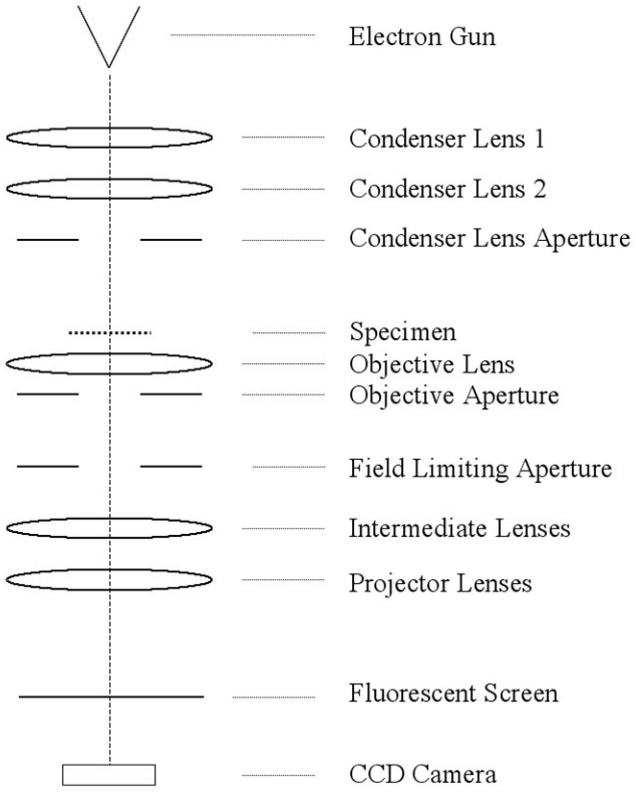

Figure 3.2: A diagram showing the main components of TEM.

energy and momentum conservation. Both of these processes are employed by different TEM techniques for structure or composition analysis. Image and diffraction formation in this thesis is achieved by methods only using electrons elastically scattered, such as selected area electron diffraction, dark-field imaging and high-resolution TEM.

3.2.1 Electron diffraction

When a beam of electrons is incident on the surface of a thin crystalline specimen, specific diffracted beams arise at the bottom exist surface. Although each individual atom in the crystal scatters the electrons, the scattered wavelets will only be in phase in some particular crystallographic directions, known as Bragg conditions.

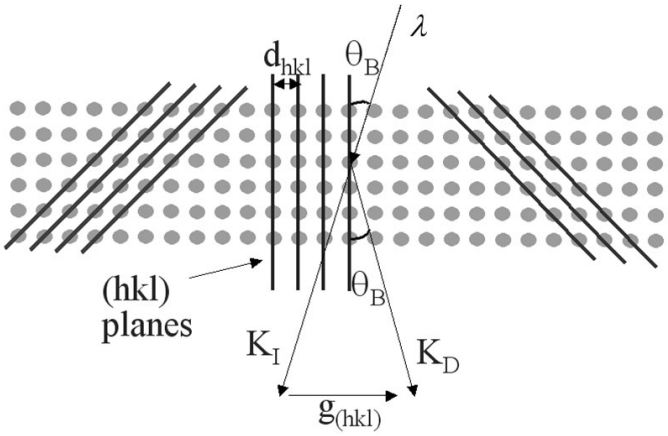

Figure 3.3: A schematic diagram of electron diffraction at Bragg condition. K_I and K_D denote the incident wave front normal and the diffracted wave front respectively. d_{hkl} is (hkl) plane spacing and λ is the electron wavelength.

Figure 3.3 shows the incident electron wave K_I, being scattered by a group of atom planes, i.e. (hkl) planes, producing diffracted waves K_D. The constructive electron wave interference will only occur when the electron beam is incident at Bragg angle θ_B, or in other words, when

$$K_D - K_I = \mathbf{g}_{(hkl)} \tag{3.1}$$

where $\mathbf{g}_{(hkl)}$ is a reciprocal lattice vector defined by the plane (hkl). This equation is the Bragg condition in vector notation. Noting $g_{(hkl)} = 1/d_{hkl}$ and $K_D = K_I = 1/\lambda$, (3.1) results in the well-known Bragg condition:

$$2d_{hkl} \sin\theta_B = \lambda \tag{3.2}$$

The process of diffraction using the Bragg's law could be visualized by the Ewald sphere construction and reciprocal lattice arrays. As shown in Figure 3.4, if the set of planes satisfy Bragg condition, the corresponding point in the reciprocal lattice intersects the surface of the sphere and the reflection is strongly excited in the viewing screen. However, due to the small wavelength of electrons (e.g., $\lambda = 1.97$ pm for 300 keV electrons), the radius of the Ewald sphere ($1/\lambda$) is quite large, resulting in an almost flat surface of the sphere. Furthermore, TEM specimens are very thin in real space, leading to the corresponding lattice points in the reciprocal lattice elongated parallel to the foil normal [26]. Consequently, the Ewald sphere intersects several of the rods. Many reflections

appear simultaneously since diffraction occurs even if the Bragg condition is not exactly satisfied.

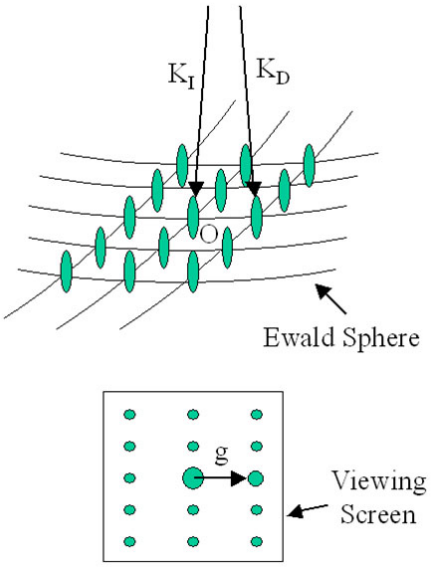

Figure 3.4: The Ewald sphere in a reciprocal lattice. K_I and K_D are incident and diffracted wave vector, respectively. O is the origin of the reciprocal lattice.

For crystalline materials, crystal symmetry is also an important factor to affect the diffraction pattern we expect to see. The structure factor describes the contribution of the entire unit cell to the diffracted intensity, which is given by [27]:

$$F_{hkl} = \sum_i f_i \exp(2\pi i g_{hkl} r_i) = \sum_i f_i \exp(2\pi i(hx_i + ky_i + lz_i)) \tag{3.3}$$

where f_i is atomic scattering factor, r_i is the position vector of each atom i in the unit cell and (h, k, l) is the fractional coordinates. For GaAs where Ga located on the origin of the fcc lattice (0, 0, 0) and the As related to it by the basis vector [1/4, 1/4, 1/4], as an example, the structure amplitude becomes

$$F = \{f_{Ga} + f_{As} e^{\frac{\pi}{2} i(h+k+l)}\}\{1 + e^{\pi i(h+k)} + e^{\pi i(h+l)} + e^{\pi i(l+k)}\} \tag{3.4}$$

from which, we can obtain:

- $F = 0$ if h, k, l are mixed,
- $F = 4(f_{Ga} \pm i f_{As})$ if h, k, l are all odd,
- $F = 4(f_{Ga} - f_{As})$ if h, k, l are all even and $h + k + l = 2N$ where N is odd,
- $F = 4(f_{Ga} + f_{As})$ if h, k, l are all even and $h + k + l = 2N$ where N is even.

The intensity of the spot we see in the diffraction pattern is proportional to F_2, so the spot is kinematically forbidden when $F = 0$, i.e. (0, 0, 1) and (1, 1, 0) spot. For different compound with the same fcc symmetry (e.g. AlAs and InAs), the term corresponding to $4(f_{Ga} - f_{As})$ will be different in each case. Therefore, reflections satisfying 3) are sensitive to the chemistry of the compound and called "chemically sensitive reflections".

Dark-field image with such reflections (e.g. (002)) as the **g** vector is further employed to investigate the spatial distribution of the compound.

Some reflections are only present once the material is ordered, which are termed "superlattice reflection". As an example, CoAl crystallizes in a cubic B2 structure, which can be degraded to bcc. F_{001} for B2 is a nonzero value given by $f_{Co} - f_{Al}$, where f_{Co} and f_{Al} is the respective atomic scattering factor of Co and Al. However, once Co and Al are mixed up leading to a bcc structure, i.e., the ordering is destroyed, F_{001} equals to zero given by $f_{(Co,Al)} - f_{(Co,Al)}$, where $f_{(Co,Al)}$ is the average atomic scattering factor of Co and Al. Consequently, by the appearance of the (001) reflection, one can analyze the ordering of the structure.

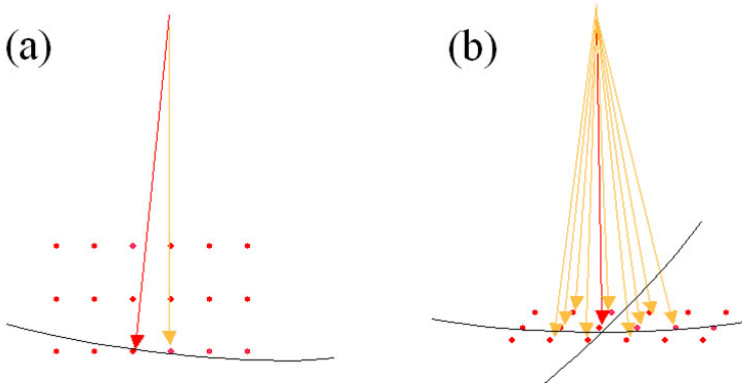

Figure 3.5: (a) two-beam condition (b) diffraction pattern when electron beam is aligned to zone axis.

Electron diffraction pattern is very important for materials characterization. It carries the structural information of the specimen. The conventional way to acquire the diffraction pattern of the specimen is selected-area electron diffraction (SAED). A field-limiting aperture is located in the intermediate-image plane above the intermediate lens (Figure 3.2). It selects an area of the specimen, from which the diffraction pattern is formed. However, for an area of nanometer scale, the SAED is not applicable anymore, other techniques, for instance, nano-beam diffraction (NBD) is required. Instead of limiting the area by an aperture, NBD uses a nanometer-sized beam to detect the specimen and acquire the accurate diffraction pattern from the corresponding illuminated nanometer-sized area [28, 52]. In this technique, a small probe with reduced convergence angle is directed to the sample producing diffraction pattern with spots similar to those of convention SAED.

Diffraction pattern enables a wide range of experiments to be performed. Correct adjustment of the diffraction pattern via specimen tilting is a prerequisite for the following imaging process. For instance, high-resolution TEM is possible only if the sample is tilted to the zone axis as shown in Figure 3.5(b) and two-beam condition, where only one single diffracted beam is strongly excited besides the transmitted beam (Figure 3.5(a)), is essential for the defect imaging in bright-field and dark-field imaging mode.

3.2.2 Bright field and dark field imaging

Quantitative analysis of crystal defect and chemical composition using diffraction contrast approach frequently needs careful comparison of bright-field and dark-field images.

To produce a bright-field image, the sample is oriented so that two-beam condition is satisfied and a small objective aperture is placed around the transmitted beam as shown in Figure 3.6(a). An image is formed by the removal of diffracted electrons from the primary beam that produces contrast as a result of the varying diffraction strength of different regions of the thin foil.

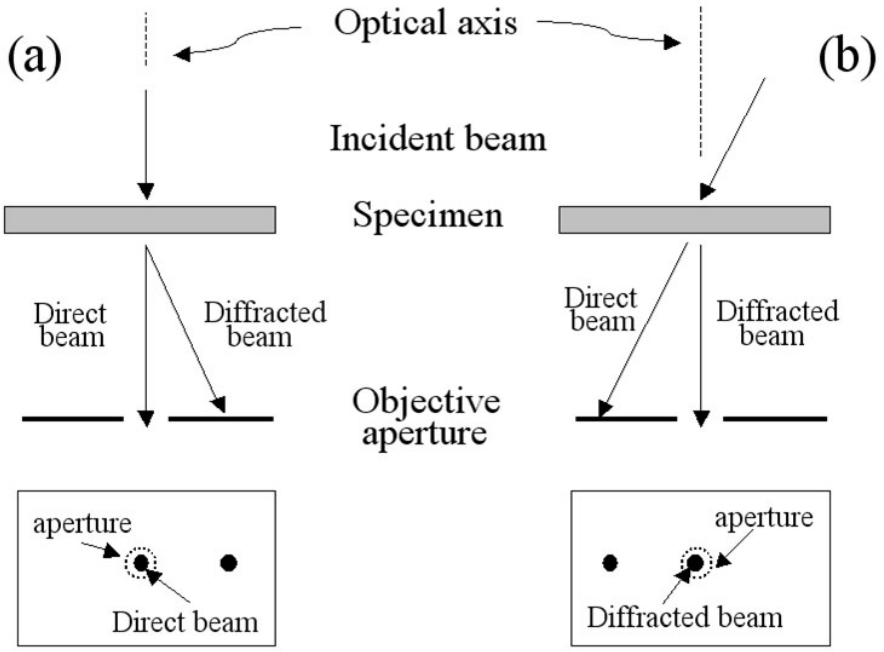

Figure 3.6: Ray diagram to show how to produce (a) Bright-field image and (b) Centered Dark-field image. The area selected by the objective apertures is present below each ray diagram [53].

Dark-field imaging is very useful in obtaining information from specific sets of crystal planes. In this mode, instead of selecting the diffracted electrons traveling off the optic axis, we tilt the incident beam to bring the scattered electrons traveling back down the optical axis as illustrated in Figure 3.6(b). This so-called centered dark-field imaging mode is used to avoid electrons suffering from lens aberrations and astigmatisms. The image contrast is again a result of the diffraction strength from different regions, but with a considerable number of unwanted scattering contributions removed. Depending on the reflections selected to form the image, dark-field imaging can be used to extract the compositional information. For instance, by choosing the chemical sensitive (002) reflection, one can identify (Al, Ga)As with variable Al concentration because they have different contrast intensity. With the superlattice reflection (001) selected in CoAl case, dark-field image can supply the spatial distribution of ordered and disordered phase.

Furthermore, dark-field imaging is very sensitive to the strain field and therefore can be utilized to analyze the defect structure in the specimen. It is generally performed under two-beam conditions. For a better interpretation of the diffraction contrast image, theoretical background of intensity distribution of diffracted beam should be clearly understood. Based on a number of assumptions, column approximation is adopted to simplify the mathematical calculation and to emphasis the underlying physical principles [53]. The column approximation is equivalent to the assumption that crystal can be divided into narrow columns. The amplitude of the beams in any such column can

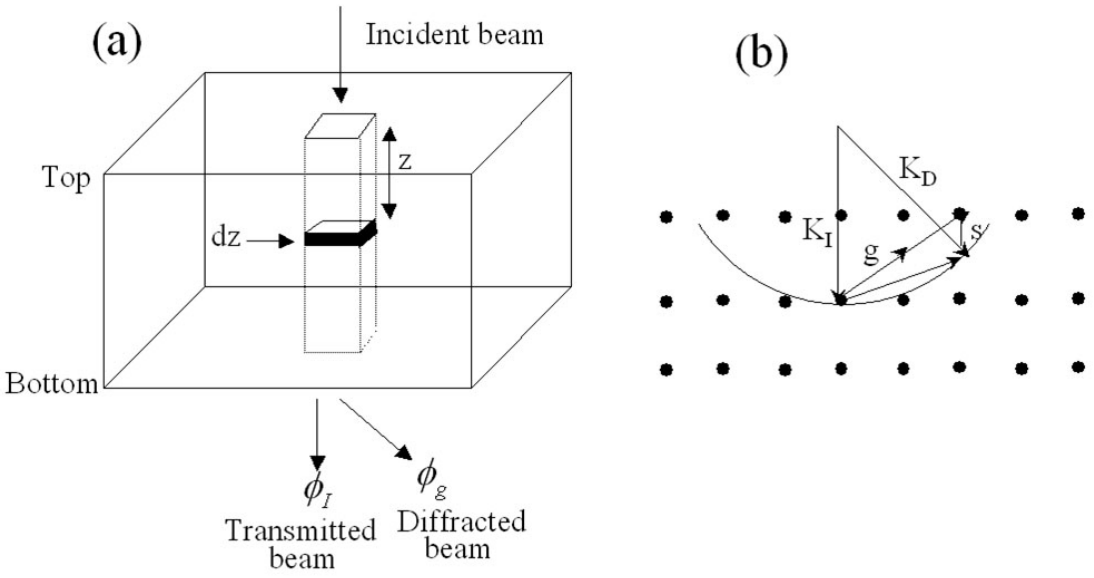

Figure 3.7: (a) The column approximation for a perfect crystal (b) introduction of deviation error factor s [53].

then be calculated as if the whole crystal is composed of an infinite number of identical columns. Figure 3.7(a) schematically illustrates the column approximation for a perfect crystal. From this approximation, we can obtain the unit amplitudes ϕ_0(transmitted) and ϕ_g (diffracted) as follows:

$$\mathrm{d}\phi_0 = \{\frac{\mathrm{i}\pi}{\xi_0}\phi_0 + \frac{\mathrm{i}\pi}{\xi_g}\phi_g \mathrm{exp}(2\pi \mathrm{i} s z)\}\mathrm{d}z \tag{3.5}$$

$$\mathrm{d}\phi_g = \{\frac{\mathrm{i}\pi}{\xi_0}\phi_g + \frac{\mathrm{i}\pi}{\xi_g}\phi_0 \mathrm{exp}(-2\pi \mathrm{i} s z)\}\mathrm{d}z \tag{3.6}$$

where z is depth, s is the deviation from the exact Bragg position as shown in Figure 3.7(b), and ξ_0 and ξ_g are the extinction distances.

For imperfect crystals, the displacement vector **R** that is the displacement of the atom from its proper position should be introduced. The equations corresponding to (3.5) and (3.6) are:

$$\mathrm{d}\phi_0 = \{\frac{\mathrm{i}\pi}{\xi_0}\phi_0 + \frac{\mathrm{i}\pi}{\xi_g}\phi_g \exp(2\pi \mathrm{i} s z) \exp(2\pi \mathrm{i} g R)\}\mathrm{d}z \tag{3.7}$$

$$\mathrm{d}\phi_g = \{\frac{\mathrm{i}\pi}{\xi_0}\phi_g + \frac{\mathrm{i}\pi}{\xi_g}\phi_0 \exp(-2\pi \mathrm{i} s z) \exp(-2\pi \mathrm{i} g R)\}\mathrm{d}z \tag{3.8}$$

Obviously, the imperfection introduces an additional phase factor $\exp(-2\pi i g R)$. When we form a dark-field image of a distorted crystal in electron microscope, we obtain a dark image with some brightness arising from the enhanced diffraction by the introduced displacement **R** of the crystal defect.

3.2.3 High-resolution TEM

High-resolution (HR) TEM is capable of providing specimen information on an atomic scale. To acquire an excellent high-resolution TEM image, the specimen should be tilted to a low index zone axis, leading to a strong transmitted beam and many diffracted beams from the different sets of atomic planes nearly parallel to the incident beam (Figure 3.5(b)). The multitude of beams is then collected with a large objective aperture in the microscope. It is the interference of these beams that generates an image that is essentially a reconstruction of the projected crystal potential.

A plane wave of unit amplitude is modified by the specimen resulting in the wave function at the existing surface, which is referred to as the transmission function $q(x,y)$ of the specimen. If the specimen changes only the phase of the incident wave, $q(x,y)$ is given by:

$$q(x,y) = \exp(i\sigma\varphi(x,y)t) \tag{3.9}$$

where σ is interaction constant, determined by the accelerating voltage of the microscope, and $\phi(x,y)$ is the projected electrostatic potential along incident electron direction. The phase change $\sigma\phi(x,y)$ induced by extremely thin foil is very small (weak phase-object approximation), and (3.9) could be further simplified using Taylor expansion:

$$q(x,y) \approx 1 + i\sigma\varphi(x,y)t \tag{3.10}$$

Noting the amplitudes of electron waves through the objective lens is the Fourier transform of $q(x,y)$. After propagation in the microscope, the final wave function is given by:

$$\psi(x,y) = F\{F[q(x,y)]T(\mathbf{u})\} \tag{3.11}$$

where F is Fourier transformation, $\mathbf{u}$ is the reciprocal space vector and $T(\mathbf{u})$ is the contrast transfer function. $T(\mathbf{u})$ has no amplitude contribution and it is given by:

$$T(\mathbf{u}) = A(\mathbf{u})E(\mathbf{u})\exp(i\chi(\mathbf{u})) \tag{3.12}$$

where $A(\mathbf{u})$ is the aperture function, $E(\mathbf{u})$ is the envelope function attenuating the higher spatial frequency and $chi(\mathbf{u})$ is the aberration function which presents the phase distortion induced by the electron wave length λ, the spherical aberration C_s and defocus Δf, written as:

$$\chi = \pi\Delta f\lambda u^2 + 0.5\pi C_s\lambda^3 u^4 \tag{3.13}$$

The image intensity I can be further obtained by $I = \psi^2(x,y)$.

HRTEM image is a phase contrast image. Correlating the HRTEM image with the atomic structure is generally not straightforward, because, for example, under different defocus values, a contrast reversal will appear, where the white dots corresponding to the atom column will transform into dark dots. Furthermore, if the distance between two atomic planes is too small and beyond the resolution of the microscope, these planes cannot be resolved in the phase contrast image. In order to bring the image back to the atomic structure, therefore, contrast simulation is essential to be performed and compared with the experimental image. Generally, there are four steps as following to quantitatively identify HRTEM contrasts:

- The modeling of the crystal structure or defect structure;
- The propagation of the incident electron save through the crystal slab;

- The transfer of the scattered by the optical system of the electron microscope;
- The quantitative comparison with the experimental micrographs.

The contrast simulation in the present work is based on the multislice method [124]. The crystal of thickness t is sliced into many thin slices of smaller thickness Δt, which ranges from 0.2 nm to 0.5 nm. For each slice the crystal potential is projected onto a plane, where the incident wavefront is scattered. The propagation of the modified wavefront to the next slice is done in vacuum over a small distance of Δt. The final image function can be obtained by a calculation of the transmission function over the thickness of t and the contrast transfer function of the microscope (cf. (3.11)). Factors that could affect the simulation are mostly known for a given TEM system. For instance, the microscope JEOL 3010 used in the present research is operating at 300 KV, and the values for spherical aberration, focus spread, semi-divergence angle and objective aperture diameter used in the computer simulation are set to 0.6 mm, 10 nm, 1.0 mrad and 20 nm^{-1}, respectively. If we assume the zone axis of the specimen is perfectly aligned to the electron beam, there are two crucial points needed to be considered: crystal thickness and defocus. Simulations are generally conducted over a wide range of defocus and sample thickness, compared and brought match with experimental micrographs.

3.3 Sample preparation

The TEM images presented in this work are obtained from thin-film samples prepared for analysis either in cross-section or plan-view. There are two main steps for preparation of cross-sectional samples: disc creation and disc thinning, as illustrated in Figures 3.8 and 3.9, respectively. (110) oriented samples are cleaved into roughly 2 mm wide strips along both in-plane [001] and $[1\bar{1}0]$ direction. These two stripes are then glued face to face with Gatan G1 epoxy between two dummies. The dummy is selected as the same material as the substrate to obtain the same ion-sputtering rate, which is GaAs in our case. The assembly is transferred into a 3 mm diameter metal tube, where the free space is filled with G1 epoxy that is then allowed to bake out and harden. At last, the metal tube is cut into slices of about 400 µm thick with a low speed diamond wire saw, which are ready for the following thinning process.

The slice is thinned by mechanical grinding with diamond paper. Progressively smaller paper grits are used in successive steps to achieve thinning and polishing at the same time. Afterwards, the sample is polished by using diamond paste of 3, 1 and $\frac{1}{4}$ μm grade sequentially. When no bright line (scratch) on the sample surface is observed in the optical microscope, the sample is flipped over and thinned to 80 μm. The sample is then ground and polished by a commercial dimple machine to a point where the thickness is below roughly 20 μm. The dimpling slurry is generally varied from 3 μm diamond paste at first, to 1 μm diamond slurry near the end.

The last step is the perforation of the dimpled sample by means of ion milling. Ion milling in this work is performed with a Gatan ion polishing system, which is equipped with two ion milling guns generating inert (Ar^+) ionic beams to thin the specimens from both sides. The milling is conducted by Ar^+ ions with incident angle of 3°, accelerating energy of 3 keV and beam current of less than 20 µA for about 1-2 hours. In some cases when the materials are very sensitive to ion bombardment, e.g. AlAs and Fe, we first choose large incident angle (5°) and high-energy (4.5 keV) Ar^+ ions to perforate the sample as soon as possible, then small angle (1°) and low energy (2.5 keV) ions are adopted to

remove the amorphous area. To reduce the damage, a cooling system operating at liquid nitrogen temperature is also employed.

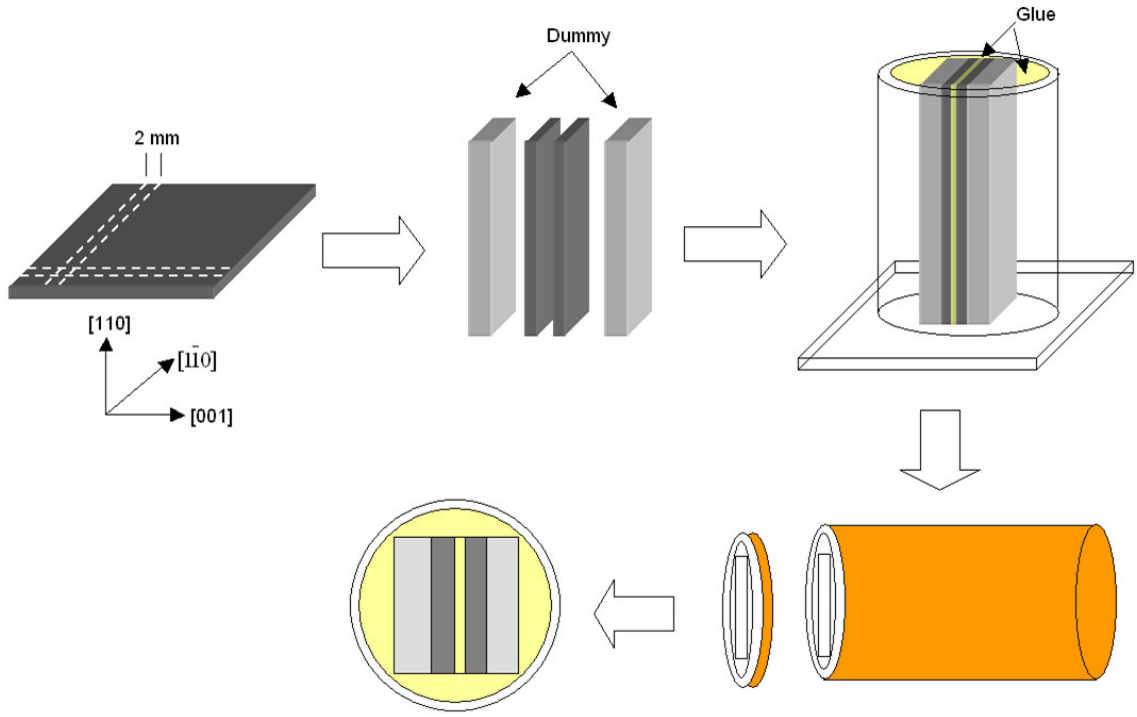

Figure 3.8: Schematic sequence for cross-section specimen preparation: the (110) oriented sample is cut into thin slices along two perpendicular in-plane directions that are face-to-face glued together between dummies. The assembly is filled into a 3mm diameter copper tube together with glue that is allowed to harden. The tube is then sectioned into disks with a diamond saw, which is ready for the following procedure.

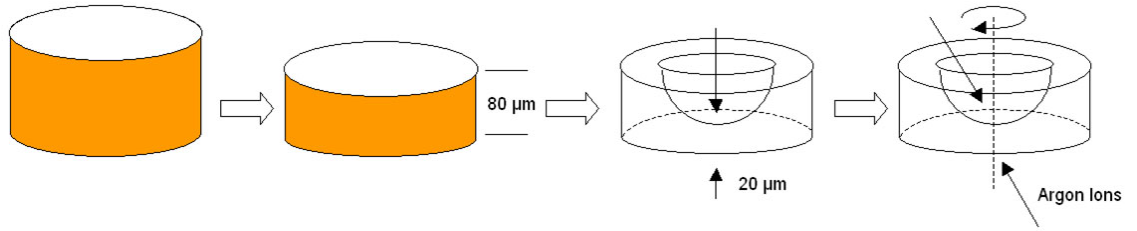

Figure 3.9: Schematic sequence for cross-sectional specimen preparation: The disk with specimen inside is mechanically thinned to 80 μm, followed by dimpling until the thickness reaches 20 μm. The assembly is then ion milled to perforation.

The TEM plan-view specimens are prepared in a similar procedure. We cleave 2 mm$\times$2 mm pieces from the specimen. The piece is thinned, dimpled and polished from the substrate side with the same technique described before. Both guns are tilted to the same side of the specimen. The incident angle and accelerating energy for Ar^+ ions is set to 6° and 5 keV respectively.

Chapter 4

Heterostructures on GaAs (110)

This chapter briefly reviews some general aspects of heterostructures grown on GaAs (110) in comparison with its well-studied (001) oriented counterpart. We start with the surface atomic configuration of GaAs (110) substrates. The elastic properties of (110) oriented cubic as well as hexagonal materials are then outlined. Afterwards, we discuss the different lattice mismatch strain relaxation mechanisms. A brief summary of the current research status on the microstructural analysis of (110) oriented heterostructures is presented at last.

4.1 Surface atomic configurations

A vast majority of studies of semiconductor epitaxial growth have been carried out on (001) oriented substrates, but there is both fundamental and technological interest in the epitaxial growth on (110) surfaces. For a better understanding of (110) oriented heterosystem, a comparison of microstructural properties between the structures grown on GaAs (110) and GaAs (001) is addressed.

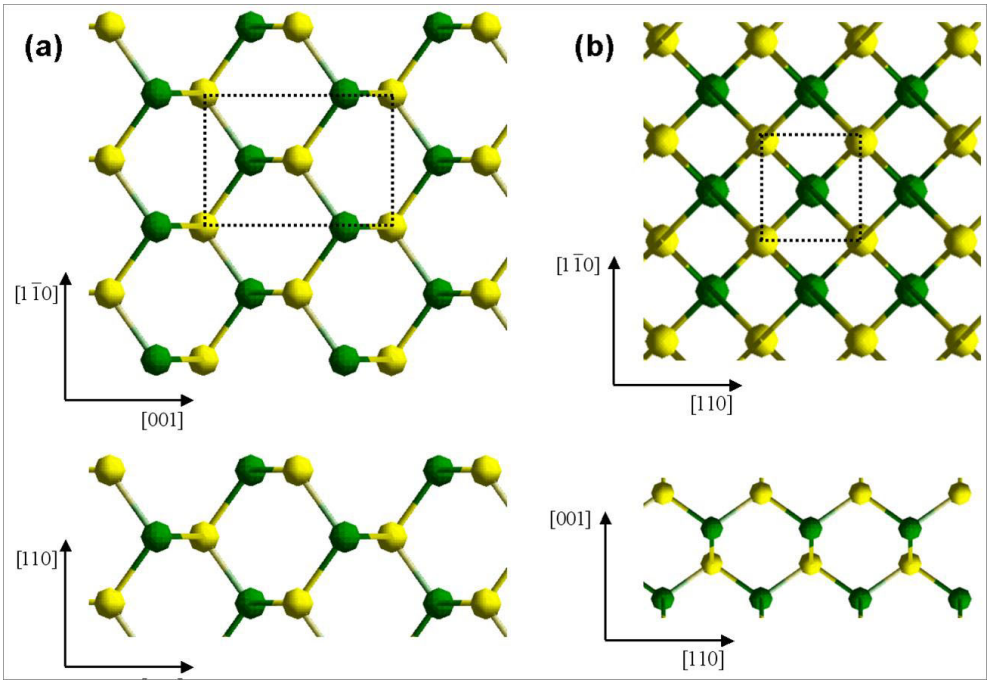

Figure 4.1: Surface atomic configuration of (a) (110) and (b) (001) oriented GaAs with their corresponding side views shown below. A unit mesh is indicated by dashed line in both figures.

Figure 4.1 illustrates the surface atomic configuration of GaAs with these two orientations. Different from the square unit mesh of its (001) counterpart, GaAs (110) surface is characterized by an rectangle, where the lattice spacing of {001} planes and $\{1\bar{1}0\}$ planes are 0.5653 nm and 0.3997 nm, respectively. Furthermore, GaAs (001) is a polar surface, terminated either by Ga or As atoms. In contrast, GaAs (110) is an unpolar surface with equal numbers of Ga and As atoms. The characteristic of GaAs (110) causes certain problem to the epitaxial growth, e.g. the missing surface reconstruction disables the precise in-situ control of growth parameters by RHEED [54].

4.2 Elastic Behavior

The microstructural evolution of the epilayer in heteroepitaxy is closely related to its elastic properties. Therefore, knowledge of elastic behavior of the heterostructure is of obvious importance.

The strain is the deformation of the crystal due to external stress. Since the rigid body rotation dose not induce any solid structure deformation, the strain tensor is symmetric and consists of normal strain components ε_{xx}, ε_{yy} and ε_{zz} as well as shear strain components ε_{xy}, ε_{yz} and ε_{zx}. The stress is the force per unit area that is acting on an oriented surface of the solid. In static equilibrium state there are no net forces or torques acting on the crystal. The stress is therefore symmetric and has a total number of six elements represented in a second-rank tensor, with three normal components σ_{xx}, σ_{yy} and σ_{zz} as well as three shear components σ_{xy}, σ_{yz} and σ_{zx}.

In the framework of linear elasticity, according to the Hooke's law, the stress of a material is directly proportional to the strain according to:

$$\sigma_{ij} = \sum_{kl} C_{ijkl}\varepsilon_{kl} \tag{4.1}$$

where C_{ijkl} is the tensor of elastic moduli. C_{ijkl} is normally a 6×6 matrix of elastic coefficients. If the envisaged material has some certain symmetry, the number of coefficients can be reduced substantially.

4.2.1 Cubic crystal on GaAs (110)

For cubic crystals, equation (4.1) could be expressed as:

$$\begin{bmatrix} \sigma_{xx} \\ \sigma_{yy} \\ \sigma_{zz} \\ \sigma_{yz} \\ \sigma_{zx} \\ \sigma_{xy} \end{bmatrix} = \begin{bmatrix} C_{11} & C_{12} & C_{12} & 0 & 0 & 0 \\ C_{12} & C_{11} & C_{12} & 0 & 0 & 0 \\ C_{12} & C_{12} & C_{11} & 0 & 0 & 0 \\ 0 & 0 & 0 & C_{44} & 0 & 0 \\ 0 & 0 & 0 & 0 & C_{44} & 0 \\ 0 & 0 & 0 & 0 & 0 & C_{44} \end{bmatrix} \begin{bmatrix} \varepsilon_{xx} \\ \varepsilon_{yy} \\ \varepsilon_{zz} \\ \varepsilon_{yz} \\ \varepsilon_{zx} \\ \varepsilon_{xy} \end{bmatrix}. \tag{4.2}$$

In the simple case of a (001) cube-on-cube orientation, the coherently strained epilayer is described by an equal biaxial strain ε^0, leading to:

$$\varepsilon_{xx} = \varepsilon_{yy} = \varepsilon^0 \tag{4.3}$$

With the knowledge that the layer is free of stress along the growth axis ($\sigma_{zz} = 0$), we can obtain the elastic stresses along different in-plane directions based on the equation

(4.2) and (4.3). The (001) oriented structure has an isotropic biaxial elastic stress, which is given by [55]:

$$\sigma_{xx} = \sigma_{yy} = (C_{11} + C_{12} - \frac{2C_{12}^2}{C_{11}})\varepsilon^0 \tag{4.4}$$

However, for a film deposited on GaAs (110), the elastic properties are not symmetric. The elastic modulus along the mutually perpendicular [001] and $[1\bar{1}0]$ direction is different. The stresses could be written as [55]:

$$\sigma^{[001]} = \{C_{11} + C_{12} - \frac{C_{12}(C_{11} + 3C_{12} - 2C_{44})}{(C_{11} + C_{12} + 2C_{44})}\}\varepsilon^0 \tag{4.5}$$

$$\sigma^{[1\bar{1}0]} = \{\frac{(2C_{11} + 6C_{12} + 4C_{44})}{4} - \frac{(2C_{11} + 2C_{12} - 4C_{44})}{4}\frac{(C_{11} + 3C_{12} - 2C_{44})}{(C_{11} + C_{12} + 2C_{44})}\}\varepsilon^0 \tag{4.6}$$

The resulting direction dependent elastic stresses lead to a direction dependent critical layer thickness and relaxation mechanism. Note due to the anisotropic stresses along mutually perpendicular in-plane directions, the unit cell in the film will be deformed with its surface normal no longer parallel to the growth direction. Consequently, the elastic stress along the growth direction is a nonzero value, e.g. $\sigma^{[110]}$ should not be equal to zero for (110) oriented cubic heterostructure, which introduces to an error in calculating the elastic modulus. However, since this discrepancy is quite small, we neglect such effect in the current thesis.

4.2.2 Hexagonal crystal on GaAs(110)

In case of hcp crystal, (4.1) is expressed as the following form:

$$\begin{bmatrix} \sigma_{xx} \\ \sigma_{yy} \\ \sigma_{zz} \\ \sigma_{yz} \\ \sigma_{zx} \\ \sigma_{xy} \end{bmatrix} = \begin{bmatrix} C_{11} & C_{12} & C_{13} & 0 & 0 & 0 \\ C_{12} & C_{11} & C_{13} & 0 & 0 & 0 \\ C_{13} & C_{13} & C_{33} & 0 & 0 & 0 \\ 0 & 0 & 0 & C_{44} & 0 & 0 \\ 0 & 0 & 0 & 0 & C_{44} & 0 \\ 0 & 0 & 0 & 0 & 0 & C_{44} \end{bmatrix} \begin{bmatrix} \varepsilon_{xx} \\ \varepsilon_{yy} \\ \varepsilon_{zz} \\ \varepsilon_{yz} \\ \varepsilon_{zx} \\ \varepsilon_{xy} \end{bmatrix}. \tag{4.7}$$

The elastic coefficient matrix C_{ijkl} contains six elastic modules, five of which are independent and $C_{66} = (C_{11} - C_{12})/2$. Here ε_{xx} and ε_{yy} denote the strain along the mutually perpendicular directions in the basal plane. ε_{zz} represents the strain normal to the basal plane along **c** direction.

The elastic status the hexagonal film is dependent on the epitaxial orientation relationship with respect to the substrate. If the hcp crystal has its prism plane parallel to the GaAs surface, the elastic stresses are acquired as [126]:

$$\sigma^{[11\bar{2}0]} = \frac{(C_{11}^2 - C_{12}^2) \cdot \varepsilon^{[11\bar{2}0]} + (C_{11} - C_{12})C_{13} \cdot \varepsilon^{[0001]}}{C_{11}} \tag{4.8}$$

$$\sigma^{[0001]} = \frac{(C_{11}C_{33} - C_{13}^2) \cdot \varepsilon^{[0001]} + (C_{11} - C_{12})C_{13} \cdot \varepsilon^{[11\bar{2}0]}}{C_{11}} \tag{4.9}$$

4.3 Strain relaxation

Besides the anisotropic elastic modulus, the epitaxial strain relaxation of (110) oriented structure is further complicated by some other aspects. Taken zinc-blende structure as an example, the (110) oriented structure is characterized by a lower critical thickness and a reduced number of slip systems as compared to its (001) counterpart.

According to MB method via equation (2.7), the calculation of critical thickness requires the consideration of the appropriate value of $\cos\beta$. Taking zinc-blende crystal as an example, $\cos\beta$ varies as $\cos\beta_{(100)} = 0.50$ and $\cos\beta_{(110)} = 0.707$ for $\langle 110\rangle\{111\}$ glide system, representing a lower critical layer thickness of (110) oriented structure as compared to its (100) counterpart [24, 37].

Since the slip planes are the close-packed planes with the largest separation, the geometric difference of (001) and (110) oriented heterostructures could result in different activated slip systems. For zinc-blende structure on GaAs (001), $a/2\langle 110\rangle$ misfit dislocations glide on the two groups of {111} planes as shown in Figure 4.2(a), and form 60° dislocations along both [110] and $[1\bar{1}0]$ direction after relaxation. However, for (110) oriented structure, only one set of slip planes are activated and effective to relieve the strain because there is no resolved shear stress onto the dislocations lying in $(1\bar{1}1)$ and $(\bar{1}11)$ planes. Figure 4.2(b) schematically illustrates the slip systems of heterostructures on (110) surface, where dislocation with in-plane direction $[\bar{1}10]$ is formed only for the relaxation along the [001] direction [24, 41, 56]. Mismatch relaxation along the perpendicular $[\bar{1}10]$ needs activation of a secondary glide system.

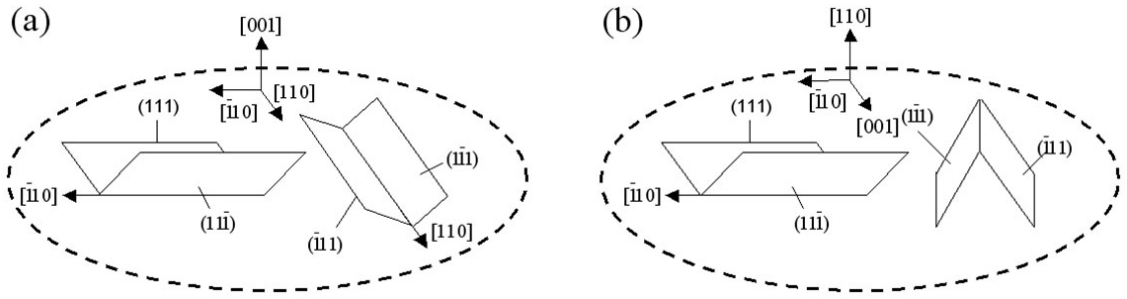

Figure 4.2: Geometry of the 111 slip planes in zinc-blende crystal on the (a) (001) and (b) (110) GaAs substrate.

4.4 Current research status

Comparing with (001) substrate, the epitaxial growth with (110) surface is affected by a smaller critical thickness, a possible anisotropic in-plane mismatch stress and a reduced number of active glide systems, which would deteriorate the growth and induce a distinctive way of strain relaxation. There is, however, only a very limited literature on the growth and microstructure of heteroepitaxial layers on (110) substrates. Among them, InAs/GaAs (110) is the most widely studied case, mainly because growth of InAs on GaAs (110) substrates proceeds in a 3D island mode forming compositionally abrupt interface [57], which is essential for the electronic behavior of device. The relaxation of this system is highly asymmetric, with the formation of two perpendicular sets of misfit dislocations of distinct characters. Due to the lack of the slip systems, strain relief

in $[\bar{1}10]$ is achieved by a group of 90° dislocations lying along [001] with $b = 1/2[\bar{1}10]$, which are deposited from the edge of expanding InAs islands. The relaxation in $[\bar{1}10]$ is almost completed during the nucleation stage. Along the perpendicular [001] direction, conventional 60° dislocations are formed along $[\bar{1}10]$ by the expansion of half loops on the activated {111} planes as shown in Figure 4.2(b). With the increase thickness of the epilayer, the density of 60° dislocations increases indicating a higher relaxation extent [41, 57-59]. First principle calculation method is also employed to study the interfacial stability and misfit dislocations of InAs/GaAs (110) [60-62], which show excellent agreement between the predicted critical thickness and the experimental data. Similar relaxation mechanism has been observed in Ge_xSi_{1-x}/Si(110) [56, 63], where a number of stacking faults exist formed by the dissociation of the 60° dislocations. It is shown that 60° dislocations are preferable to form if the epilayer thickness is larger than a certain value, while the stacking faults are encouraged to form when the thickness is smaller than that value. The formation of stacking faults is also found in InGaAs/GaAs (110) [64-66] and $In_{0.1}Ga_{0.9}As$/GaAs(110) [41, 59] where the lattice mismatch is smaller than that of InAs/GaAs (110). The 90° partial dislocations relieve the strain along [001] direction in combination with the 60° perfect one. At lower mismatch system, e.g. $In_{0.1}Ga_{0.9}As$/GaAs(110), 90° perfect dislocations for the relaxation along the $[\bar{1}10]$ direction do not exist anymore due to the reduced strain energy. Only 60° dislocations and stacking faults are present until the activation of secondary slip system when the epilayer thickness is larger than a certain value. Dislocations along $\langle 1\bar{1}2\rangle$ directions are formed by the slip on the inclined {131} planes for the relaxation in both [001] and $[\bar{1}10]$ directions [41, 59].

Overall, most of available researches only deal with large mismatched single heterostructure of fcc type. Therefore, it is of great importance and interest to investigate the microstructure of epilayers grown on GaAs(110), which are defined by different symmetries.

Chapter 5

Microstructure of (Al,Ga)As/AlAs/GaAs superlattice on GaAs (110)

This chapter treats fcc-type (Al,Ga)As/AlAs/GaAs multilayer stacks grown on GaAs (110). Comparing with its (001) counterpart, (110) oriented structure is affected by a smaller critical thickness, and therefore, an effective way to stabilize the system against plastic relaxation is highly desired. We start with the mismatch strain accommodation mechanisms. Short period superlattice (SPSL) is introduced to the system to stabilize the structure. Defect-free structures are successfully acquired by an appropriate SPSL composed of AlAs/GaAs. Finally, nano-indentation tests are applied to the defect-free sample to verify the effect of SPSL on strain relief.

5.1 Introduction

Strained-layer superlattice structure composed of fcc-type (Al,Ga)As/AlAs/GaAs on GaAs (110) is chosen for the first case study. Different from the available results for highly mismatched single heterostructure, the present structure is characterized by a low lattice misfit and a large number of interfaces. Investigation of relaxation mechanism and the effect of superlattices is therefore very interesting. Other than that, the system is technologically attractive. Besides the longer spin lifetime, the spintronic device property may be further improved by embedding the quantum well structure into a microcaivity because of an enhanced conversion efficiency of photons to electrons. However, the performance of such device is degraded by the appearance of misfit dislocations caused by strain relief of the lattice mismatch. The exact knowledge of the strain state and relaxation mechanism is, therefore, a prerequisite for the applicability of such heterostructures in the optical devices.

5.2 Sample growth

Prior to growth, all GaAs (110) substrates are smoothened by GaAs grown in migration enhanced epitaxy mode. Three different samples are grown by MBE at a temperature of 490°C and a beam equivalent pressure ratio of 45. The layout of the samples is presented in Table 5.1. The detail layer sequences of distributed Bragg reflectors (DBRs) are illustrated schematically in Figure 5.1. They are designed for the wavelength (λ) within the range from 810 nm to 980 nm, which allow the use of GaAs quantum wells or (In,Ga)As quantum wells as well. For samples A and B, the growth rate of GaAs, AlAs and $Al_{0.33}Ga_{0.67}As$ is 800 nm/h, 400 nm/h and 1200 nm/h respectively, while for sample C, the growth rate of both GaAs and AlAs is 500 nm/h. Within the growth, interruptions for annealing are performed to reduce surface step density [67].

Table 5.1: Sample design.

Sample	Nominal Structures	Total thickness t
A	10-pair DBR$^{[a]}$	1.3 μm
B	15.5-pair DBR$^{[a]}$/Cavity/1-pair DBR$^{[a]}$	2.3 μm
C	10.5-pair DBR$^{[b]}$/Cavity/5-pair DBR$^{[b]}$	2.1 μm

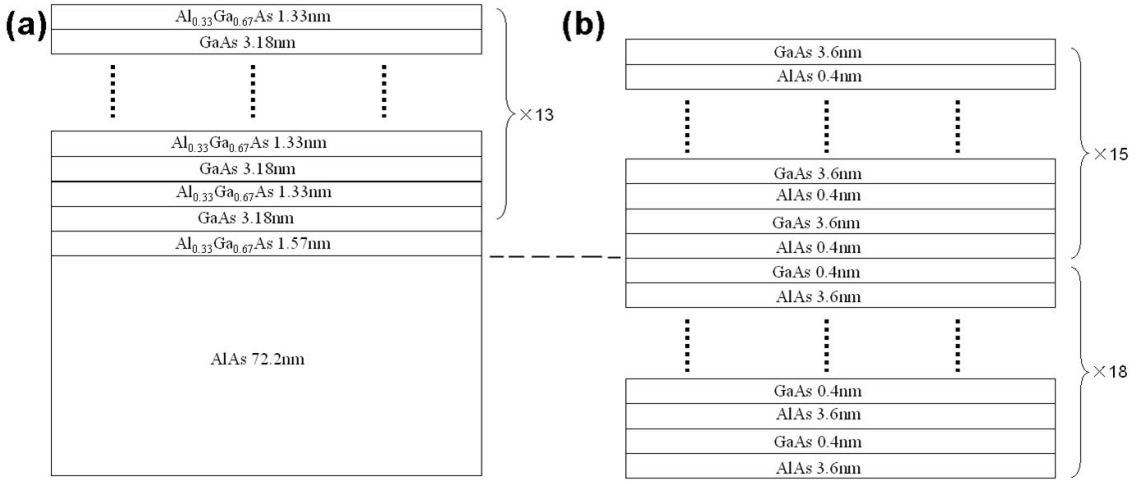

Figure 5.1: Stacking structures of (a) DBR$^{[a]}$ and (b) DBR$^{[b]}$.

5.3 Relaxation mechanism

Using Matthews-Blakeslee relation (2.7) for a single heterostructure, the relations between the critical thickness h_c vs ε^0 are summarized for zinc-blende structures grown on GaAs (110) and (001) substrates in Figure 5.2, with respect to the 60° misfit dislocation. Obviously, the (110) oriented structure is characterized by a much smaller critical thickness as compared to its (001) counterpart.

The dotted line in Figure 5.2 denotes the strain for AlAs on GaAs. The calculated critical layer thickness for (110) oriented AlAs on GaAs amounts to about 66 nm. Such value is much smaller than the entire thickness of the strained stacks in sample A of about 0.65 µm, and therefore, plastic relaxation should be initiated as evidenced by the cross-sectional dark-field image in Figure 5.3. Very few planar defects are detected along the {111} planes running through multilayer structure. In order to determine the character of these planar defects, a high-resolution electron microscopy study has been carried out. It is found that most of the planar defects are nanotwins in addition to stacking faults.

Perfect dislocations in zinc-blende structure such as GaAs are almost invariably of the type $(a/2)\langle 110\rangle$ since their Burgers vectors are equal to primitive lattice vectors of the crystal in this case. These dislocations can dissociate into two $(a/6)\langle 112\rangle$ Shockley partial dislocations within the {111} glide plane according to the following equation:

$$\frac{a}{2}[10\bar{1}] = \frac{a}{6}[11\bar{2}] + \frac{a}{6}[\bar{2}11] \tag{5.1}$$

After dissociation, the partial dislocations glide apart and leave a stacking fault ribbon between. The type of leading partial dislocation depends on the sign of misfit and the

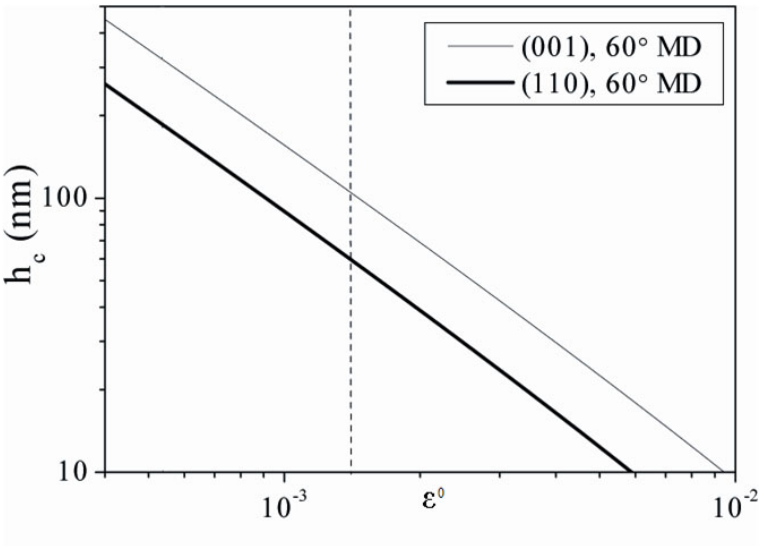

Figure 5.2: Critical thickness h_c as a function of the strain ε^0 for (001) and (110) oriented zinc-blende structures with respect to 60° misfit dislocation. The dashed line denotes the strain for AlAs and GaAs.

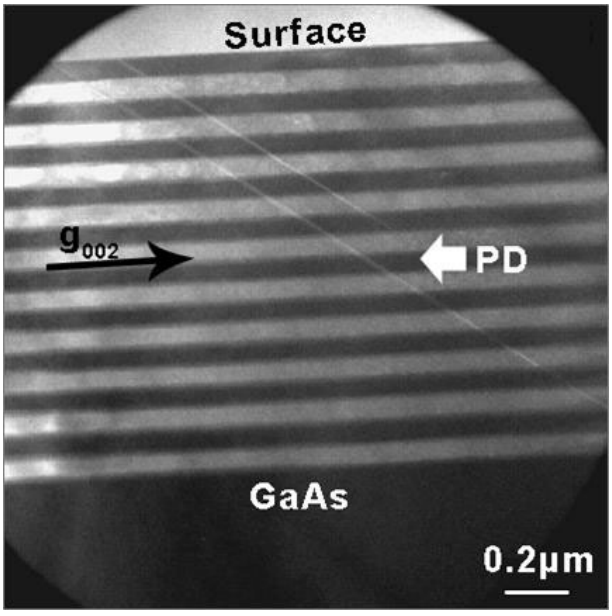

Figure 5.3: Cross-sectional bright-field TEM image of Sample A with $\mathbf{g} = 002$ (PD: planar defect).

geometry of substrate. As in our experiment, for (110) oriented substrate and compressive strain field, the geometrical arrangement of the atoms on the glide planes requires leading 90° partial dislocation [24, 37]. The HRTEM image in Figure 5.4(a) illustrates an intrinsic SF bounded with a 90° partial dislocation. The formation mechanism of the nanotwin is not clarified yet. A possible explanation is that a second SF formed by the similar dissociation process appears on an adjacent plane to a preexisting one. The second 90° partial dislocation glides into the stack until a stable equilibrium position is achieved between the misfit-induced driving force and the repulsive force between the two partial

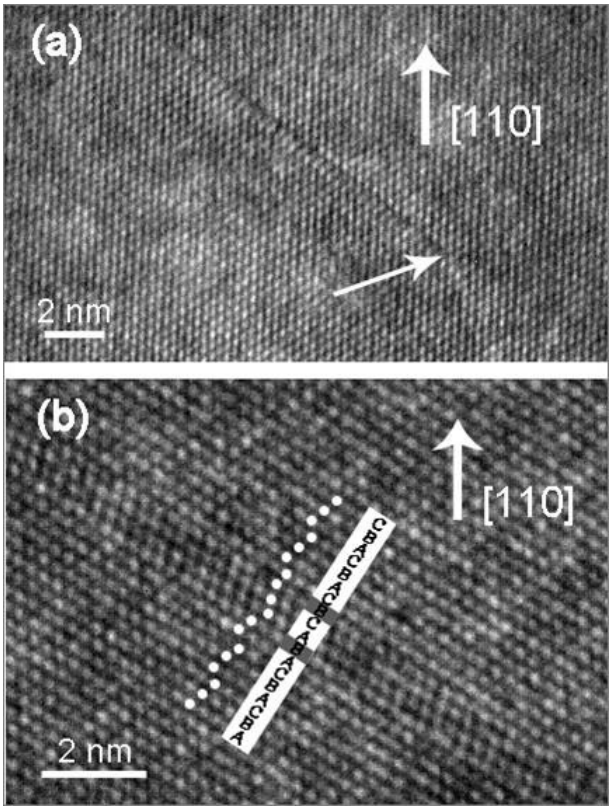

Figure 5.4: High-resolution TEM images of planar defect in the relaxed SPSL taken along the $[1\bar{1}0]$ direction. (a) Intrinsic stacking fault, a 90° partial dislocation is arrowed (b) nanotwin.

dislocations with identical Burgers vectors. In this manner, the intrinsic SF changes into an extrinsic SF and a nanotwin is generated after a continuation of this process [38] as shown in Figure 5.4 (b). Note that 90° partial dislocations at the interface to the substrate give rise to the strain relief only in the [001] direction.

By adding a (Al,Ga)As/GaAs cavity with 15.5-pair DBR$^{[a]}$ below and 1 pair DBR$^{[a]}$ on top (Sample B), the thickness of the whole film is increased to about 2.3 μm as well as the accumulated strain energy. Consequently, the number of planar defects with strain relieving partial dislocations is enhanced, which is demonstrated by the cross-sectional TEM image in Figure 5.5(a). As described in Chapter 4, the partial dislocations bounding the planar defects can only relive strain along the [001] direction, plastic relaxation in the perpendicular $[1\bar{1}0]$ direction requires an alternate slip system $\langle 110\rangle\{113\}$ [59]. The activation of slip systems is critically determined by the resolved shear stress. Combining equation (2.4) and (4.2), we may acquire the resolved shear stress τ given by:

$$\tau = M_{[hkl]}\varepsilon^0_{[hkl]}\cos\beta\cos\phi \tag{5.2}$$

where the anisotropic biaxial elastic behavior between different in-plane directions must be taken into account according to (4.5) and (4.6). Using the lattice mismatch between AlAs and GaAs, the calculation results are shown in Table 5.2, from which $\langle 110\rangle\{113\}$ slip system should become active in the latter stage of the relaxation due to the lower resolved shear stress compared to that one applied to the {111} planes.

The geometry of primary and secondary sliding systems on (110) surface is shown

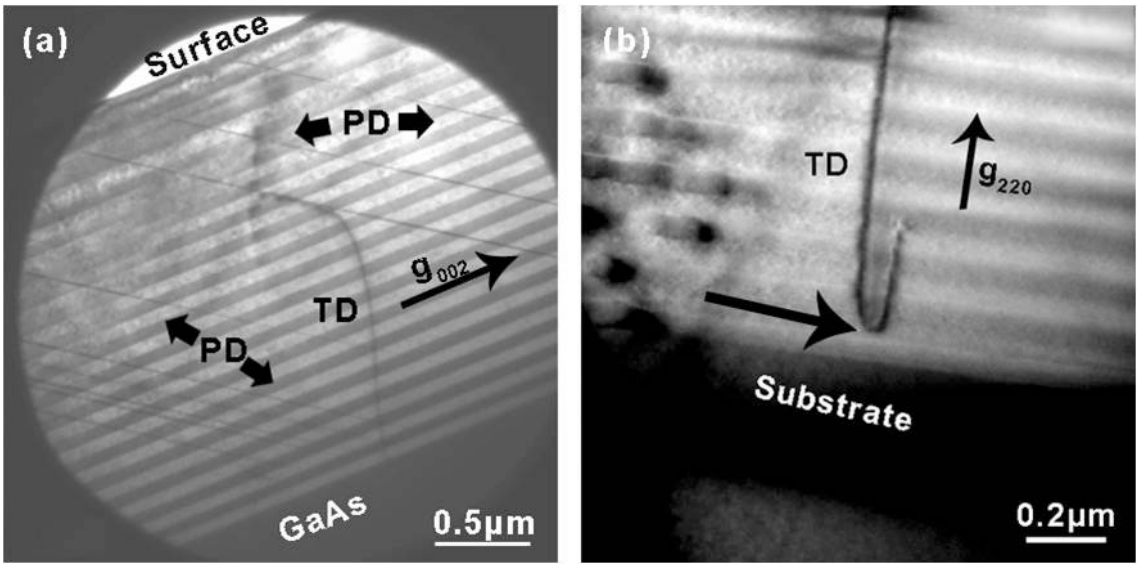

Figure 5.5: Cross-sectional bright-field images of sample B taken with (a) $[1\bar{1}0]$ and (b) [001] projection (TD: threading dislocation). A misfit dislocation is indicated by an arrow in (b).

Table 5.2: Comparison of resolved shear stress (GPa) for $\langle 110\rangle\{113\}$ and $\langle 110\rangle\{111\}$ slip systems.

	[001]	$[1\bar{1}0]$	sum
$\langle 110\rangle\{111\}$	1.14	0	1.14
$\langle 110\rangle\{113\}$	0.30	0.56	0.86

graphically in Figure 5.6. The strain energy in sample B is large enough for the activation of the $\langle 110\rangle\{113\}$ slip system and relaxation along the $[1\bar{1}0]$ direction starts by introducing dislocation half loops on the {113} glide plane. Figure 5.5(b) shows such a dislocation half loop with Burgers vector $\mathbf{b} = 1/2\langle 110\rangle$. Due to the projectional TEM view along the [001] direction, the loop on the {113} plane appears contracted and also the length of the misfit dislocation part along the interface (marked by arrow). This group of misfit dislocations is able to relieve strain in both [001] and $[1\bar{1}0]$ directions.

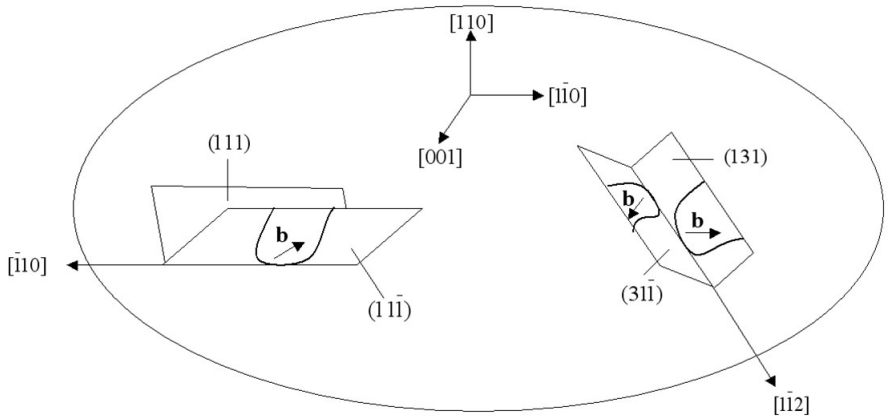

Figure 5.6: Schematic diagram of the geometry of the slip systems on (110) oriented substrate.

According to equation (2.4) and (2.8), the residual strain of Sample B can be roughly estimated, indicating that 40% of lattice mismatch along the [001] direction and 90% along the $[1\bar{1}0]$ direction is still not relaxed. Although the critical thickness is widely exceeded, the degree of plastic relaxation is still rather low, which indicates the superlattice structure may play a role of suppressing the misfit dislocation formation and glide

5.4 Influence of SPSL

For the fabrication of optically efficient quantum well samples, the generation of the defects related to strain relaxation has to be prevented. Therefore, in the following step, sample C with both $\lambda/4$-thick components of the DBRs composed of SPSL is prepared. Figure 5.7(a) shows the cross-sectional image of sample C revealing an overview of the microstructure. The higher magnified dark-field image in Figure 5.7(b) taken under $\mathbf{g} = 002$ condition illustrates the multilayer structure, which is characterized by a high periodicity and sharp hetero-interfaces. The faint lines in the micrograph denote the SPSLs, whose corresponding high-resolution lattice image is shown in Figure 5.7(c). The thickness of the individual layers of the SPSL is about 4 nm and 0.6 nm, respectively, with 1-2 monolayers fluctuations in consistence with the nominal value. Obviously, the introduction of SPSL prevents the generation of MDs.

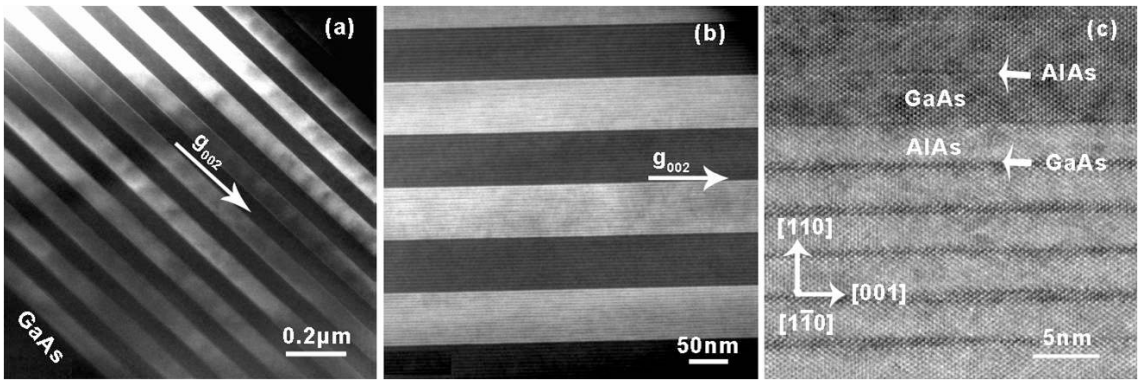

Figure 5.7: Cross-sectional TEM images of Sample C (a) overview and (b) detail dark-field image with $\mathbf{g} = 002$ and (c) lattice image taken along the $[1\bar{1}0]$ direction.

SPSL, if embedded between the substrate and the active layers, can be used as a filter to prevent the threading dislocation from propagating into epilayers. The strain present in the superlattices makes the threading dislocation confined in the superlattice region and bend at the interface, depositing misfit dislocation for the relaxation of the lattice mismatch [68-70]. Pseudomorphical growth beyond the critical thickness by using SPSL was reported before for $(InAs)_m(GaAs)_n$[71], due to the balance between surface and interface free energies. Regarding to the current study, a possible explanation of the system stabilization is that SPSL could improve the smoothness of the interfaces and accordingly reduce the amount of centers with sufficiently low energetic barriers for the nucleation of misfit dislocations. However, by comparing the lattice images of the interfaces of sample A and sample B as shown in Figure 5.8 with that of sample C (Figure 5.7(c)), it seems that such explanation is not applicable because thickness fluctuations and interface roughness collectively exist in these three samples.

Generally speaking, a mechanical view of the kinetics of strain relaxation via misfit

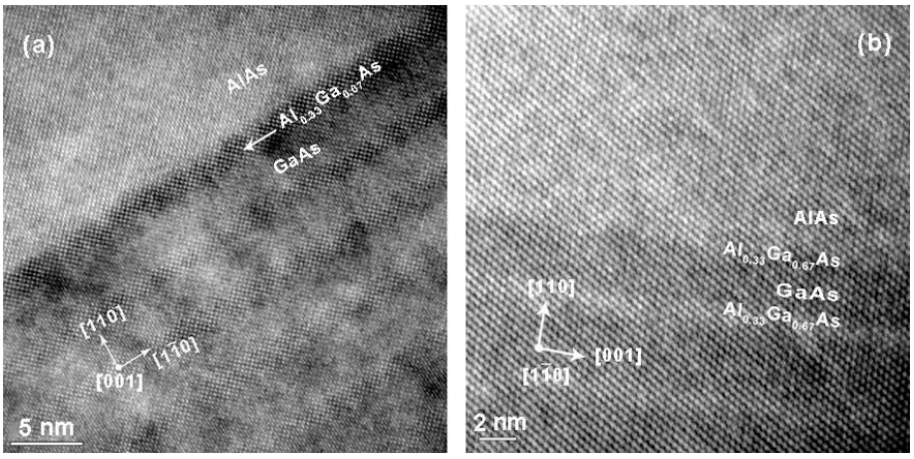

Figure 5.8: Cross-sectional high-resolution TEM images of (a) Sample A along the [001] direction and (b) Sample B taken along the $[1\bar{1}0]$ direction.

dislocation formation in strained layer structures should consider dislocation nucleation and propagation. If we neglect the controversial multiplication mechanisms [72], there are two candidates for dislocation nucleation, known as homogeneous nucleation and heterogeneous nucleation at specific local stress centers.

The concept of homogeneous nucleation contains a growing loop that relieves a certain amount of mismatch strain, in balances with the loop's self-energy and the surface step energy created in the nucleation process [24]. The total energy of the loop would pass through a maximum value, known as activation energy, at a critical loop radius R_c. When the loop is larger than the critical size, it is thermodynamically favorable to expand itself until reaching the interfaces when it forms a MD segment. Otherwise, homogeneous nucleation is not preferable. According to the equation proposed by Hull [24], the critical loop radius R_c corresponding to $\varepsilon^0_{[hkl]}$ is given by:

$$R_c = \frac{\mu b^2}{8\pi M_{[hkl]}\varepsilon^0_{[hkl]}} \frac{[\frac{b_z^2}{b^2} + (1-\frac{v}{2})(1-\frac{b_z^2}{b^2})][\ln(\frac{2\pi\alpha R_c}{b} - 1.758)]}{(b_g \cos\phi\cos\beta + b_e\cos^2\phi)} \tag{5.3}$$

where b_e, b_g and b_z are the glide, climb and loop-normal components of Burgers vector. For the current case with 60° misfit dislocation moving on {111} planes, the critical radius is calculated as 98 nm. This corresponds to a layer thickness of 80 nm based on $h_c = R_c \cos\phi$. Such value is much larger than the individual layer thickness of SPSL. Consequently, the formation of a critical loop has to overcome the energy barriers from many heterointerfaces, which in turn enhances the activation energy of the critical loop and thereby make homogeneous nucleation of dislocation loops less probable.

On the other hand, heterogeneous nucleation of threading dislocation and dislocation loop would be possibly initiated at the preexisting stress centers, such as interface roughness in Figure 5.7(c). Since threading dislocation could be considered as one arm of the dislocation loop, we only take into account the situation where there is a heterogeneously nucleated dislocation loop in the film as schematically illustrated in Figure 5.9.

The motion of the loop along the interface could be best described by the confined layer slip model, which is based on the hypothesis that plastic flow is initially confined to one layer and occurs by the motion of single hairpin dislocation loop [73-76]. The

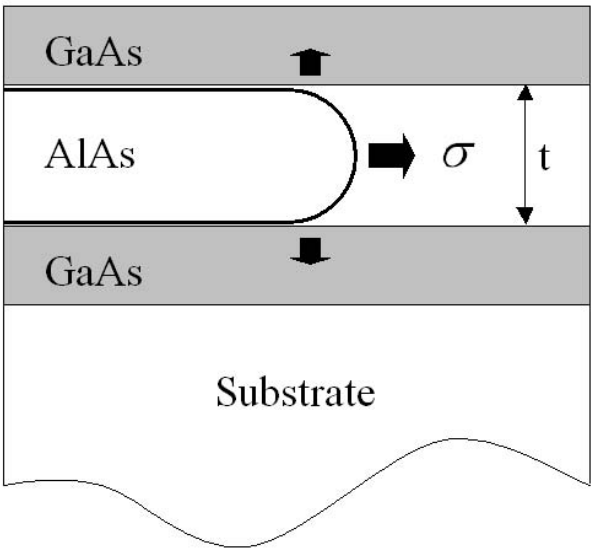

Figure 5.9: Schematic illustration of the expansion of a dislocation loop.

critical stress required to achieve the bowing process is known as Orowan force. It is proportional to $\ln t/t$, where t is the thickness of the soft AlAs layer that contains the loop. It is obvious that the critical stress increases with decreasing layer thickness, and the lateral expansion of the loop is accordingly more difficult. The same trend also holds for the large dislocation loop cutting across several layers [76]. Actually, the lateral expansion of the dislocation loop introduces misfit dislocation segments at both interfaces. With the identical Burgers vector, these two misfit dislocations are affected by a repulsive force between each other, which is inversely proportional to the distance between the misfit dislocations, i.e. the thickness of AlAs. If the distance is relatively low, this repulsive force is neglectable. However, when the thickness comes to the order of the nanometer as in our case, such repulsive force must be considered. The repulsive force becomes larger and larger with decreasing thickness, making the lateral expansion of the loop and the formation of misfit dislocations unfavorable.

A propagating dislocation loop along the growth direction has to cross the interfaces. When a dislocation moves from a soft to a hard layer, in addition to other configurational resistance arising from structural effects of the interface itself, an extra force must be applied to overcome the "Koehler barrier", which is known as the maximum difference of the image forces on a dislocation segment in the two neighboring materials [77]. As in our experiment, when a pure AlAs layer in Sample B is replaced by GaAs/AlAs SPSL in Sample C, the propagation of the loop parallel to the growth direction has to overcome the Koehler barrier between AlAs and GaAs layer, making the expansion much more difficult. A. Misra's simulation [75] also suggests that interfaces act as barriers for transmission of a dislocation. The stress field of a glide dislocation approaching the interface can locally shear a weak interface, leading to dislocation absorption and core spreading along the interface. Re-nucleation of the glide dislocation on the other side of the interface requires an extremely high stress because of the relaxed core configuration of the dislocation along the interface. One thing worth noting here is that when the layer thickness is of the size of the Burgers vector, the interface barrier to slip transmission decreases because the dislocation core effect has to be taken into account. However, comparing with the system stabilization acquired by the SPSL, this negative effect is neglectable.

In conclusion, SPSL suppresses the homogeneous nucleation of dislocation loops. Even if there are heterogeneously nucleated dislocations, the reduced individual layer thickness and plenty of interfaces from SPSL play against their propagation. Therefore, the introduction of SPSL makes the formation of dislocation unfavorable and pseudomorphic growth is realized far beyond the critical thickness.

5.5 Verification of the stabilization effect of SPSL by nano-indentation test

For the verification of the effect of SPSL against the propagation of the dislocation, plastic deformation is introduced to the defect-free sample C intentionally by nano-indentation. The deformation is conducted by a Berkovitch diamond pyramid using a MTS XP indenter, which runs at room temperature in the force-control mode of the machine. A 10×12 array of indents are produced onto each stripe of the sample as shown in Figure 5.10 before the subsequent standard TEM preparation procedure. This is designed for a better chance to acquire a specimen containing at least one dislocation for TEM investigation.

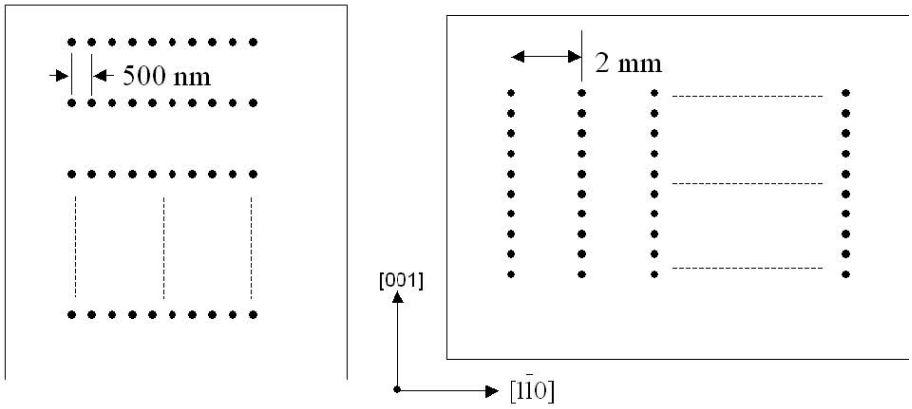

Figure 5.10: Schematic diagram of the array of the indents.

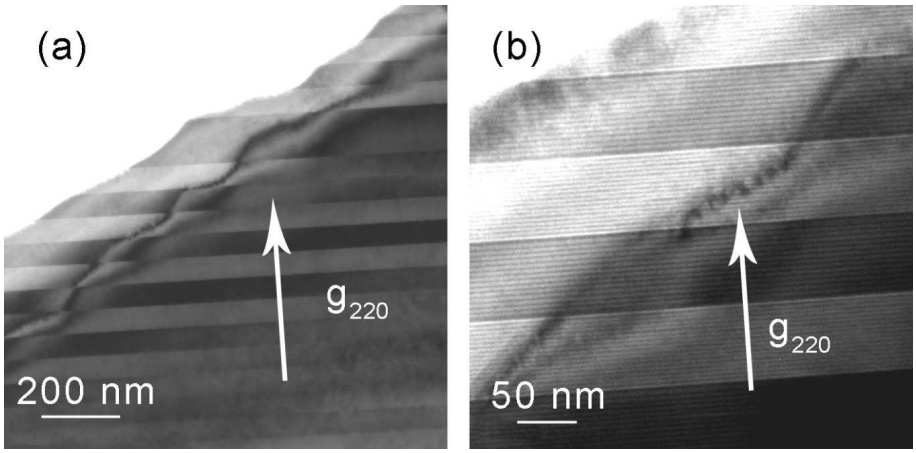

Figure 5.11: Cross-sectional TEM images of indentation-induced dislocation (a) overview BF image and (b) detail BF image, $\mathbf{g} = 220$.

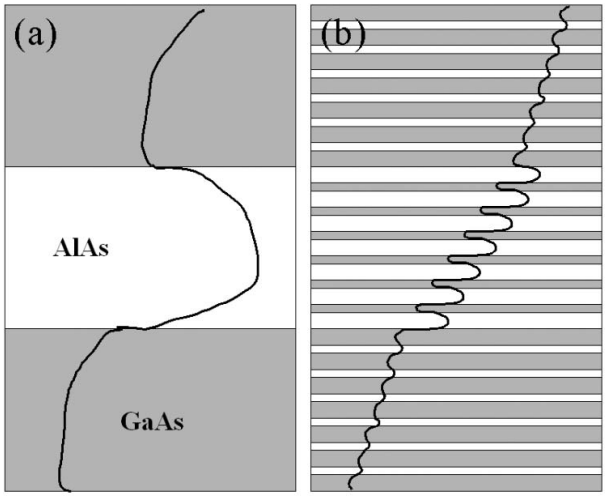

Figure 5.12: Schematic illustrations of the propagation of a dislocation in (a) Superlattice (b) SPSL, gray and white area refers to GaAs and AlAs, respectively.

Subsequently, the indented sample C is investigated by TEM to clarify how the dislocation propagates in these SPSL. The cross-sectional BF image in Figure 5.11(a) illustrates a wavy dislocation running through the whole structure. Comparing with the GaAs-rich layer (dark contrast), the curvature of the dislocation in AlAs-rich layer (bright contrast) is larger. With higher magnification as shown in Figure 5.11(b), it is found that the dislocation in AlAs-rich layer displays as a spiral shape, and loses this character when it extends to GaAs-rich layer. When a dislocation runs through a multilayer structure, it tends to glide along the interfaces and present a bow shape in the layer because of the different elastic property of two neighboring materials. The curvature of the bow is dependent on the shear modulus and the thickness of the layer. It becomes larger with the smaller shear modulus and larger layer thickness. For example, the curvature of the dislocation in AlAs layer is larger than that in GaAs layer of the same thickness (cf. Figure 5.12(a)), because of the higher shear modulus of GaAs as compared to AlAs. When a SPSL is introduced into the stack, the dislocation would react with interfaces in the same manner. In AlAs-rich layer, the dislocation propagates zigzag (Figure 5.12(b)), which appears spiral-like in Figure 5.11(b). The dislocation in GaAs-rich layer presents straightly in Figure 5.11(a), because the variation is so small that it is beyond the resolution limit of the BF imaging. The bowing of the dislocations is trivial even under a high external stress induced by the nano-indentation. Therefore, the reduced individual layer thickness and plenty of interfaces from SPSL are indeed unfavorable for the lateral propagation of the dislocation.

Chapter 6

Microstructure of MnAs on GaAs (110)

In this chapter, we report on the microstructure analysis of hexagonal MnAs epilayers grown on GaAs (110) by MBE. TEM investigations reveals the presence of a wetting layer prior to the formation of MnAs islands on GaAs (110) substrates, indicating that hexagonal MnAs grows epitaxially on GaAs via the Stranski-Krastanov mode. The symmetry break at the MnAs/GaAs interface leads to anisotropic lattice mismatches, which are accommodated either elastically or by the generation of an array of localized interfacial misfit dislocations. The elastic distortion associated with the array of dislocations is dominantly constrained at the interface within a thickness of about 3.4 nm. Subsequent growth of GaAs on MnAs is three-dimensional with a huge amount of planar defects present.

6.1 Introduction

The integration of magnetic and semiconductor materials has attracted much attention because of the prospect of utilizing both the electron charge and spin in future optoelectronic devices [18]. However, the search for suitable ferromagnetic materials remains an elusive goal because many candidates differ in crystal structure and chemical bonding with the semiconductor substrates [4]. MnAs, which is ferromagnetic at room temperature, has been extensively studied in combination with GaAs as a candidate for spintronic devices. Despite their different crystal symmetry and chemical bonding, MnAs is not only convenient to fabricate on GaAs due to the common group V element, but also thermodynamically stable in contact with the substrate [79, 80]. A major challenge for the spintronic application is the transport of spin-polarized carriers across a certain distance, which is affected by the quality of the interface, because the strain field may scatter and relax the spin of the electron [3]. Considering the difference in symmetry and large lattice mismatch between MnAs and GaAs, the basic understanding of the strain relaxation mechanism and interfacial structure is of obvious necessity for the understanding of the principles of the device performance based on such heterostructures.

Besides its technological importance, the combination of a hexagonal NiAs type MnAs (cf. Figure 6.1) with a zinc-blende structure GaAs is also interesting as a unique model system for extreme heteroepitaxy, which could be recognized as an example to discuss the underlying basic principles of heteroepitaxy and the influence of the interface structure on the strain and defect formation. Other than that, MnAs undergoes magnetoelastic phase transitions accompanying with discontinuous volume changes. According to Mn and As phase diagram [81], paramagnetic hexagonal NiAs type γ-MnAs exists above 125°C, and orthorhombic MnP type β-MnAs comes into being between 125 and 45°C. When the temperature drops below 45°C, ferromagnetic hexagonal NiAs type α-MnAs is present. During the second order phase transformation from β-MnAs to α-MnAs, the lat-

tice parameter **a** increases abruptly by about 1% with declining temperature, while lattice parameter **c** remains essentially unchanged as shown in Figure 6.2. Such films are very attractive for investigating the fundamental physical properties that may be changed in comparison with bulk properties.

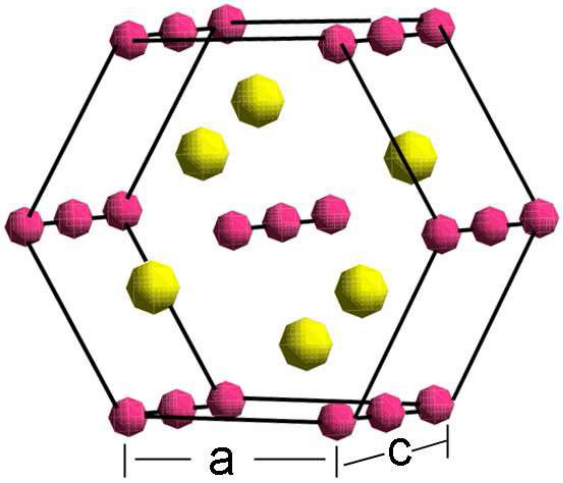

Figure 6.1: Atomic model of NiAs-type MnAs (Mn and As atoms are drafted by small red and large yellow spheres, respectively).

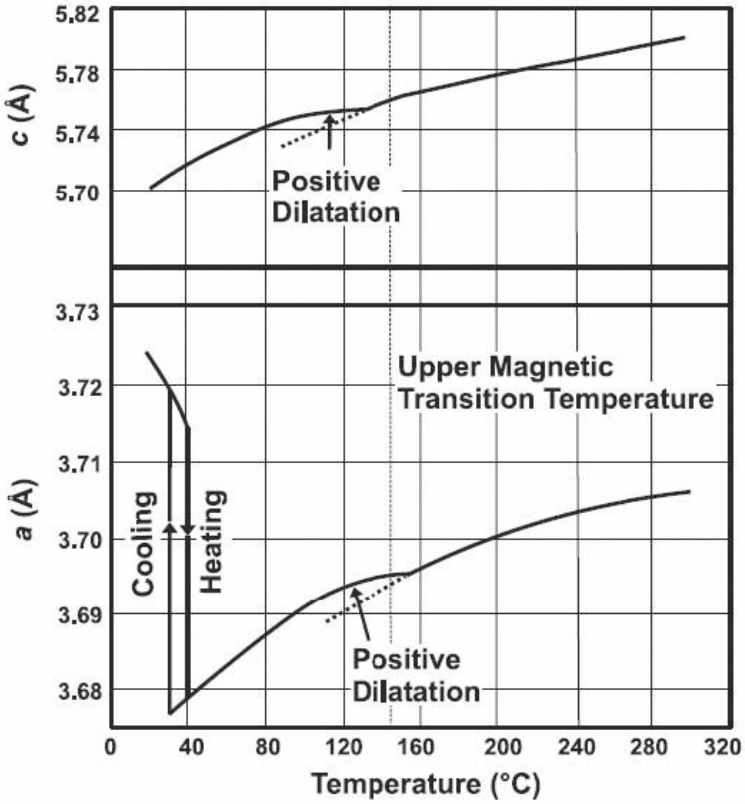

Figure 6.2: Variations of the unit cell dimensions of MnAs with temperature (reproduced after [82]).

MnAs grows epitaxially on GaAs (001) [83, 84] and (113)A [85] substrates, with its $(1\bar{1}00)$ prism plane parallel to the substrate surface. In these cases, the symmetry break at the interface results in an asymmetric character of the interface structure and thus of a direction dependent misfit parameter, leading to an anisotropic process of mismatch accommodation: the formation of a coincidence site lattice along the highly mismatched direction and the generation of an array of localized interfacial misfit dislocations along the low mismatched direction. In addition, the epitaxy of MnAs on GaAs (111) substrates [86-88] is characterized by the fact that the basal plane of MnAs matches the GaAs (111) surface, resulting in an isotropic misfit, which is also accommodated by a coincidence lattice with a small residual strain left. However, there is an obvious lack of the structural study of MnAs grown on GaAs (110). The present chapter presents a detail study of the microstructure of (110) oriented MnAs, including the growth mode, the lattice misfit accommodation mechanism, the atomic configuration of the interface and the overgrowth of GaAs on MnAs.

6.2 Sample growth

The hexagonal MnAs thin films are deposited on cubic GaAs (110) substrate by standard solid-source molecular-beam epitaxy. After growing a 280 nm GaAs buffer layer at 600°C for the realization of well-defined surface for the subsequent growth, the template is transferred to MnAs chamber and the substrate temperature is reduced to 250°C. MnAs layers with variable thicknesses are grown there with a rate of 20 nm/h and an As_4/Mn beam equivalent pressure (BEP) ratio of 200. The Mn flux is calibrated by RHEED intensity oscillations. The As_4 fluxes keep very high to acquire As coverage of GaAs (110) template which is preferable for the growth of MnAs with the only desired orientation [18]. Thereafter, the template is transferred back to the GaAs chamber. A nominally 6 nm thick GaAs is overgrown there with a growth rate of 115 nm/h and under As4/Ga BEP ratio of 5. The substrate temperature is preserved at 250°C, because the normally applied higher temperature for GaAs growth could induce Mn clustering in the MnAs epilayer [89]. Afterwards, the substrate is cooled to room temperature with a rate of 1°C per minute.

6.3 MnAs on GaAs(110)

The orientation relationship of MnAs on GaAs (110) is determined by in situ RHEED and ex situ SAED. The electron diffraction patterns reveal that the $(1\bar{1}00)$ lattice plane of MnAs is parallel to the GaAs (110) substrate surface and the in-plane GaAs [001] ($[1\bar{1}0]$) direction is parallel to MnAs [0001] ($[11\bar{2}0]$) axis resulting in the following relationship:

$$\mathrm{MnAs}(1\bar{1}00)||\mathrm{GaAs}(110) \text{ and } \mathrm{MnAs}[11\bar{2}0]||\mathrm{GaAs}[1\bar{1}0].$$

Thus, the natural lattice mismatch f along the MnAs $[11\bar{2}0]$ and [0001] direction, respectively, is -7.5% and 0.7%, if we take as a basis the bulk lattice parameters of GaAs ($a = 0.565$ nm) and MnAs ($a = 0.371$ nm and $c = 0.570$ nm). A plan-view of the interface geometry is indicated in Figure 6.3 summarizing the results of the orientation relation and the lattice mismatches.

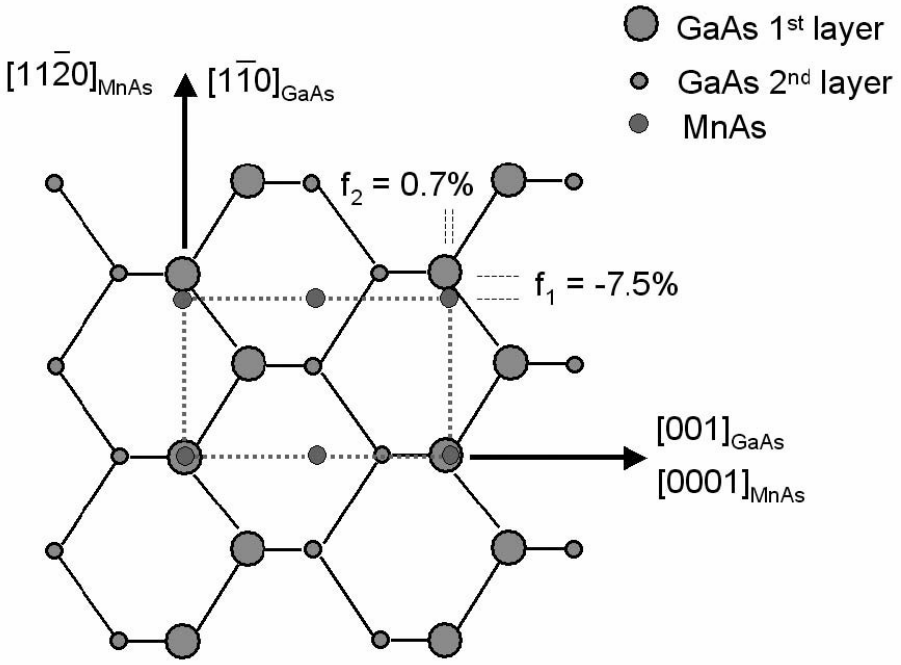

Figure 6.3: Schematic illustration of the MnAs/GaAs (110) heterostructure in plan-view (f represents the lattice mismatch).

6.3.1 Growth mode

Figure 6.4(a) displays a typical cross-sectional HRTEM micrograph of the sample with nominally 3 nm MnAs taken along the $[11\bar{2}0]_{MnAs}||[1\bar{1}0]_{GaAs}$ direction. For such a low coverage, three-dimensional (3D) flat MnAs islands are observed. These islands are characterized by (0001) planes as side facets and the $(1\bar{1}00)$ plane as the top of surface.

In addition, as it is highlighted by the ellipse in Figure 6.4(a), we find an extra bright band along the substrate surface, as well as along the interface to the MnAs island. The appearance of this bright contrast may indicate that there is a very thin layer deposited on top of the substrate. For verification of this finding, the interplanar spacings are measured by intensity line scans across the interface using the DigitalMicrograph^{TM} program and the substrate surface from a highly magnified image as shown in Figure 6.4(b). The profile of the surface region reveals a change of spacing from 0.403±0.005 nm, corresponding to the GaAs (110) plane, over 0.432±0.005 nm to 0.321±0.005 nm. This obvious variation demonstrates the existence of additionally deposited material different from that of the GaAs substrate. Comparing this result with a profile measurement of the interface between the island and the substrate, which shows almost the same trend from 0.401±0.005 nm to the MnAs $(1\bar{1}00)$ spacing of 0.327±0.005 nm with a distance of 0.427±0.005 nm in between, we conclude that a MnAs wetting layer is deposited prior to the formation of 3D islands. It should be clarified here that neither the value of 0.432±0.005 nm nor 0.427±0.005 nm corresponds to the real interfacial width (cf. Chapter 6.3.3) because of the lack of contrast analysis. The growth of MnAs on GaAs (110) proceeds via a layer plus island growth, i.e., in the Stranski-Krastanov mode. The extra bright layer at the interface is a result of the special interfacial atomic configuration, which will be discussed in detail later.

From the thermodynamic point of view (cf. Chapter 2.1.2), the growth modes are

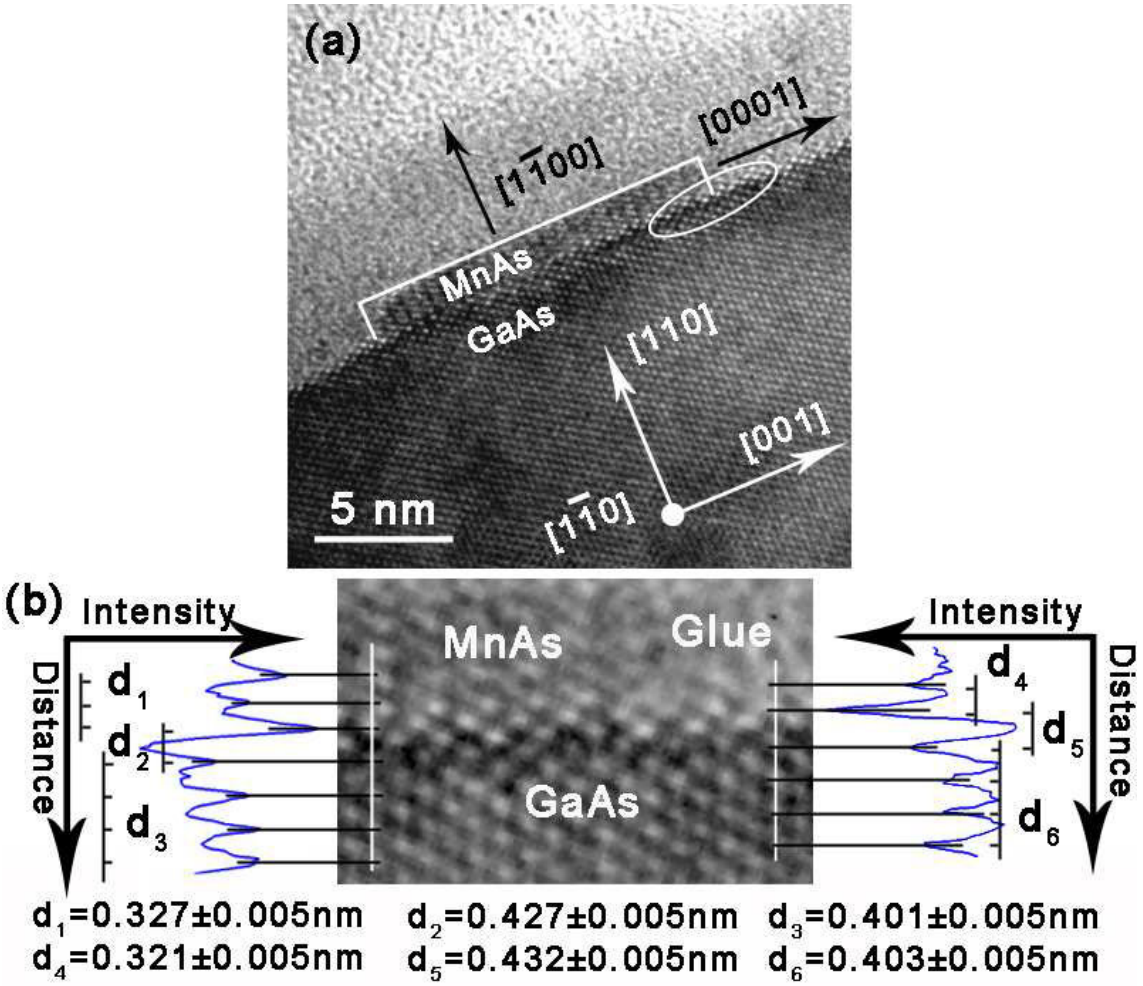

Figure 6.4: (a) Cross-sectional HRTEM image of the 3 nm thick MnAs grown on GaAs (110) along the $[11\bar{2}0]_{MnAs}||[1\bar{1}0]_{GaAs}$ direction. The area in the ellipse is magnified in (b). An accurate measurement of the lattice plane spacing at the interface and substrate surface region is obtained by a scan along the white line in the image.

dominated by the relative combination of the surface free energies of substrate, overlayer, the interface energy γ_i and the strain energy γ_ε. A wetting layer is formed prior to the formation of islands during the heteroepitaxy of MnAs onto GaAs (110), implicating the satisfaction of the following equation [106]:

$$\gamma_{MnAs} + \gamma_i + \gamma_\varepsilon \leq \gamma_{GaAs} \tag{6.1}$$

where γ_{MnAs} and γ_{GaAs} represent the surface free energies of MnAs and GaAs, respectively. Such equation indicates $\gamma_{MnAs(1\bar{1}00)} < \gamma_{GaAs(110)}$. The wetting behavior of MnAs on GaAs is primarily depending on the specific epitaxial orientations of the heterosystem, from which different lattice mismatch values related to the interfacial strain energy are expected between the film and the substrate. In case of MnAs/GaAs (001) [107], where a large mismatch of about 30% is involved, a Volmer-Weber type of nucleation is favored at the initial stage of the epitaxial growth. However, similar as the current study, 2D nucleation is preferable for (111) oriented MnAs/GaAs [108], because only a mismatch of -7.5% is present, indicating a relatively small interfacial strain energy, which

leads to a temporary satisfaction of the above equation at the initial growth stage. As the growth continues, the strain energy increases with the increasing film thickness, and consequently leads to the violation of the above equation. Thereafter, 3D MnAs islands are formed to minimize the total energy.

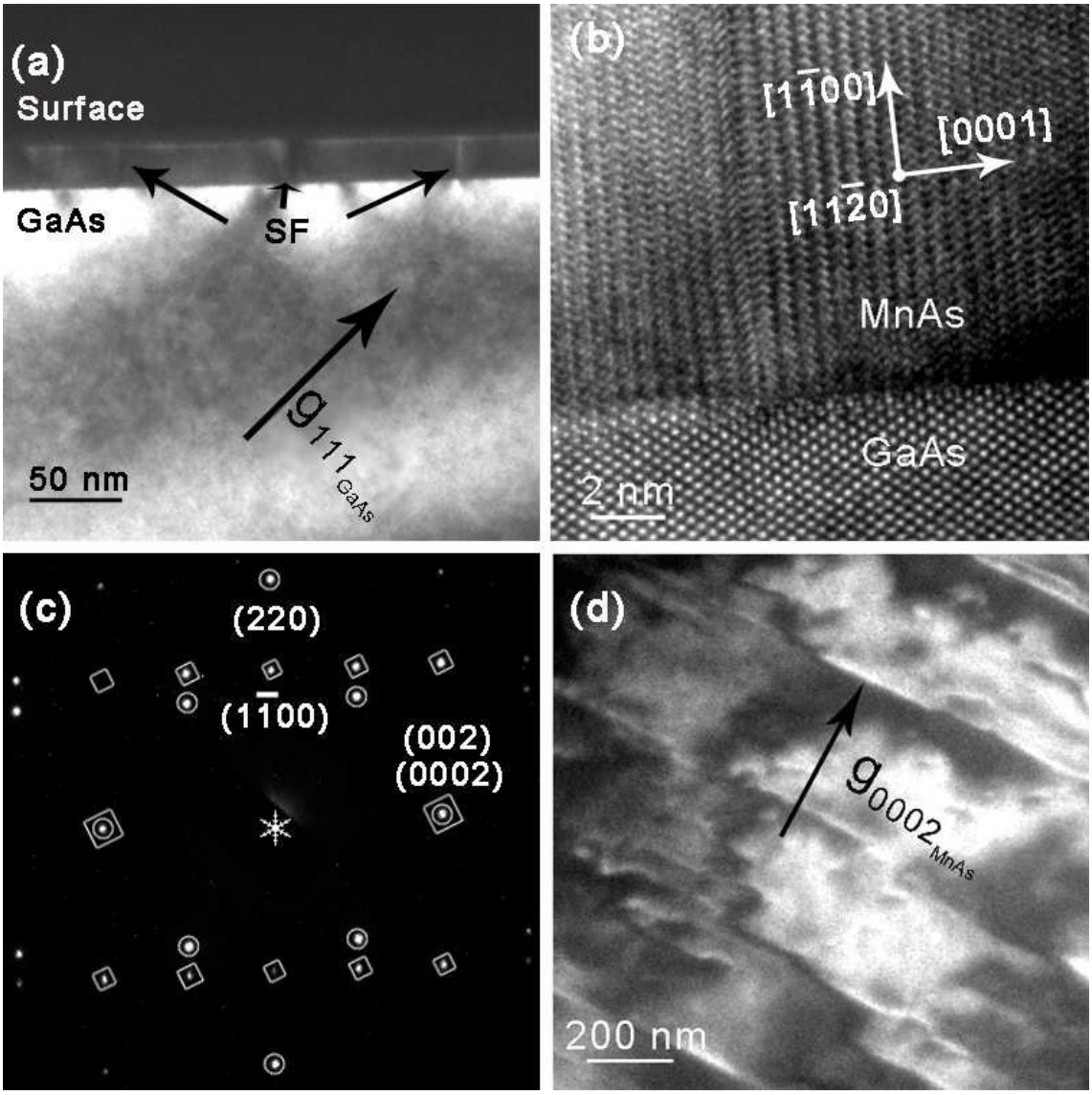

Figure 6.5: (a) A cross-sectional dark-field image of 30 nm MnAs on GaAs (110) along the $[11\bar{2}0]_{MnAs}||[1\bar{1}0]_{GaAs}$ direction with $\mathbf{g} = 111_{GaAs}$. (b) High-resolution micrograph of the interface with its SAED pattern shown in (c) (Circle = reflections of GaAs; square = reflections of MnAs). (d) Plan-view weak-beam dark-field image recorded with $\mathbf{g} = 0002_{MnAs}$.

With continuing growth, a smooth film develops from the individual islands as shown in Figure 6.5(a) for the sample with 30 nm MnAs. The abrupt change in contrast reflects a clear and chemically sharp boundary without any indication of an extended interfacial phase. The bright lines crossing the film are clearly observed as expected for basal plane stacking faults, which are demonstrated by the high-resolution micrograph along the $[11\bar{2}0]_{MnAs}||[1\bar{1}0]_{GaAs}$ direction as shown in Figure 6.5(b). Plan-view weak-beam dark-field TEM image (Figure 6.5(d)) confirms their existence. The stacking faults are perpen-

dicular to the substrate surface, and therefore, they appear as lines in plan-view. These basal plane stacking faults are unlikely to be formed through a traditional glide process of partial dislocations with mismatch relaxation involved due to the lack of resolved shear stress on $(0001)_{MnAs}$ planes. Considering the fact of the MnAs islands with {0001} facets as their side-surfaces, we conclude that the main reason of the stacking fault formation is the coalescence of MnAs islands [90]. Except for basal plane stacking faults, no dislocation or other relaxation-related defects are observed at the interface, implying that the film is still coherently strained along this direction. This is reasonable because the layer is still too thin for the initialization of plastic relaxation. It is confirmed by the SAED pattern along this projection as shown in Figure 6.5(c), where separation between (0002) reflection of MnAs and (002) refection of GaAs is not observed.

6.3.2 Periodic dislocation array at the interface

From the perpendicular $[0001]_{MnAs}||[001]_{GaAs}$ projection, the lattice image of 3 nm MnAs sample (Figure 6.6(a)) confirms the presence of islands, which have $(1\bar{1}00)$ top surfaces and $(11\bar{2}0)$ side of facets. Together with the previous TEM results, the observation represents most of the 3D islands are rectangular shapes, which have a larger side length along the $[11\bar{2}0]$ direction. During epitaxial growth, the atoms are preferentially adsorbed at island ledges before new atomic steps are formed on perfect close-packed crystal planes [91], i.e. 0001 planes in our case. Thus, the growth rate is lower along the [0001] direction, leading to the rectangular island with a larger side length along the $[11\bar{2}0]$ direction.

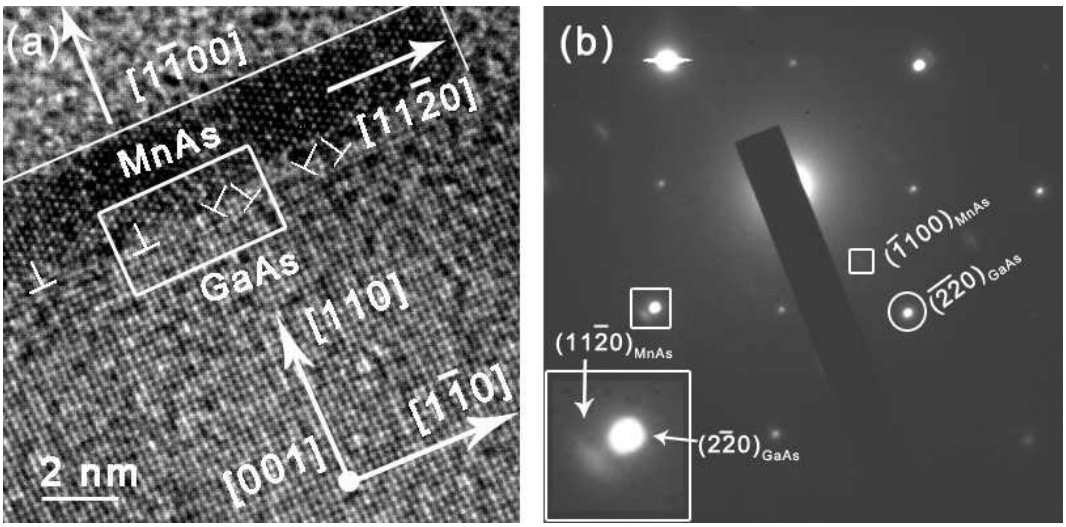

Figure 6.6: (a) Cross-sectional HRTEM image of 3 nm MnAs grown on GaAs (110) and the corresponding SAED pattern (b) with the electron beam parallel to the $[0001]_{MnAs}||[001]_{GaAs}$ direction.

The MnAs films appear homogeneous. No granular morphology is visible, which would be expected in the presence of orientation or phase variations. SAED pattern in Figure 6.6(b) indicates that the islands are almost completely relaxed along the $[11\bar{2}0]_{MnAs}$ direction, in accordance with the presence of an array of misfit dislocations along the hetero-boundary as verified in Figure 6.7(a), which is a magnified image of the semi-coherent interface region marked by the rectangle in Figure 6.6(a). The atomic structure of the dislocations can be directly interpreted by HRTEM only if they have their line di-

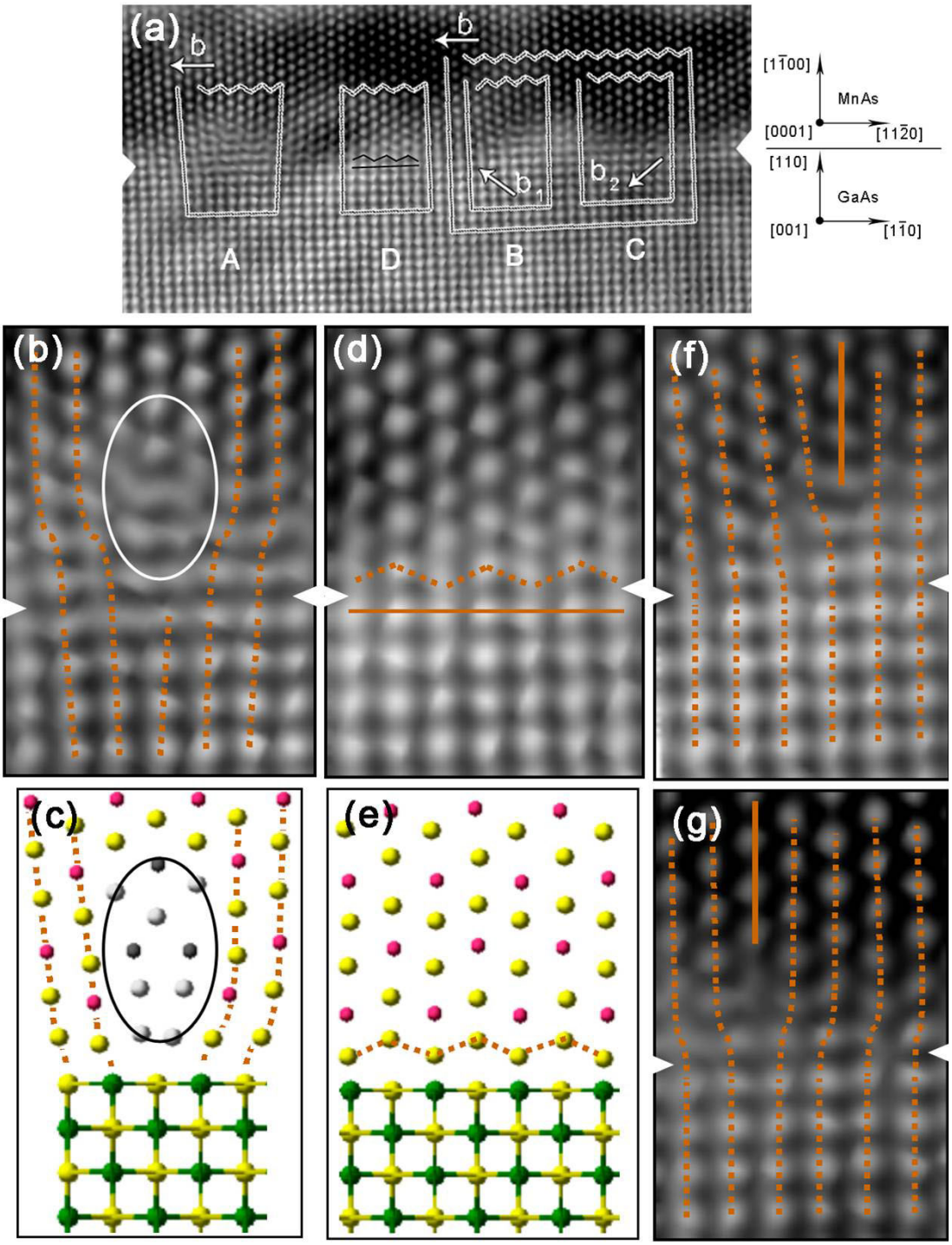

Figure 6.7: (a) The Fourier filtered and magnified image of the area in the rectangle in Figure 6.6(a). Note that a perfect edge dislocation and two partial dislocations are identified by Burgers circuits. The interface can be distinguished clearly as indicated by a straight line (GaAs) and a zigzag line (MnAs). Magnifications of the region around (b) the core of a perfect dislocation and (d) lattice matched area, and their corresponding atomic configurations in (c) and (e), respectively. Note that the dislocation core is indicated by the ellipse. Magnifications of the partial dislocations are shown in (f) and (g) for comparison.

rection lying parallel the incident electron beam and the edge component of their Burgers vector in the imaging plane. Both conditions are satisfied for the misfit dislocations in the HRTEM micrograph shown in Figure 6.7(a) as demonstrated in the following.

As demonstrated in the next subchapter, the image is a "white-atom" micrograph with the bright spot representing atomic positions. The image reveals a semi-coherent interface, along which lattice-matched areas (marked as **D**) are separated by different dislocated areas (marked by **A**, **B** and **C**). Due to the difference in crystal symmetry between film and substrate, the interface position is clearly indicated in area **D** by the transition from a zigzag line in MnAs to a straight line of the bright dots in GaAs. Considering the fact that no interface step is present, such interface position can be extrapolated to the whole interface in Figure 6.7(a).

A Burgers circuit is drawn around the center of dislocation core that is located at region **A**. In that area, a strong lattice plane bending is observed associated with a heavily localized strain field and a high strain energy. The dislocation core structure can be seen more clearly in the magnified image shown in Figure 6.7(b), with the coherent area shown in Figure 6.7(d) for comparison. On the basis of the atomic configuration of the MnAs/GaAs (110) interface (c.f Chapter 6.3.3), simple atomic models of the dislocated area (cf. Figure 6.7(c)) and the coherent area (cf. Figure 6.7(e)) can be further extracted from Figures 6.7(b) and 6.7(d), respectively, by correlating the bright dots to the corresponding atoms. However, due to the strong distortion of the interference pattern in the core area of the dislocation (indicated by the ellipse), the HRTEM image of the core is not directly interpretable. Other than that, the dislocation is characterized by two extra $\{22\bar{4}0\}_{MnAs}$ half planes. No visible distortion is observed in the MnAs lattice beyond 6 monolayer away from the interface, indicating a very localized strain field associated with the dislocation as a result of the dislocation array. The dislocation core is delocalized along the $[1\bar{1}00]_{MnAs}$ direction and compact with only minimal spreading along the perpendicular $[11\bar{2}0]_{MnAs}$ direction. Furthermore, it is not located exactly at the interface, but shifted 1–3 monolayers away into the MnAs side. Since most of the bending around the dislocation core is restricted to the MnAs lattice, it is reasonable to describe this interfacial misfit dislocation regarding only to the MnAs lattice. The closure failure in **A** as compared to the closed Burgers circuit in **D** reveals Burgers vector component in the imaging plane of $\mathbf{b} = \mathbf{a}/3[11\bar{2}0]_{MnAs}$. Since $\mathbf{a}/3[11\bar{2}0]_{MnAs}$ is a translational lattice vector of the hexagonal structure, the present dislocation is a perfect edge one, which has both its line and Burgers vector parallel to the interface, and therefore, is most efficient for strain relaxation.

Two additional dislocations, which are located about 6–7$\{22\bar{4}0\}_{MnAs}$ planes away to each other at the interface, are observed in regions **B** and **C**, with their corresponding magnified images shown in Figures 6.7(f) and 6.7(g), respectively. In both cases, the dislocation is characterized by one extra $\{22\bar{4}0\}_{MnAs}$ half plane. The lattice plane bending around each dislocation core is much weaker than that observed around the core of the perfect edge dislocation. Burgers circuit analysis reveals that the Burgers vector component in the imaging plane for the dislocations in regions **B** and **C** are $\mathbf{b}_1 = \mathbf{a}/3[2\bar{1}\bar{1}0]_{MnAs}$ and $\mathbf{b}_2 = \mathbf{a}/3[\bar{1}2\bar{1}0]_{MnAs}$, respectively, both of which have a strain-relieving component of $\mathbf{a}/6[11\bar{2}0]_{MnAs}$. They are not translation vectors of the MnAs lattice, and their sum is equal to the Burgers vector of the edge type dislocation. These dislocations are therefore recognized as partial dislocations. The formation mechanism of partial dislocations still remains open to us. They are not introduced by the conventional dissociation-glide process since $(1\bar{1}00)_{MnAs}$ plane is not the glide plane for these partials and, furthermore,

there is no driving force for the glide process due to the complete relaxation of lattice misfit stress. Climb process is also unlikely because the growth temperature of 250°C is too low for the activation of climb. One possible explanation is that the dissociation is an energy-driven process, which is activated by the residual stress from the sample preparation or forces related to the thin foil effect, e.g. image force [96].

Similar as the perfect dislocation, it is found from the HRTEM image of partial dislocations in Figures 6.7(f) and 6.7(g) that the cores are located 2-3 monolayers away from the interface in MnAs side. Such a situation is called "a stand-off position of misfit dislocations" [94]. They have been observed before in the diffusion-bonded metal/ceramic system [92]. Located in the elastically softer medium, the dislocations are repelled by the image force from the interface, however attracted by the coherence force induced by the lattice misfit between two crystals. The equilibrium position of the dislocation is known as "stand-off" position when the net force on the dislocation is zero [78,93,94]. Considering the fact that there is a large difference in the shear modulus E of the GaAs and MnAs along the $[11\bar{2}0]_{MnAs}||[1\bar{1}0]_{GaAs}$ direction ($\mu_{GaAs} \sim 33$ GPa; $\mu_{MnAs} \sim 18$ GPa [95]), the core of the dislocations would accordingly lie at some distance away from the interface in the MnAs lattice. On the other hand, it has been demonstrated that a wetting layer is deposited on the GaAs substrate prior to the formation of the islands with built-in dislocations during the epitaxial growth of MnAs. Since there is no driving force for these built-in dislocations to glide, they would rather stay where they are formed, i.e. 2–3 monolayers away from the interface.

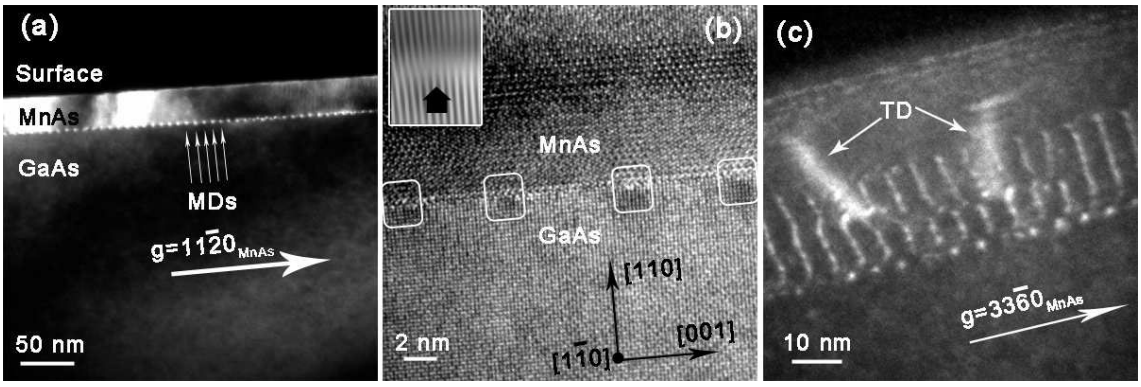

Figure 6.8: (a) DF micrograph of 30 nm MnAs film on GaAs (110) with $\mathbf{g} = 11\bar{2}0_{MnAs}$. Notice the array of misfit dislocations (MDs) along the interface (arrowed). (b) HRTEM image of the interface. Fourier filtered image is shown as inset to better illustrate the interfacial dislocations. (c) Weak-beam DF image recorded by tilting the specimen about 12° with $\mathbf{g} = 33\bar{6}0_{MnAs}$. All images are taken along the $[0001]_{MnAs}||[001]_{GaAs}$ projection (TD: threading dislocation).

A compact film has formed for the sample with nominally 30 nm MnAs. Figure 6.8(a) illustrates a $\mathbf{g} = 11\bar{2}0_{MnAs}$ dark-field (DF) image of the MnAs film taken close to the $[0001]_{MnAs}||[001]_{GaAs}$ projection. An array of contrast features along the interface is observed with a mean distance of $D = 5.3 \pm 0.2$ nm between each other. The HRTEM micrograph in Figure 6.8(b) indicates that each feature corresponds to a perfect edge dislocation. The interface microstructure is further investigated employing weak-beam (WB) DF TEM by tilting the cross-sectional specimen around 12° away out of the $[0001]_{MnAs}$ zone axis around the $[11\bar{2}0]_{MnAs}$ direction. Figure 6.8(c) shows a regular array of sharp bright lines lying along the interface corresponding to the interfacial dislocations. The

lines are misregistered in the area bounded by threading dislocations. Such misregistration is formed during the coalescence of the relaxed MnAs islands. The positions of the misfit dislocations in the coalesced islands are not necessarily in phase with each other, and consequently, threading dislocations are easy to be generated at these misregistered locations along the boundary of the islands. Furthermore, comparing with the interfacial dislocations, the contrast related to the threading dislocations in Figure 6.8(c) is much broader. This represents that the interfacial dislocation has a much more localized strain field than that of the threading one.

Diffraction patterns recorded from a structured interface carry the information on periodicities in the interface. A row of reflections corresponding to the interfacial periodicities will be present elongated along the normal of the interface in the reciprocal space, and finally lead to appearance of the fine structures around the matrix reflection in the SAED pattern. Analysis of such fine structures has been proved to be a useful method to study the grain boundary in polycrystalline metal and semiconductors [53, 97, 98]. Figure 6.9(a) shows the SAED pattern of the sample with 30 nm MnAs along the $[0001]_{MnAs}||[001]_{GaAs}$ projection. By tilting the specimen slightly off the zone axis, we observe the emergence of faint lines elongated along the $[1\bar{1}00]_{MnAs}$ direction around the $(11\bar{2}0)_{MnAs}$ spot as highlighted in Figure 6.9(b). The appearance of these lines is attributed to the extra periodicity at the interface induced by the misfit dislocations. When the interface is viewed edge-on under current imaging condition, the relrods associated with the dislocation array are observed as streaks, since the Ewald sphere cuts along them [cf. Figure 6.9(d)]. The length of the relrods reveals how far the strain field of the dislocation array extends out into two adjacent crystals, or in other words, the "width" of the interface. With the knowledge that the length of the relrod can be roughly estimated by $1/t$ [53], where t is the width of the interface, we obtain a value of around 3.4 nm. Such "sharp" interface suggests that, the strain field is confined within a thickness of 3.4 nm away from the interface, and beyond that, the MnAs is almost elastic distortion free. This is the consequence of the compensation of the strain fields from the respective dislocations in a periodic array. Theoretical calculation of the displacement field due to the periodic dislocations has been performed with respect to the similar MnAs/GaAs (001) heterostructure, under the assumption of elastic isotropy [80]. The estimated interface thickness of 1.6 nm corresponds well to our result. A more accurate simulation needs to consider the anisotropic elastic behaviors [99], however is beyond the scope of the current research.

To set a **g**–3**g** image condition, the specimen is tilted around 12° about $[11\bar{2}0]_{MnAs}$ direction together with the relrods in the reciprocal space. As schematically illustrated in Figure 6.9(e), the relrods corresponding to the interfacial dislocations are no longer tangential to the Ewald sphere, and accordingly, appear as spots in the SAED pattern in Figure 6.9(c). They have the same spacing as the streaks in Figure 6.9(b). The spacing of these reflections (**p**) is half of the distance between the $(11\bar{2}0)_{MnAs}$ and $(2\bar{2}0)_{GaAs}$ spots, which corresponds, in real space, to the periodicity of the envisaged structure along the interface, or in terms of misfit dislocations, the mean separation D of the dislocations with Burger vector $\mathbf{b} = \mathbf{a}/3[11\bar{2}0]_{MnAs}$. The measured value of 5.1±0.1 nm agrees well with the mean distance between dislocations that is roughly estimated from the WB-DF image. Estimation of the strain relieved by these dislocations according to (5.3) yields to -7.35%, implying that there is almost no residual strain along the $[11\bar{2}0]_{MnAs}$ direction, which is in accordance with the fact that the film is formed by completely relaxed islands.

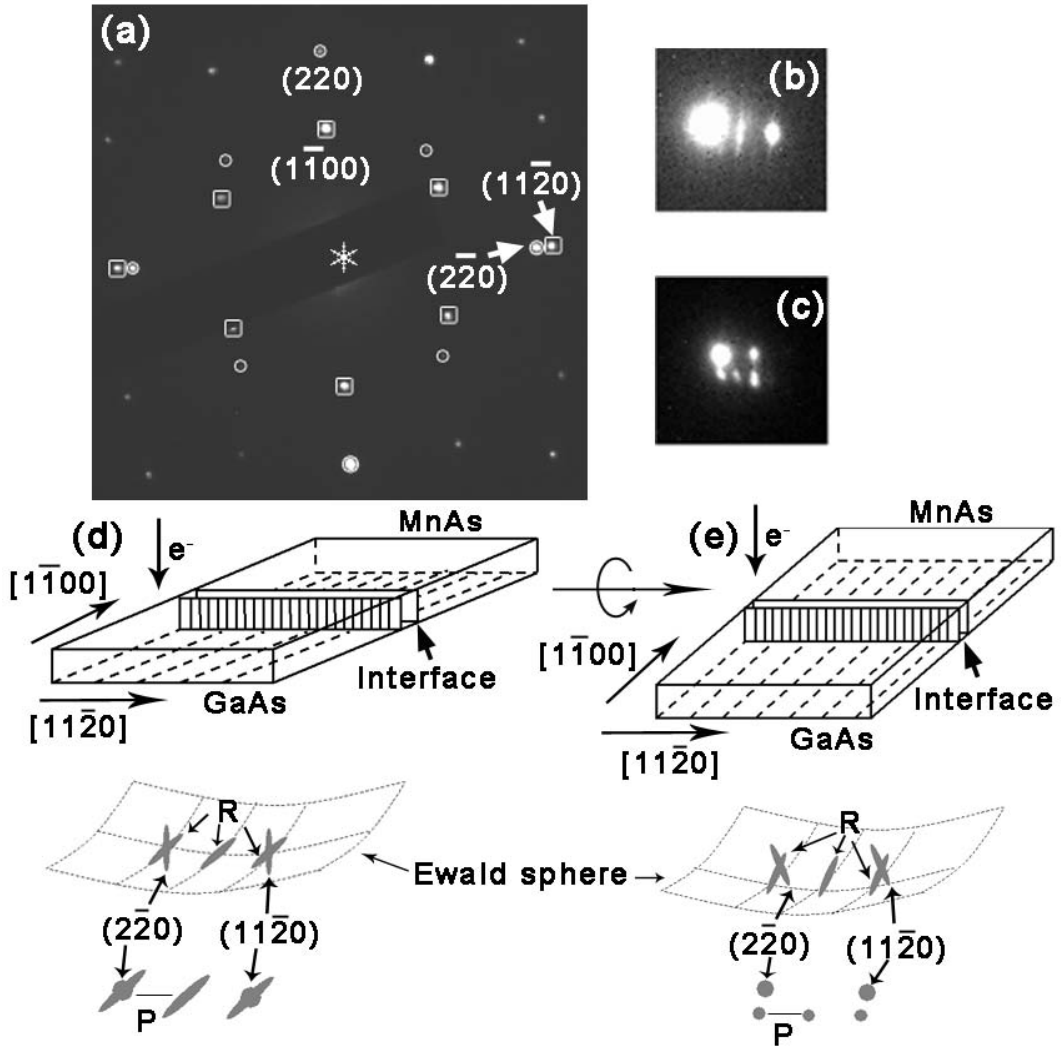

Figure 6.9: (a) SAED pattern of the sample with 30 nm MnAs along the $[0001]_{MnAs}||[001]_{GaAs}$ direction. Magnification of the region around $(11\bar{2}0)_{MnAs}$ reflection after tilting the specimen (b) slightly off the pole and (c) into a g-3g weak-beam condition. The geometry of the heterosystem and the reciprocal lattice in the vicinity of $(11\bar{2}0)_{MnAs}$ reflection in (b) and (c) is also shown in (d) and (e), respectively. The dotted lines in the GaAs and MnAs denote $(2\bar{2}0)_{GaAs}$ and $(11\bar{2}0)_{MnAs}$ planes, respectively. R: the relrods associated with the dislocation array at the interface.

6.3.3 Atomic configuration of the interface

The Mn-As bond has a large ionic contribution in NiAs-type MnAs crystals [100]. When MnAs is combined with covalently bonded GaAs, the resultant bond configuration at the interface is unclear and a key issue for the spin injection [101]. On the other hand, HRTEM is a powerful method to study the atomic structure of interfaces. This technique, with assistance of contrast simulations, has been successfully applied to ceramic-ceramic (e.g. [102]), metal-metal oxide (e.g. [92, 103]), and metal-semiconductor interfaces (e.g. [104]). In the present subchapter, we will study the atomic configuration of the MnAs/GaAs interface by semi-quantitative HRTEM.

As discussed previously, the strain associated with the -7.5% lattice mismatch along

the $[11\bar{2}0]_{MnAs}||[1\bar{1}0]_{GaAs}$ direction is almost completely relaxed by the formation of a periodic array of misfit dislocations. Along such a semi-coherent interface, areas of preserved coherency are separated by localized interfacial misfit dislocations as evidenced in Figure 6.7(a). In the following, we will only focus on the coherent part of the interface, which is described by a lattice plane matching across the boundary. The coherent parts offer the opportunity to quantitatively compare the HRTEM images with contrast simulations based on a simple rigid lattice model.

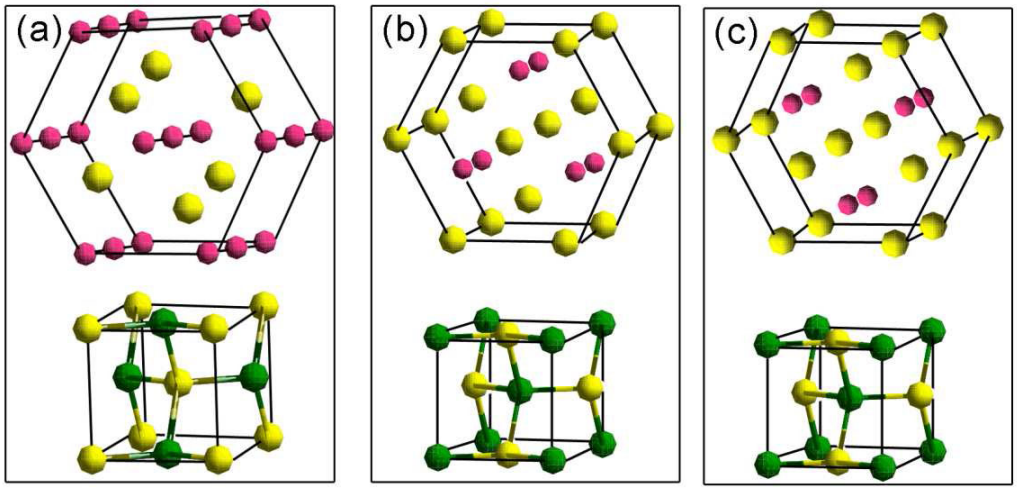

Figure 6.10: Schematic diagrams of the three different MnAs/GaAs (110) interface configurations. The Mn, As and Ga atoms are indicated by red, yellow and green spheres, respectively.

In order to construct a reasonable atomic model of the interface, three characteristic properties have to be addressed:

- The relative orientation of both crystal lattices along the interfacial plane;
- The interface distance;
- The respective atom occupancy of the terminating lattice planes at the interface.

The GaAs (110) planes contain an equal number of Ga and As atoms. Therefore, only one structural configuration is possible for the GaAs substrate side of the interface. Due to the NiAs lattice type of MnAs and the epitaxial orientation relationship with respect to GaAs (110) surface, there are three potential interfacial configurations, which are illustrated schematically in Figure 6.10 (neglecting the exact in-plane positions). These configurations manly differentiate in the terminating atoms of the first and second monolayers of MnAs, which consist of Mn or As atoms, respectively. In the following, we will try to identify the terminating MnAs layers by comparing HRTEM image with simulations.

Figure 6.11(a) illustrates a cross-sectional HRTEM micrograph of the heterosystem at the interface along the $[0001]_{MnAs}||[001]_{GaAs}$ direction. The experimental image has been Fourier filtered in order to reduce the noise and improve the interference pattern [Figure 6.11(b)]. Due to the difference in crystal symmetry between film and substrate, the interface is clearly recognized, which appears atomically abrupt without any implication of chemical reactions. As already mentioned, coherent interface parts are separated by misfit dislocations, which are characterized in the HRTEM image by a local lattice plane

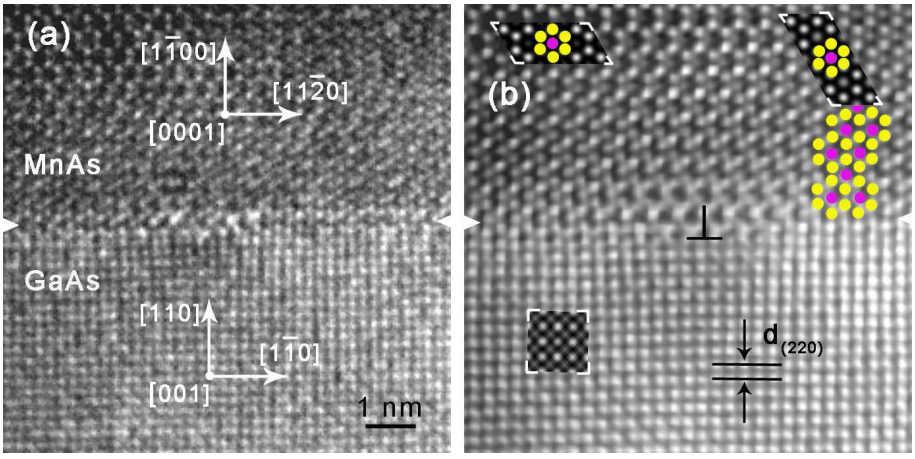

Figure 6.11: (a) Cross-sectional HRTEM image of the MnAs/GaAs (110) interface taken along the $[0001]_{MnAs}||[001]_{GaAs}$ direction and its Fourier-filtered version (b). The atomic model of MnAs and its simulated patterns are overlaid for comparison as insets. Calculated contrast for GaAs is also shown in the inset.

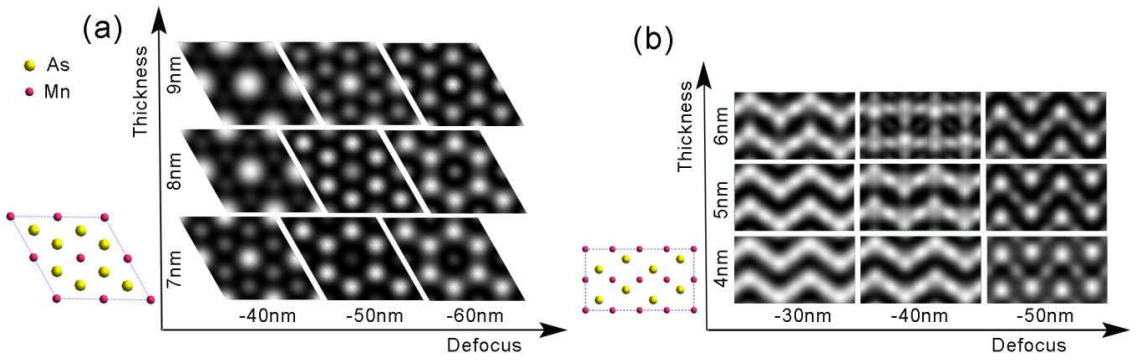

Figure 6.12: Thickness-defocus maps of the HRTEM contrast simulations for MnAs along the (a) [0001] and (b) $[11\bar{2}0]$ zone axis.

bending. In the present micrograph, this plane bending leads to a strong distortion of the MnAs interference pattern. On the contrary, the homogeneous contrast inside the MnAs layer represents a simple hexagonal interference pattern that locally changes into a pattern of hexagons containing a centered weak spot. The variation of the pattern from area to area indicates that the TEM specimen is not uniform in thickness.

The quantitative analysis of the HRTEM contrast, which is needed to determine the atom positions, requires a careful comparison between experimental and simulated images. In the following, we first simulate the thickness-defocus maps for both, the MnAs and GaAs crystal lattice, and then examine if the simulated patterns, which resemble the experimental contrasts, have realistic thickness and defocus values and if these values are nearly equal for both the MnAs and GaAs. After a reliable assignment is acquired, we can finally correlate the experimental interference pattern with the atomic models. The Figures 6.12(a) and 6.13(a) reveal simulated thickness-defocus maps of MnAs and GaAs along the [0001] and [001] direction, respectively, in the thickness range between 7 and 9 nm, and the defocus range between -40 and -60 nm. In all cases, these calculations are actually performed over a larger range of thicknesses (2 nm to 15 nm) and defocus values (-20 nm to -100 nm). However, only the applicable range of the thickness-defocus map

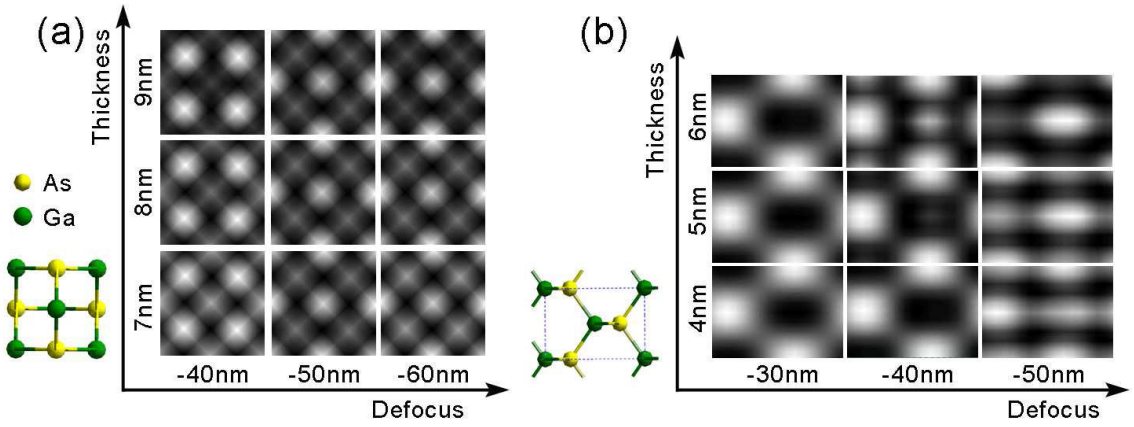

Figure 6.13: Thickness-defocus maps of the HRTEM contrast simulations for GaAs along the (a) [001] and (b) $[1\bar{1}0]$ zone axis.

around Scherzer defocus is presented since the rest are irrelevant to the understanding of the experimental results. On the basis of this map, it is figured out that the experimentally detected hexagonal pattern [cf. Figure 6.11(b)] is in best accordance with the simulated lattice image of MnAs for a foil thickness of 7 nm and a defocus value of -50 nm, while the interference pattern of hexagons with a weak, centered spot agrees perfectly with the MnAs contrast at the same defocus but at the marginally different thickness of 8 nm. Moreover, the squared array of GaAs pattern is also well simulated using the same imaging conditions (defocus value of -50 nm and thickness of 8 nm). Based on this interpretation of the contrast in MnAs and GaAs, we conclude that all the bright spots in the HRTEM image correspond to atom positions. This result consequently indicates an "atom-on-atom" relationship cross the coherent interface along this projection. Furthermore, the shortest atom spacing of the Mn sublattice is larger than that of the As sublattice in the [0001] projection view of MnAs [cf. Figure 6.12(a)]. It is therefore possible to correlate the interference pattern with the atomic model as shown in Figure 6.11(b). Positions of Mn and As atoms are superimposed upon the simulated contrast and extrapolated by repeating this pattern up to the interface. Obviously, the MnAs crystal at the interface is terminated by two monolayers of As atoms, pointing to the applicability of the atomic interface model presented in Figure 6.10(b).

Beyond the atom termination, the interface distance between the two crystals can be additionally measured from the coherent part at the interface, e.g. region **D** in Figure 6.7(a). Figure 6.14 illustrates a noise-reduced magnified micrograph of region **D**, where the interface position is clearly indicated by the transition from a zigzag line in MnAs to a straight line of the bright dots in GaAs. For both MnAs and GaAs materials, the simulated interference pattern at a thickness of 9 nm and a defocus of -60 nm corresponds well with the experimental image in Figure 6.14, respectively. The result of the contrast simulations implies that the bright dots in both crystals again correspond to the atom positions. Therefore, the interplanar spacing and the interface distance can be directly measured by an intensity profile generated from an intensity line scan of the TEM image (line scans were integrated over a width of 5 nm). With the bulk value of GaAs (220) interplanar spacing as an internal standard ($d_1 = 0.199$ nm), the MnAs interplanar spacing is obtained being 0.212 ± 0.005 nm that agrees well with the theoretical value of 0.213 nm for bulk MnAs. Furthermore, an interface separation of 0.176 ± 0.005 nm is acquired, which is smaller than the corresponding lattice plane distances in both MnAs and GaAs,

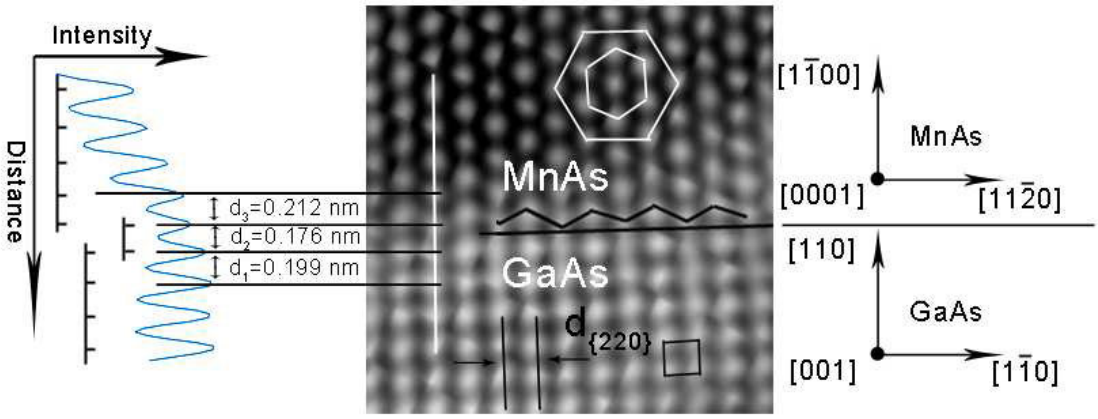

Figure 6.14: Noise-reduced $[0001]_{MnAs}||[001]_{GaAs}$ cross-sectional HRTEM image of a coherent area between two dislocations. Note that the interface can be distinguished clearly as indicated by a straight line (GaAs) and a zigzag line (MnAs). An accurate measurement of the lattice plane spacing at the interface region is obtained by a scan along the white line in the image.

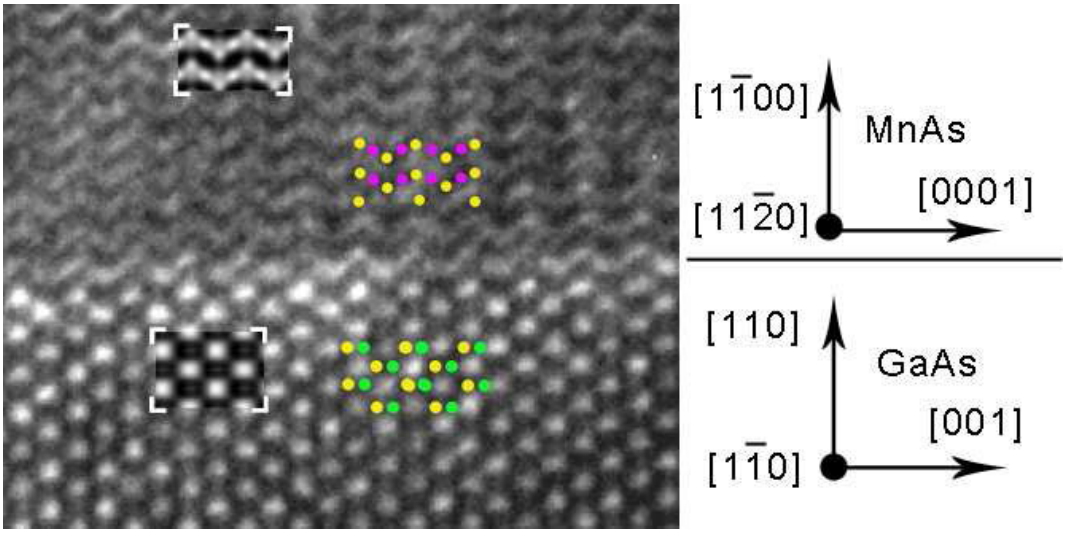

Figure 6.15: Cross-sectional HRTEM image of the MnAs/GaAs (110) interface along the $[11\bar{2}0]_{MnAs}||[1\bar{1}0]_{GaAs}$ direction. The atomic models and simulated patterns are superimposed for comparison as insets.

indicating a good adhesion of the interface.

Figure 6.15 reveals the cross-sectional HRTEM micrograph of the interface along the $[11\bar{2}0]_{MnAs}||[1\bar{1}0]_{GaAs}$ projection. The corresponding thickness-defocus maps of MnAs and GaAs are shown in Figure 6.12(b) and Figure 6.13(b) respectively, in the relevant range of thicknesses between 4 and 6 nm, and defocus values between -30 and -50 nm. Comparing the simulations with the experimental image, the HRTEM contrast of the MnAs lattice imaged in the $[11\bar{2}0]$ direction is wavy-like with a period corresponding to the hexagonal lattice constant **c**, in agreement with the calculated contrast pattern of MnAs for a thickness of 5 nm and a defocus of -40 nm. The interference pattern in GaAs is also well reproduced under the same imaging condition. Therefore, it is figured out that the bright dots in the micrograph represent tunnel positions. By correlating the

contrast with the positions of Mn, As and Ga [cf. Figure 6.15], it becomes apparent that the atoms in the first layer of MnAs are located directly on top of Ga-As dimers.

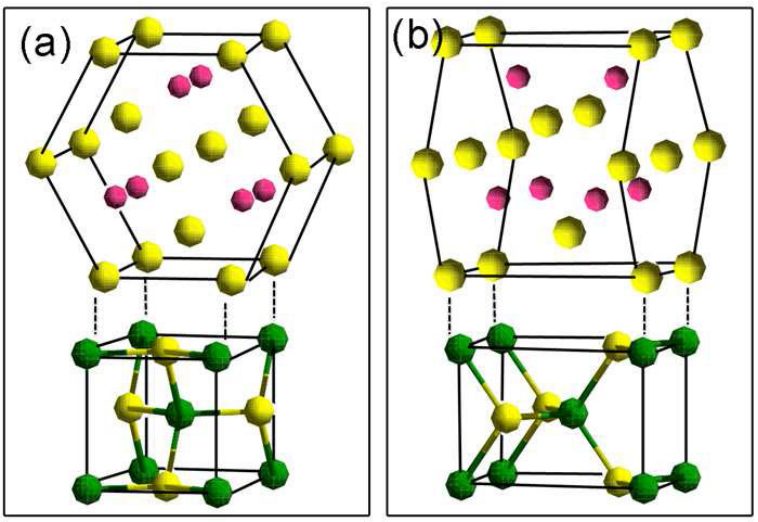

Figure 6.16: Interfacial atomic model of the MnAs/GaAs (110) interface viewed along (a) [0001] and (b) $[11\bar{2}0]$ direction.

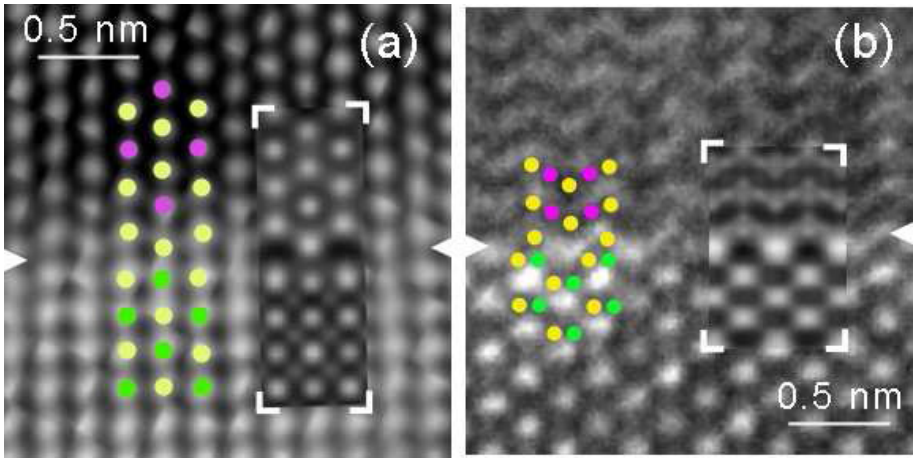

Figure 6.17: Noise-reduced cross-sectional HRTEM image of a coherent area of the MnAs/GaAs (110) interface taken along the (a) $[0001]_{MnAs}||[001]_{GaAs}$ and (b) $[11\bar{2}0]_{MnAs}||[1\bar{1}0]_{GaAs}$ direction. Interface configuration model and its simulated contrast are superimposed for comparison.

Based on all given results, we elaborate a rigid atomic model of the MnAs/GaAs (110) interface as shown in Figure 6.16. The MnAs lattice at the interface is terminated by two monolayers of As atoms similar to the configuration presented in Figure 6.10(b). The interface distance in the model is set to be 0.176 nm according to the experimentally determined value. The As atoms on the last layer of MnAs are placed on top of the Ga atoms in the GaAs (110) planes. Figure 6.17(a) and 6.17(b) illustrate HRTEM micrographs and their corresponding simulations of a coherent interface region along the $[0001]_{MnAs}||[001]_{GaAs}$ direction and $[11\bar{2}0]_{MnAs}||[1\bar{1}0]_{GaAs}$ direction, respectively. The good agreement between experimental and simulated contrast at the interface in both projections, i.e. the sequence

of bright and dark spots in Figure 6.17(a) and the large bright spots with bridges in between in Figure 6.17(b), respectively, prove the suitability of the interface model.

In conclusion, with the assistance of image simulation, we successfully identify the atomic configuration of the terminating MnAs layer at the interface and the relative atom locations between MnAs and GaAs. The atomic configuration of the MnAs/GaAs interface is characterized by an "atom-on-atom" orientation relationship. Therefore, the bond length at the interface between the As from MnAs and Ga from GaAs is equal to the interface separation of about 0.176 nm. Comparing this interfacial bond length of Ga-As to the bond length of the covalently bonded Ga-As in cubic GaAs lattice, which is about 0.245 nm, we conclude that the interface is characterized by a special bonding type with ionic fraction. An interfacial atomic configuration is proposed by applying the interface separation acquired from the HRTEM image. The good agreement between the simulations and experimental images supports the validity of the model. We anticipate that our structural results will advance theoretical studies on the electron and spin density distribution of the interface between ferromagnetic MnAs and GaAs in order to achieve a deeper understanding of the mechanisms affecting the spin injection.

6.3.4 Overgrowth of GaAs on MnAs

The application of ferromagnetic/semiconductor materials requires artificial nanostructures, such as multilayer structures, to realize the novel functionalities. For instance, a typical giant magnetoresistance (GMR) device today consists of a trilayer structure with a pinned magnetic layer and one in which the magnetization is free to rotate [105]. Nevertheless, the epitaxial growth of the multilayer structure is far more difficult. The quality of the nonmetallic spacer layers is problematic and difficult to control. Here 6 nm GaAs is overgrown on 30 nm MnAs/GaAs (110) as the first step to study the ferromagnetic/semiconductor multilayer structure. The epitaxial orientation relationship between the overgrown GaAs and MnAs is identical as the previous MnAs/GaAs case. Due to the MnAs relaxation, consequently, the GaAs layer is free of strain along the $[0001]_{MnAs}||[001]_{GaAs}$ direction (coherent interface) and 7.5% mismatched along the perpendicular $[11\bar{2}0]_{MnAs}||[1\bar{1}0]_{GaAs}$ direction.

It is known from Chapter 6.3.1 that a wetting layer exists during the epitaxy of MnAs on GaAs (110), in agreement to equation (6.1). When GaAs is inversely grown onto MnAs, the surface free energy of the overlayer has to be "exchanged" with that of the substrate, while the interfacial energy and strain energy remain identical. As we know: $\gamma_{MnAs(1\bar{1}00)} < \gamma_{GaAs(110)}$, the following equation is fulfilled:

$$\gamma_{GaAs} + \gamma_i + \gamma_\varepsilon \geq \gamma_{MnAs} \tag{6.2}$$

Therefore, a 3D island growth mode is expected for the overgrowth of GaAs on MnAs, which is evidenced by the in-situ RHEED investigations. The patterns in Figure 6.18(a) and 6.18(b) are taken right after the accomplishment of 30 nm thick MnAs, with the electron beam along the $[11\bar{2}0]$ and [0001] direction of MnAs $(1\bar{1}00)$ surface, respectively. The surface reconstruction is identified as (1×2) structure. The sharp streaky patterns represent a well-defined atomically smooth surface of the MnAs film. Figure 6.18(c) and 6.18(d) are taken 30 seconds after the beginning of the overgrowth of GaAs. The spotty transmission-like features in the RHEED patterns represent that the epitaxy of GaAs proceeds via 3D islands.

The surface topography of 30 nm thick MnAs with and without the overgrowth of

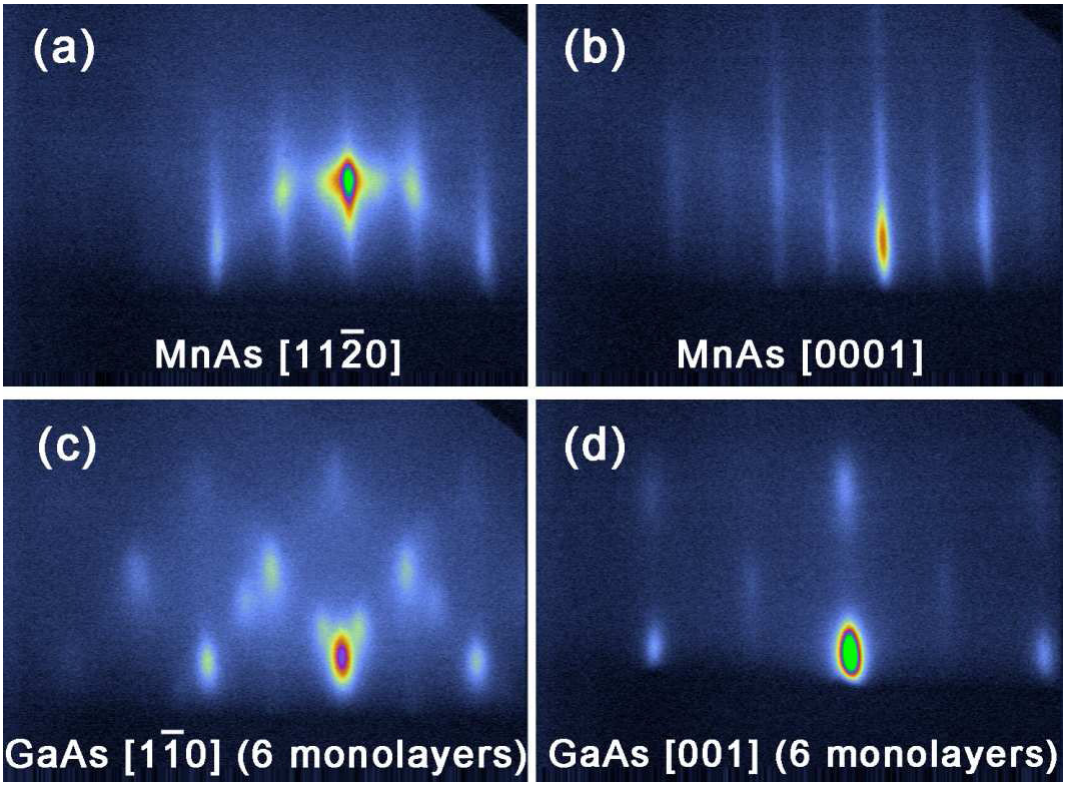

Figure 6.18: RHEED patterns taken in the (a) $[11\bar{2}0]_{MnAs}$ and (b) $[0001]_{MnAs}$ azimuth before the overgrowth of GaAs. RHEED patterns taken in the (c) $[1\bar{1}0]_{GaAs}$ and (d) $[001]_{GaAs}$ azimuth with 6 monolayers of GaAs deposited on MnAs.

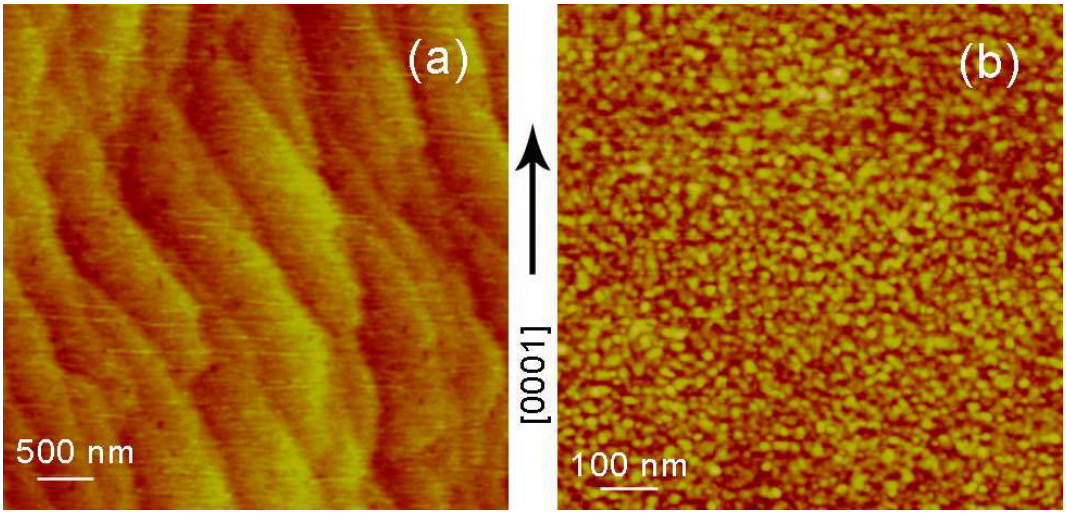

Figure 6.19: AFM images of (a) 30 nm MnAs on GaAs (110) and (b) 6 nm GaAs overgrown on MnAs.

6 nm GaAs imaged by atomic force microscope (AFM) is shown in Figure 6.19(b) and 6.19(a), respectively. An array of monolayer steps is observed for the sample with only 30 nm MnAs grown, indicating that the sample has a well-defined atomic smooth surface. After the growth of nominally 6 nm thick GaAs, a very rough surface with 3D GaAs islands of irregular shape has developed as can be seen in Figure 6.19(b), which evidences

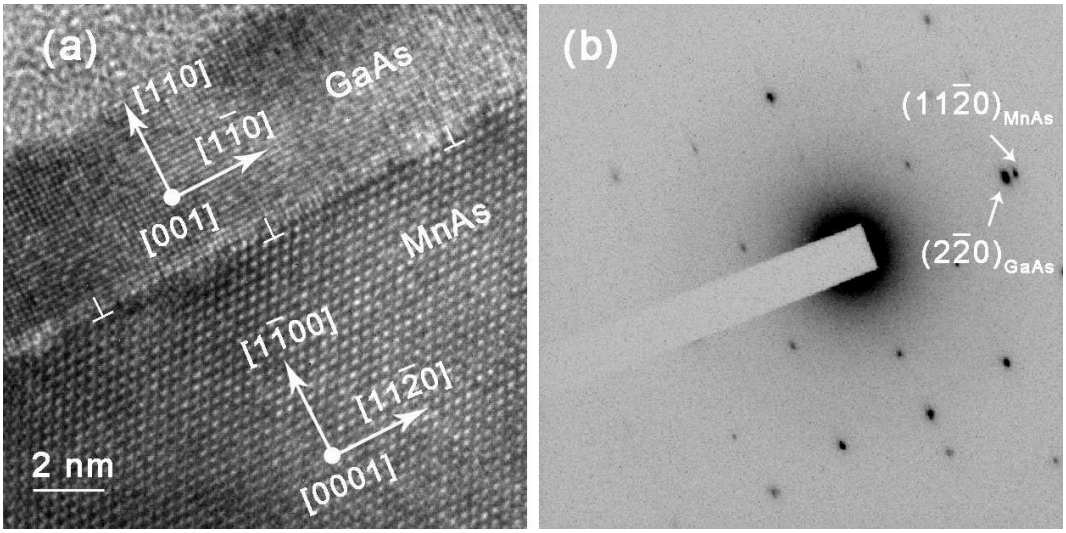

Figure 6.20: (a) Cross-sectional HRTEM image of the GaAs/MnAs interface along the $[0001]_{MnAs}||[001]_{GaAs}$ direction with its corresponding SAED pattern (b).

the presence of GaAs islands.

Figure 6.20(a) illustrates a HRTEM cross-sectional micrograph of the interface along the $[0001]_{MnAs}||[001]_{GaAs}$ direction. The heterostructure is characterized by a rough surface and a clear chemically sharp boundary with monolayer steps present. An array of dislocations is formed at the interface for the relaxation of the strain related to the lattice misfit. Similar as the MnAs/GaAs interface, the lattice plane bending around the dislocation core is neglectable in GaAs side, indicating the dislocation can be described only with respect to the MnAs lattice. However, since the present contrast in the MnAs lattice only reflects the Mn atom column positions, whose shortest atom spacing is about twice as large as that of the As sublattice, and the strain field is quite localized, the distortion in MnAs lattices not as obvious as the previous case shown in Figure 6.7(a). Burgers vector analysis indicates that the dislocations are perfect edge dislocations with $\mathbf{b} = \mathbf{a}/3[11\bar{2}0]$. Figure 6.20(b) shows the SAED pattern of the GaAs/MnAs interface. With the lattice parameter of MnAs as an internal standard, the lattice constant of GaAs is calculated to be very close to its bulk value, implying that the mismatch strain along this direction is almost completely relieved by the formation of misfit dislocations.

From the perpendicular $[11\bar{2}0]_{MnAs}||[1\bar{1}0]_{GaAs}$ projection as shown in Figure 6.21(a), the lattice image of the interface confirms the existence of 3D islands, which are characterized by {111} planes as their facets. A large amount of planar defects (cf. Figure 6.21(b)), including stacking faults and twins, are present in the islands. These two-dimensional defects are commonly attributed to the stresses caused by the lattice mismatch, or by the mismatch of thermal expansion between film and substrate. Such stresses lead to nucleation of misfit dislocations for the strain relaxation, which would split into partials and glide apart leaving stacking faults in between. In our case, however, the occurrence of such a high density of planar defects cannot be explained by such classic mechanism, since the overgrown GaAs is strain free along the [001] direction. Interface steps and surface impurities are also considered as locations of high stress, where dislocations and planar defects are easy to generate. As illustrated in Figure 6.22, the stacking fault in the MnAs layer introduces a step on its surface, where planar defects are originated. Considering that the surface of MnAs is atomically smooth, the surface step is definitely not the

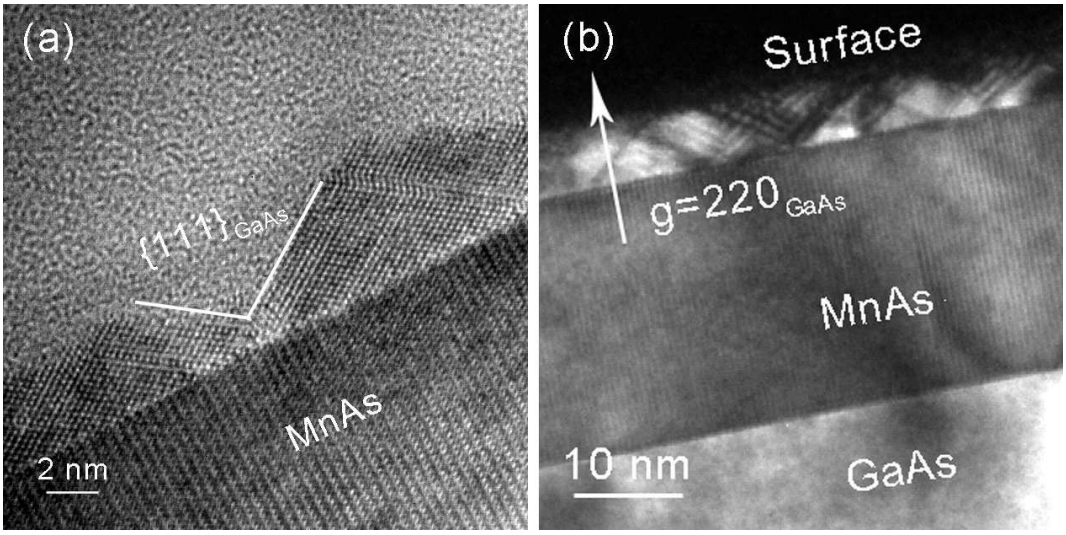

Figure 6.21: Cross-sectional HRTEM image (a) and DF image (b) of the interface of 6 nm GaAs on MnAs/GaAs (110) with electron beam parallel to the $[11\bar{2}0]_{MnAs}||[1\bar{1}0]_{GaAs}$ direction. Notice the island in (a) has {111} facets. The bright contrast in the overgrown GaAs film in (b) represents planar defects.

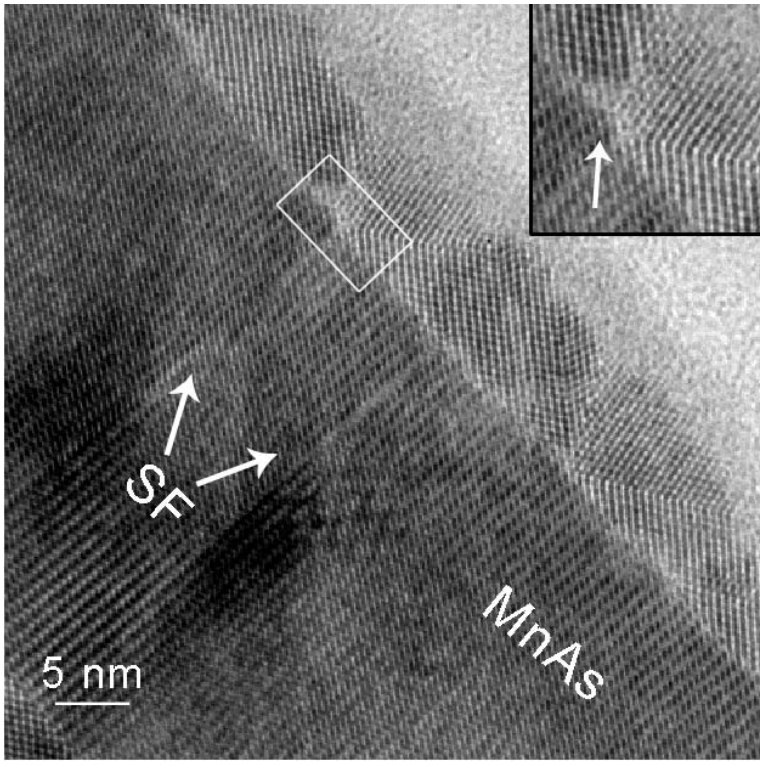

Figure 6.22: Cross-sectional HRTEM of the GaAs/MnAs interface along the $[11\bar{2}0]_{MnAs}||[1\bar{1}0]_{GaAs}$ zone axis. Note an interface step is shown in the inset.

main reason for such a large amount of planar defects.

In case of 3D growth, the nuclei are faceted along the low-energy planes, i.e., the close-packed {111} planes for zinc-blende structure. Further growth of the islands requires the deposition of atoms on these facets. However, it is possible that the atoms stop at incorrect sites forming a small fraction of faulted layer, since the energy of the resulting stacking fault is quite small [109]. These misdeposited layers either lead to the formation of stacking faults (intrinsic and extrinsic), or nanotwins, as depicted in Chapter 2.2.2. Moreover, the growth temperature must be high enough that the adatoms have sufficient mobility to crystallize into a thermodynamic equilibrium crystal structure. Since the current substrate temperature for the GaAs growth is as low as 250°C (comparing with the normal applied 560°C), the weak adatom's mobility would lead to a high density of nucleus and, accordingly, a large amount of {111} facts. As a result, the fraction of misdeposited atoms is expected to be even higher and it is therefore not surprising to observe so many planar defects.

Chapter 7

Microstructure of intermetallic CoAl on GaAs

In this chapter, we present the microstructural analysis of epitaxially grown intermetallic CoAl alloys on GaAs (110) and (001) substrates. A coexistence of B2 phase and its disordered version bcc phase is observed in the CoAl film. The disordering is induced partially by the epitaxial strain and partially by the diffusion of point defects, including vacancies and Co atoms. The strain-induced disordering diminishes with the initiation of the plastic relaxation, which is realized by the formation of a nearly periodic array of interfacial precipitates. The diffusion-induced disordering is less intense at lower growth temperature, due to the lower diffusivity and smaller concentrations of vacancies and Co antisite defects. In addition, misoriented domains are formed in (110) oriented CoAl. They are originated from the interface roughness.

7.1 Introduction

Intermetallic alloys, including FeAl, CoAl and NiAl, are of great importance since these materials have not only good strength-to-weight ratio but also excellent corrosion and oxidation resistance. These properties make them promising candidates for high-temperature and soft magnetic materials [110]. In combination with semiconductor materials, they open potentialities as spin injectors or mirrors applied in novel optoelectronic or spintronic devices. Furthermore, buried intermetallic films between two III-V compound semiconductors may possibly be used in resonant tunneling diodes and metal-base transistors [111]. Among these intermetallic alloys, CoAl is especially attractive for epitaxial growth due to its low lattice mismatch with respect to GaAs.

As a member of 3d transition metals, Co crystallizes with Al in a stable cubic B2 structure over a wide composition range (46-58 at. % Co) [112]. This ordered B2 structure can be considered as two interpenetrating primitive cubic sublattices [cf. Figure 7.1(a)], one occupied by Co and the other one by Al atoms. On the other hand, random occupancy of both sublattices by either Co or Al atoms introduces the transition from B2 to the basic bcc structures and, simultaneously, a change in the space group symmetry as indicated in Figure 7.1(b).

The atomic ordering is closely related to the physical properties of the intermetallic alloys. For instance, the degree of ordering in $Fe_xPt_yNb_z$ bulk alloys results in substantial variations in the Curie temperature [113]. Moreover, a slight atomic disordering in 3d transition metal aluminides – like FeAl or CoAl – from the equiatomic alloy to the metal rich one leads to the occurrence of local magnetic moments. This finding is explained by the formation of antisite defects, i.e. 3d transition metal atoms at Al sites, which are associated with an effective magnetic moment [114]. The exact knowledge of the mechanisms of order-disorder transitions in intermetallic alloys is, therefore, a prerequisite for a more detailed understanding of their electronic and magnetic behavior.

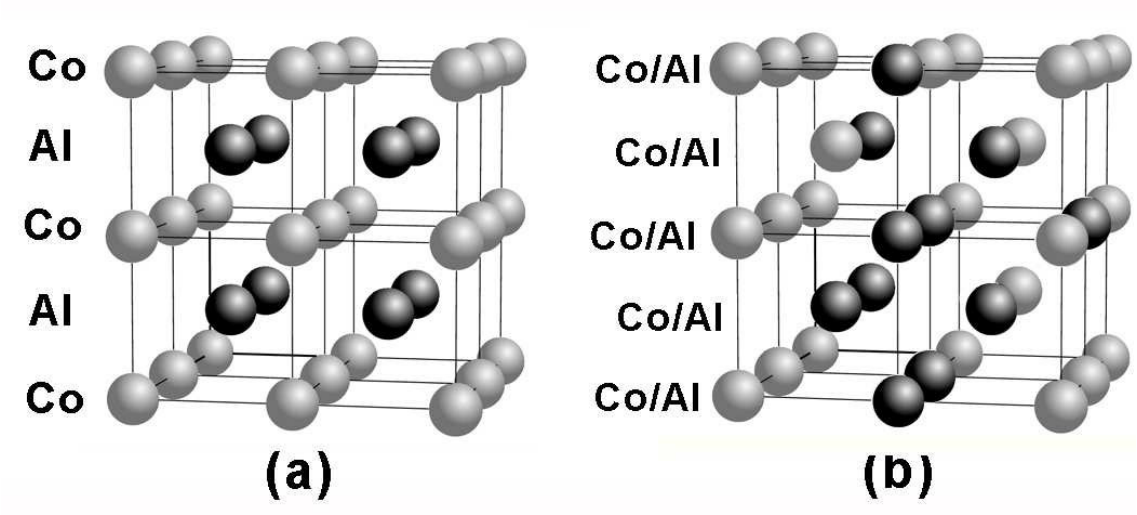

Figure 7.1: Schematic illustration of crystal structure of (a) B2 and (b) bcc phase of CoAl

The epitaxial growth of CoAl films on GaAs (001) substrates by MBE [115] has been systematically studied previously together with their overgrowth with semiconductor layers [116, 117]. However, there is no study about the order-disorder phenomena in these structures. It is thus the aim of the present work to investigate the microstructure of the intermetallic CoAl alloys. We focus on the atomic ordering of the metal layer and its relation with the interface configuration and growth condition.

7.2 Sample growth

The CoAl thin films are deposited on both GaAs (001) and GaAs (110) substrates in a two-chamber MBE system. After growing a superlattice of $Al_{0.3}Ga_{0.7}As$ and GaAs and a 1.2 nm thin AlAs buffer layer, which is intentionally used to suppress interface reactions between the intermetallic alloy and the compound semiconductor, the template is transferred into the As-free metal chamber. Subsequently, a 40 nm CoAl film is deposited with a very low growth rate in the range between 0.04 and 0.0735 nm/min. Samples are fabricated on GaAs (001) and (110) under identical MBE growth conditions except for the growth temperature, which is varied between 100 and 300°C.

7.3 CoAl on GaAs (001)

In-situ RHEED taken during growth indicates a cube-on-cube epitaxial orientation relationship between the CoAl and the GaAs crystal lattices: CoAl [110](001)|| GaAs [110](001). Based on this orientation, the natural lattice mismatch is calculated to be 0.8% along both in-plane directions. For the interpretation of the TEM images, diffraction calculations and contrast simulations are performed with the EMS^{TM} software [118].

7.3.1 Determination of local disordering in CoAl films

Figure 7.2(a) shows a dark-field TEM micrograph of the CoAl/template heterostructure, which is taken with the superlattice reflection $\mathbf{g} = 001_{CoAl}$. The image clearly displays

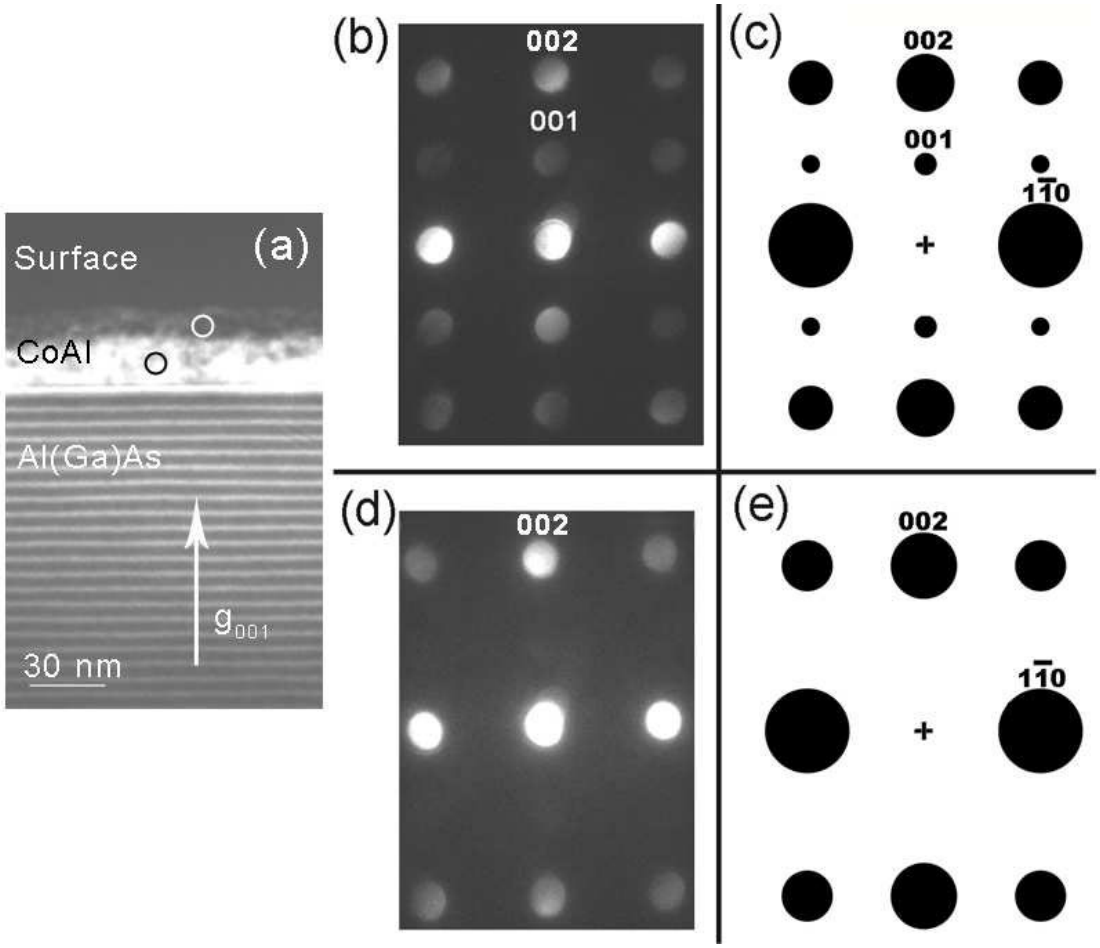

Figure 7.2: (a) (110) cross-sectional DF TEM image of the CoAl layer grown at 200°C with $\mathbf{g} = 001_{CoAl}$. The nano-beam diffraction patterns of neighboring regions (as indicated by circles in Figure 7.2(a)) are shown in (b) and (d). The simulated kinematical diffraction patterns of B2 (c) and bcc phase (e) of the CoAl alloy along the [110] zone axis are also shown for comparison. The size of the calculated reflections corresponds to these intensities.

dark regions in the CoAl film grown at 200°C. Since the intensity of the superlattice reflection decreases with the extent of disordering, the dark areas directly correspond to regions of reduced order. In addition to this fact, the Al(Ga)As layers of the template appears as bright stripes, because the chemical sensitive (002) reflection of zinc-blende structures are located very close to the (001) superlattice reflection of the intermetallic CoAl film, and thus both reflections are selected by the aperture.

Investigations using SAED are not applicable for the detection of fluctuations based on order-disorder transitions on the nanometer scale due to the relatively large aperture sizes available in the microscope. For this reason, nano-beam diffraction is utilized adjusting an electron beam diameter of about 2 nm. The Figures 7.2(b) and 7.2(d) show experimental nano-beam diffraction patterns of two neighboring bright and dark areas in the CoAl film [indicated by circles in Figure 7.2(a)]. The clear dissimilarity between these two patterns is discernible by the existence of the (001) reflection. The appearance of the reflections and their intensity are defined by their structure factor F. If CoAl is ordered, F_{001} is a nonzero value given by $f_{Co} - f_{Al}$, where f_{Co} and f_{Al} is the respective atom form factor of Co and Al. However, once Co and Al are mixed up, i.e., the or-

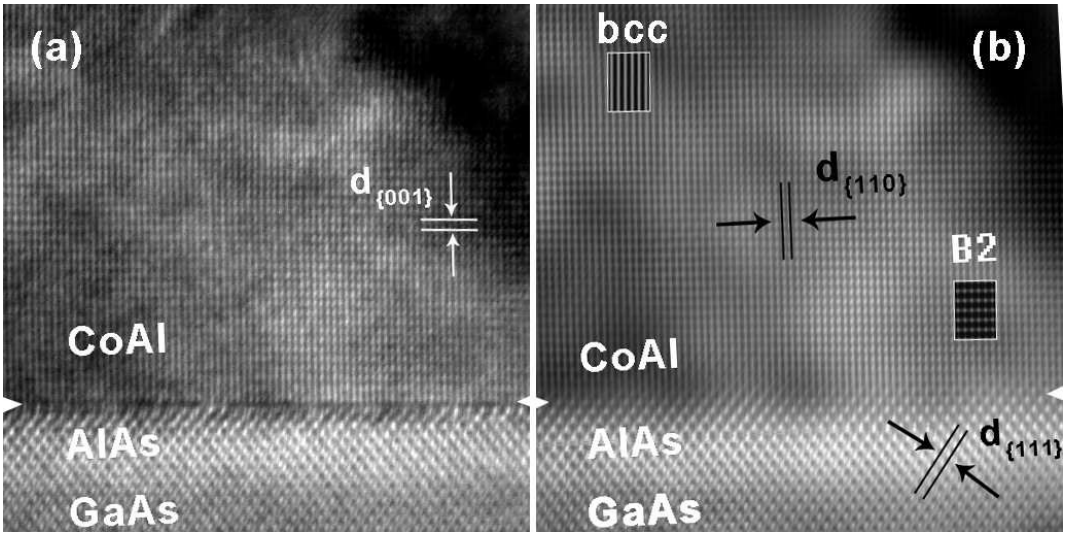

Figure 7.3: Cross-sectional HRTEM image of the hetero-system along [110] zone axis (a) and its Fourier-filtered version (b). The simulated contrasts of the B2 and bcc structures are inserted for clarification.

dering is destroyed, F_{001} equals to zero given by $f_{(Co,Al)} - f_{(Co,Al)}$, where $f_{(Co,Al)}$ is the average atom form factor of Co and Al. Spots like (001), which are present because of the ordering of the material, are generally called "superlattice" reflections. For further identification, kinematical diffraction simulations are performed based on the B2 and bcc structure and their corresponding results are revealed in Figure 7.2(c) and 7.2(e), respectively. The good agreement between the experimental and simulated diffraction pattern demonstrates that B2 and bcc phases are both present in the CoAl film.

The coexistence of ordered and disordered phases in the CoAl films is furthermore demonstrated by HRTEM investigations. Figure 7.3(a) shows the cross-sectional lattice image of the hetero-system near the interface obtained along the [110] zone axis of CoAl and GaAs. The experimental HRTEM micrograph has been Fourier-filtered in order to reduce the noise and improve the image contrast [Figure 7.3(b)]. The interface appears laterally smooth with a structural roughness of 1 to 2 monolayers. There is no indication of plastic relaxation of the lattice mismatch, i.e., the CoAl film is coherently strained. The HRTEM contrast inside the CoAl film in Figure 7.3 represents a simple interference pattern of lines running parallel to the {110} planes that locally turns into a rectangular point grid. The quantitative analysis of the HRTEM contrast requires image simulations, which are mainly dependent on the specimen thickness (t) and the objective defocus value (Δf) of the objective lens. The Figures 7.4(a) and 7.4(b) reveal simulated thickness-defocus maps for the bcc and the ordered B2 structure in the range of t between 4 and 8 nm and Δf between -30 and -80 nm. On the basis of these maps, it is figured out that the experimentally detected simple line patterns are in good accordance with simulated lattice images of the bcc structure at $t = 6$ nm and $\Delta f = -60$ nm, while the rectangular point grid patterns agree with the B2 structure at the same sample thickness and defocus values. Actually, since the interplanar lattice spacing belonging to the (002) reflection lies beyond the point resolution of our 300 kV microscope, the lattice image contrast of the bcc structure only displays vertical lines, which originate from the interference between the direct beam and the $(1\bar{1}0)$ reflection [cf. Figure 7.2(d)]. On the other hand, the presence of the (001) superlattice reflection of the B2 phase induces the visibility of

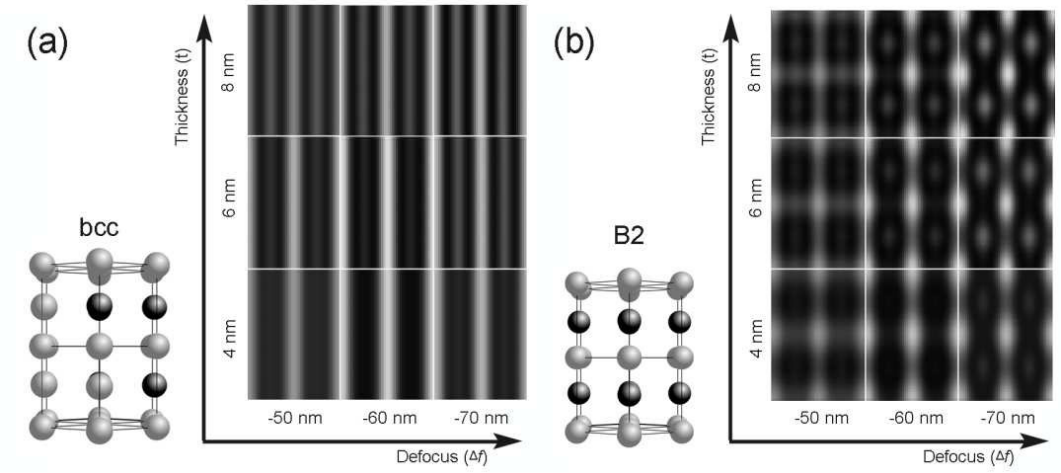

Figure 7.4: Thickness-defocus maps of the HRTEM contrast simulations for (a) bcc and (b) B2 phase of CoAl alloys along [110] zone axis.

lattice fringes parallel to the interface, and the HRTEM contrast results in a rectangular point grid pattern. Consequently, the experimental contrast in the CoAl film shown in Figure 7.3 is characterized by a predominating grid pattern (B2) in the region near the interface while the line pattern (bcc) is more pronounced away from the interface. This finding is in agreement with the results of the nano-beam diffraction and the dark-field imaging.

7.3.2 Influence of growth temperature

Generally, MBE is often used as a growth technique that is far away from thermodynamic equilibrium because surface diffusion processes are kinetically restricted. The growth kinetics determines the amount of incorporated point defects during MBE and thus affects the formation of disordering. Specific variations of the growth temperature should therefore open the possibilities to investigate the effect of order-disorder transitions and their results on the microstructure. Accordingly, samples grown at different temperature are observed by dark-field imaging using the (001) superlattice reflection under near two-beam condition. The micrographs provide information about the degree of disordering as well as the spatial distribution between ordered and disordered phases. The Figures 7.5(a)-–(c) present a series of cross-sectional (001) dark-field TEM micrographs of CoAl layers grown at 100°C, 200°C and 300°C. As explained, the bright and dark contrast inside the CoAl film corresponds to the B2 and bcc structure, respectively. Sample grown at 100°C has the largest fraction of ordered phase as indicated by a continuous bright band running parallel to the interface. When the growth temperature is increased to 200°C [cf. Figure 7.5(b)], the degree of ordering diminishes as recognizable in the interruptions of the bright band by many dark spots resulting in a more speckle-like contrast. For both specimens, the area near the surface is highly disordered. The coarsening of the speckle contrast in the CoAl film grown at 300°C [Figure 7.5(c)] demonstrates a further increase of disordering compared to the sample grown at 200°C. Surprisingly, no continuous dark band is observed near the surface region in this sample. On the other hand, an unusual array of periodic dark contrast is detected near the interface crossing the AlAs layer as indicated by arrows in Figure 7.5(c). The HRTEM image of such an area [Figure 7.5(d)]

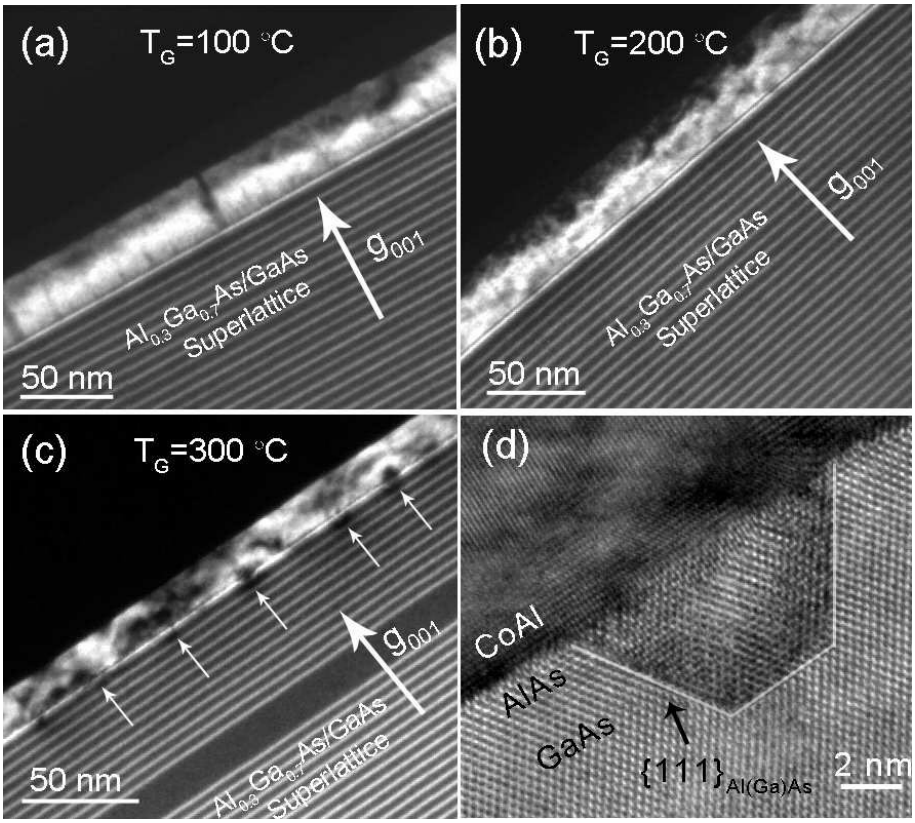

Figure 7.5: (110) cross-sectional dark-field TEM image of the CoAl layer grown at (a) 100°C, (b) 200°C and (c) 300°C with $\mathbf{g} = 001_{CoAl}$. The bright contrast in the CoAl layer is related to the B2 structure. Note the array of periodic interfacial dark areas in (c) as indicated by arrows. (d) HRTEM micrograph of a typical interface reaction region as marked in (c).

reveals a trapezoid shaped domain with side facets parallel to the {111} planes of AlAs and GaAs. The area of those domains extends from the CoAl film into the AlAs and GaAs buffer layer indicating the initiation of interface reaction when the growth temperature reaches 300°C. The HRTEM contrast inside the domain appears distorted compared to the ambient AlAs and GaAs suggesting the onset of a precipitation formation. Based on the results of the three samples, it can be deduced that the degree of disordering is smallest in the film grown at 100°C and increases with increasing temperature as expected for the thermal induced order-disorder transitions.

7.3.3 Influence of strain relaxation

The thickness of the epitaxial CoAl film is beyond the critical layer thickness for plastic relaxation that is calculated based on the Matthews-Blakeslee model. However, there is no indication for plastic relaxation by misfit dislocations at the interfaces for samples grown at 100°C and 200°C. The pseudomorphic growth of CoAl is demonstrated by the superposition of the in-plane $(110)_{CoAl}$ and $(220)_{Al(Ga)As}$ reflections in the selected area diffraction pattern shown in Figure 7.6(a). Accordingly, the splitting between the out-of-plane $(004)_{Al(Ga)As}$ and $(002)_{CoAl}$ reflections is detected that originates from the tetragonal distortion of the cubic CoAl lattice. Due to the lattice mismatch of 0.8% and the given film thickness of about 35 nm, strain energy is accumulated in the intermetallic film that

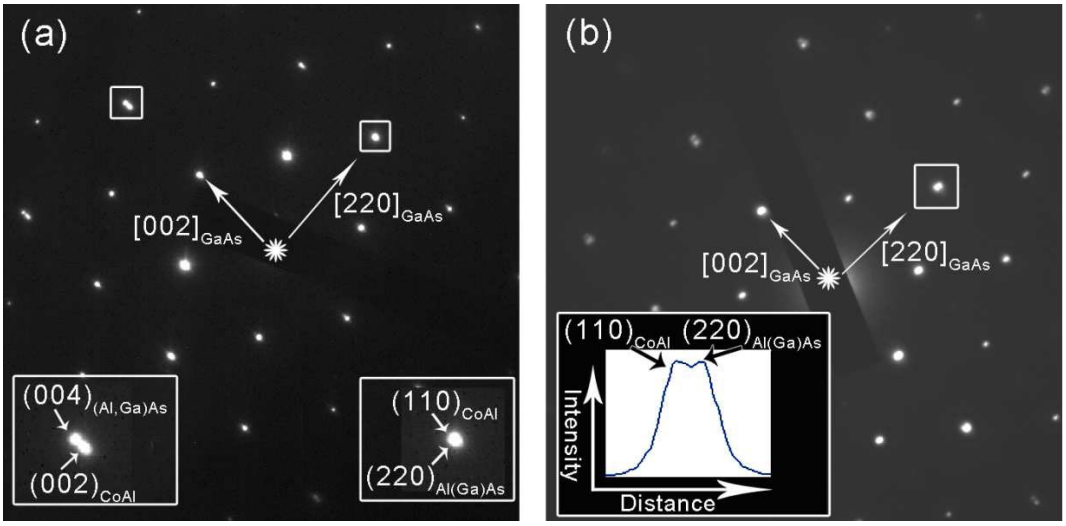

Figure 7.6: Selected area electron diffraction patterns of CoAl/template heterostructure grown at (a) 100°C and (b) 300°C with the electron beam along $[1\bar{1}0]$ zone axis. Notice that the split between $(110)_{CoAl}$ and $(220)_{Al(Ga)As}$ in (b) is revealed by an intensity line-scan.

should give rise to a stress-driven order-disorder phase transition. In fact, a continuous dark band is observed at around 30 nm away from the interface in the DF-TEM of the samples grown at 100 and 200°C [Figure 7.5(a) and 7.5(b)]. When the growth temperature is increased to 300°C, the lattice mismatch stress is partly relieved by a nearly periodic array of coherent precipitates along the interface generated as a consequence of the strong Co diffusion. This plastic relaxation process is clearly denoted by the separation of the in-plane $(110)_{CoAl}$ and $(220)_{Al(Ga)As}$ reflections as shown in Figure 7.6(b). That means that due to the epitaxial strain relief, there is no sufficient driving force for the order-disorder transition and, therefore, the corresponding dark band of a disordered phase along the surface region is not observed in the 300°C sample [Figure 7.5(c)].

7.3.4 Discussion

The compositional disorder in CoAl and some other B2-type intermetallics is dominated by the so-called triple-defect mechanism [10, 11]. Initially, vacancy pairs (V_{Al}-V_{Co}) are generated in crystals to conserve the stoichiometry. Such pairs have small binding energy and can easily dissociate in two single vacancies. Since an Al vacancy possesses a relative high formation energy, it is energetically favorable to exchange its position with one of its Co neighbors forming a Co vacancy, V_{Co}, and an antisite defect, Co_{Al}. The new defect pair, V_{Co}-Co_{Al}, has again low binding energy and easily dissociates into two single point defects [119, 120]. By this chain transformation, V_{Al}-V_{Co} turns into a dissociated triple defect, $2V_{Co}$+V_{Al}, which preserves the basic lattice structure, i.e. the lattice constant, however, changes the crystal symmetry from ordered B2 to disorder bcc, as schematically shown in Figure 7.7. With increasing temperature, the equilibrium concentrations of vacancies and antisites involved in the triple-defect become higher and, accordingly, the fraction of disordered bcc phase in the alloy will be accumulated. Furthermore, the Co atoms are very active in the CoAl system. They may diffuse out of their original lattice sites leaving vacancies behind, and occupy the available Al sites or stop

in interstitial positions, which introduces local disordering. Such disordering increases with increasing temperature because of the higher diffusivity of Co atoms. During MBE growth, these disordering effects are even more pronounced because the growth of our CoAl films is far away from thermodynamic equilibrium. Consequently, a smaller degree of disordered phase is observed in our experiment for the sample grown at lower temperature.

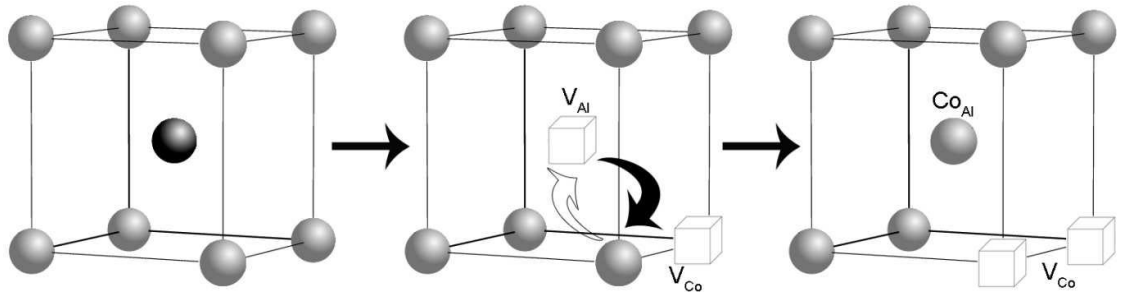

Figure 7.7: Schematic illustration of the triple-defect mechanism in the CoAl alloy [119, 120].

Provided that there are deviations from stoichiometry, another disorder mechanism is also feasible. Since Co vacancies (V_{Co}) and Co_{Al} antisites are the most stable point defects, an excess of Co atoms is accommodated by the generation of remaining Co_{Al}, whereas a excess of Al is accommodated by the generation of remaining V_{Co} [112]. These so-called constitutional point defects as shown in shown in Figure 7.8 lead to the modification of the lattice symmetry. However, the quantitative investigation of the chemical composition and point defect density is beyond the scope of the current work.

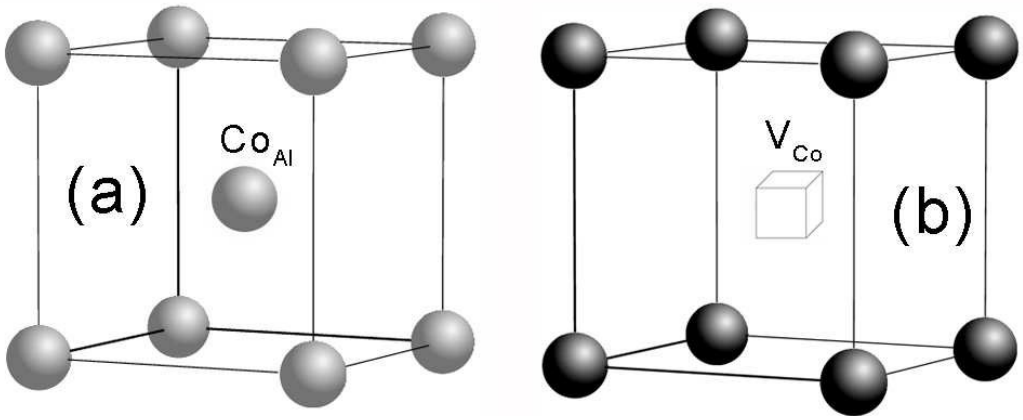

Figure 7.8: Compositional defects in (a) Co-rich and (b) Al-rich CoAl crystal.

In order to find the main diffusing species in the system, a compositional and structural analysis needs to be performed in order to identify the interfacial reaction products in the sample grown at 300°C [Figure 7.5(d)], which is, however, complicated by the small size of the precipitates. Therefore, the sample is in-situ annealed at 500°C inside the MBE system for half an hour to intensify the interfacial reaction. Figure 7.9(a) shows the high-resolution TEM micrograph of the interface in the annealed sample along the $[1\bar{1}0]_{GaAs}$ zone axis. The reaction is obviously progressed compared to the as-grown case as indicated by the quasi-trapezoid shaped precipitate, which is characterized by a HRTEM contrast that is different to that of the CoAl B2 structure or the Al(Ga)As zinc-

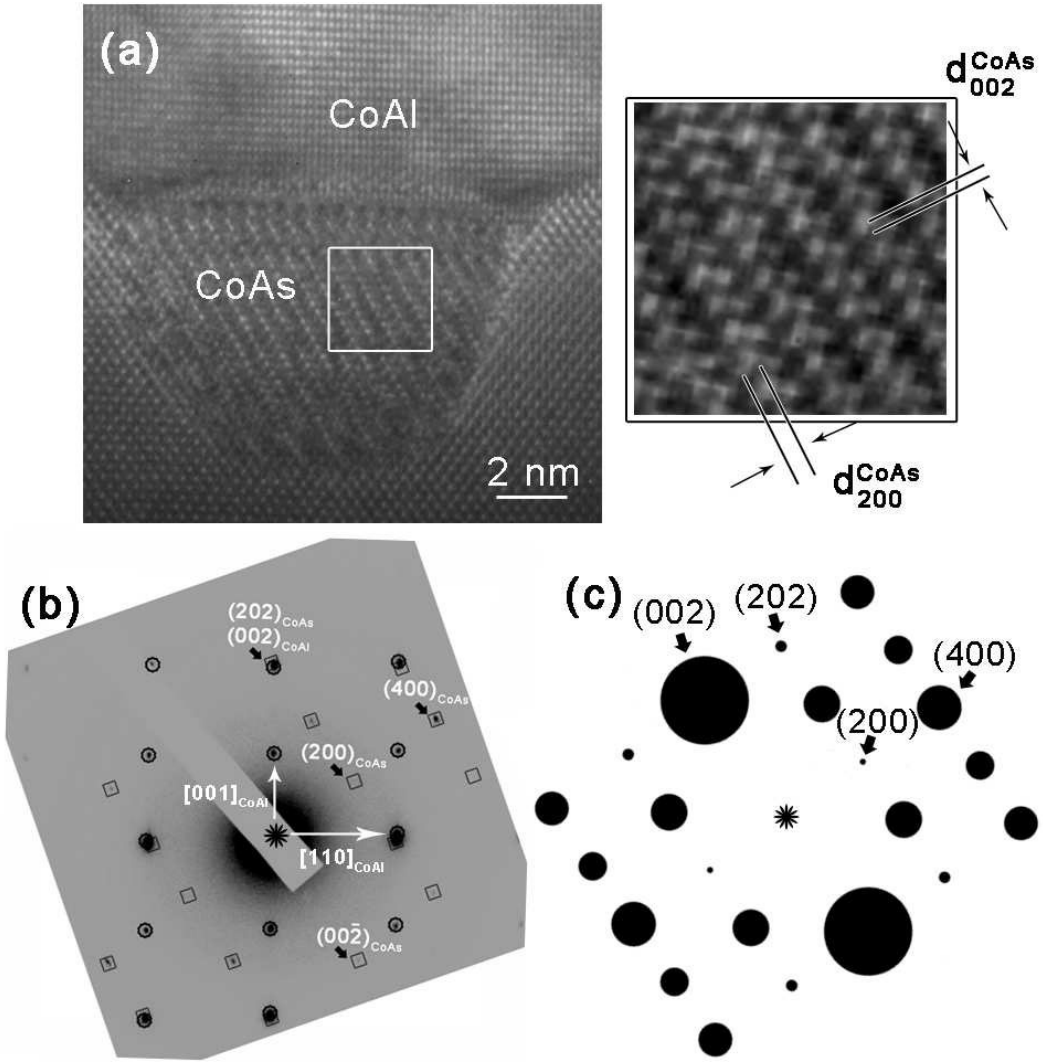

Figure 7.9: (a) Cross-sectional HRTEM micrograph of the interfacial reaction region in the 300°C grown sample annealed at 500°C for half an hour (electron beam along the GaAs $[1\bar{1}0]$ zone axis). The magnified lattice image of the reaction region is indicated on the right. (b) Electron diffraction pattern formed from the intermetallic film and the reaction region taken along the $[1\bar{1}0]_{CoAl}$ zone axis. The spots marked with circles and squares belong to those from CoAl and CoAs, respectively. (c) Simulated diffraction pattern of CoAs along the $[010]_{CoAs}$ direction.

blende structure, respectively. The corresponding selected area diffraction pattern along the $[1\bar{1}0]_{CoAl}$ direction is presented in Figure 7.9(b). Besides the reflections from the B2 type CoAl, an additional rectangular pattern is detected that belongs to the precipitate. A careful comparison with diffraction patterns from different possible compounds along various zone axes reveals that the arrangement of the additional spots agrees well with the diffraction pattern of the CoAs compound along the [010]-direction, whose simulated version is shown in Figure 7.9(c). The crystallographic structure of CoAs corresponds to an orthorhombic unit cell which has the space group $Pna2_1$ and the lattice parameters $a = 0.5286$ nm, $b = 0.5868$ nm and $c = 0.3448$ nm [121, 122]. The lattice spacings $d^{\mathrm{CoAs}}_{(200)}$ and $d^{\mathrm{CoAs}}_{(002)}$ obtained from the SAED patterns are 2.62 ± 0.05 Å and 1.76 ± 0.05 Å, respec-

tively, which correspond well to the theoretical bulk values. It is thus concluded that the interfacial reaction takes place predominantly by Co in-diffusion into the buffer layer. As a result of the reaction, a new phase is nucleated with the low-energy topotaxial orientation relationship: $[010](200)_{CoAs}||[110](111)_{Al(Ga)As}$ and $[010](202)_{CoAs}||[110](002)_{CoAl}$.

When the sample has been grown at 300°C, the thermal activation energy for Co diffusion is sufficient to overcome the barrier at the interface leading to the nucleation of CoAs inside the AlAs and GaAs buffer layer. The nuclei are grown coherently at the interface surrounded by trapezoid domains, where a high concentration of Co atoms is incorporated. These domains are terminated by {111} side facets according to the AlAs and GaAs crystal lattices, because the diffusion along these close packed planes is most rapid due to their lowest diffusion activation energy [123]. The size of the domain is limited by the diffusion length of Co atoms. When the as-grown sample is further annealed, an increased number of Co atoms are able to reach the interface to the precipitate resulting in its coarsening and the formation of a shape that corresponds to a minimal interfacial energy.

7.4 CoAl on GaAs (110)

Epitaxial growth of CoAl on GaAs (110) is more difficult to control than its (001) counterpart, because of the missing surface reconstructions and high probability of interfacial reactions. To acquire a high quality film, in the present study, we apply the growth parameters of (001) oriented samples with the highest degree of ordering to the deposition of CoAl on CoAl (110) substrate.

7.4.1 Microstructure

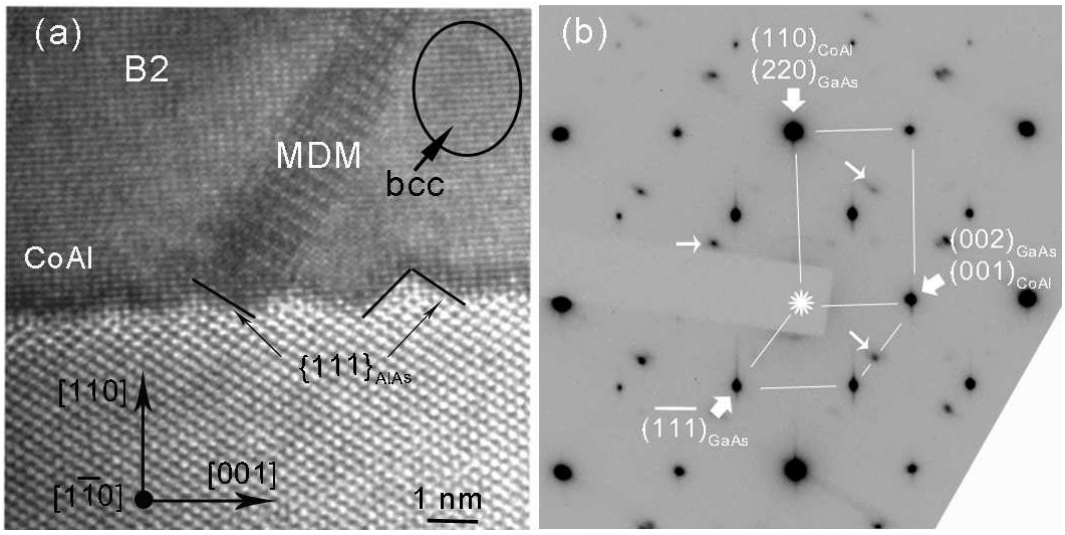

Figure 7.10: (a) Cross-sectional HRTEM image of the CoAl/GaAs (110) heterostructure. Note the interference pattern of lines running parallel to (110) planes as indicated by the ellipse. (b) SAED pattern of the heterosystem. The spots marked with narrow arrows are those from MDMs. All images are taken with electron beam parallel to the $[1\bar{1}0]$ zone axis.

Figure 7.10(a) shows the cross-sectional HRTEM image of the CoAl/template heterostructure near the interface obtained along the $[1\bar{1}0]$ zone axis of CoAl and GaAs.

Short facets are present at the interface along the {111} planes of AlAs, from where a misoriented domain (MDM) is originated. Inside the metal film, a simple interference pattern of lines running parallel to the {110} planes (as highlighted by the ellipse) is observed in addition to the rectangular point grid. As demonstrated in the previous chapter, they are corresponding to the disordered bcc and B2 phase of CoAl, respectively. The SAED pattern of the heterostructure in Figure 7.10(b) represents a high degree of crystallinity of the metal layer. The arrangement of the spots marked by rectangle reveals a B2/bcc structure of CoAl, which has the expected epitaxial orientation relationship with respect to the substrate: $[001](110)_{CoAl}||[001](110)_{GaAs}$. There is no separation of spots found between $(001)_{CoAl}$ and $(002)_{GaAs}$ as well as between $(110)_{CoAl}$ and $(220)_{GaAs}$, implicating that the interplanar spacing differences between CoAl and GaAs along both in-plane and out-of plane directions are too small and beyond the sensitivity of SAED methods. Considering the fact that the natural misfit of about 0.8% between these two materials is large enough for SAED to detect, we conclude that the mismatch strain in CoAl is partially relieved. Additional reflections corresponding to MDMs are also present indicated by the narrow arrows in Figure 7.10(b). Notice there is no overlap between these reflections and the ones shown in the CoAl/GaAs diffraction patterns.

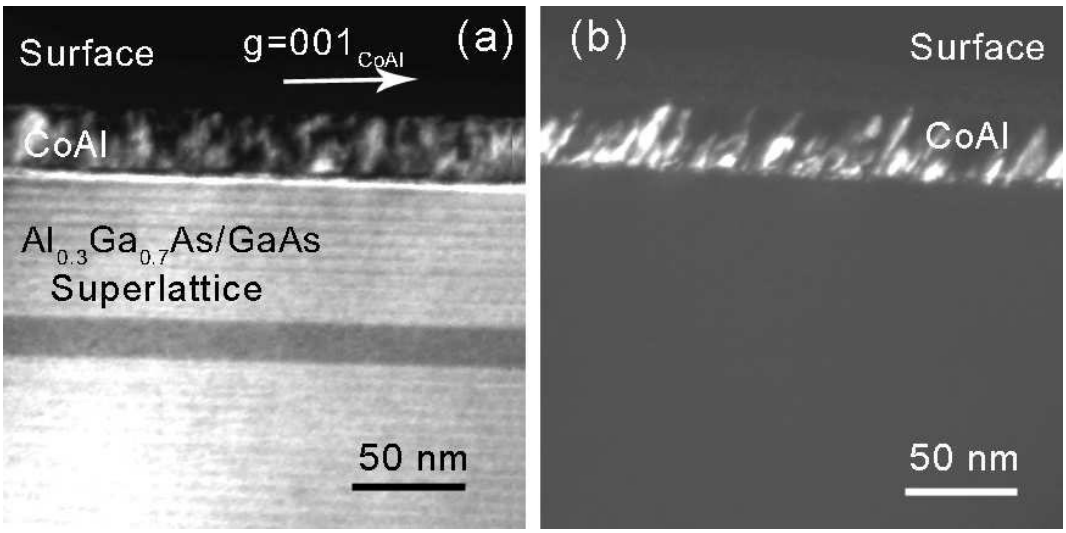

Figure 7.11: Cross-sectional DF TEM image of the (110) oriented CoAl layer along the $[1\bar{1}0]$ direction with (a) $(001)_{CoAl}$ and (b) the reflection from MDMs selected. The bright contrast in the CoAl layer in (a) and (b) is related to the B2 CoAl and the misoriented domains, respectively.

Figure 7.11(a) shows a DF TEM micrograph of the heterostructure, which is taken with the superlattice reflection $\mathbf{g} = 001_{CoAl}$ under near two-beam condition. Since there is no overlap between the reflections from MDMs and CoAl, the micrograph provides information about the volume fraction as well as the spatial distribution of the ordered B2 phases of CoAl. The bright contrast inside the metal film corresponds to the B2 type CoAl, whereas the dark contrast corresponds to the disordered bcc phase and the MDMs. The film is characterized by a predominating dark contrast, which is interrupted by some columnar bright stripes. Dark spots are also present in these stripes resulting in a more speckle-like contrast locally. Since the diffusion induced B2-bcc order-disorder transition is more likely to produce much localized disordering, e.g. dark spots in the bright stripe, rather than a large block of disordered area (cf. Figure 7.11(a)), we deduce that these

MDMs are mainly responsible for the diminishment of the B2 type CoAl. This inference is supported by the DF image of the same area with only the reflection of the MDMs selected as shown in Figure 7.11(b). A large amount of bright stripes, corresponding to MDMs, contribute predominately to the decrease of ordering in the metal layer. Furthermore, there is no obvious dark band of disordered domain visible close to the surface of the heterostructure as shown in Figure 7.11(a), representing that the stress-driven order-disorder transition in this case is neglectable. Such finding confirms the plastic relaxation in the CoAl film.

7.4.2 Misoriented domains

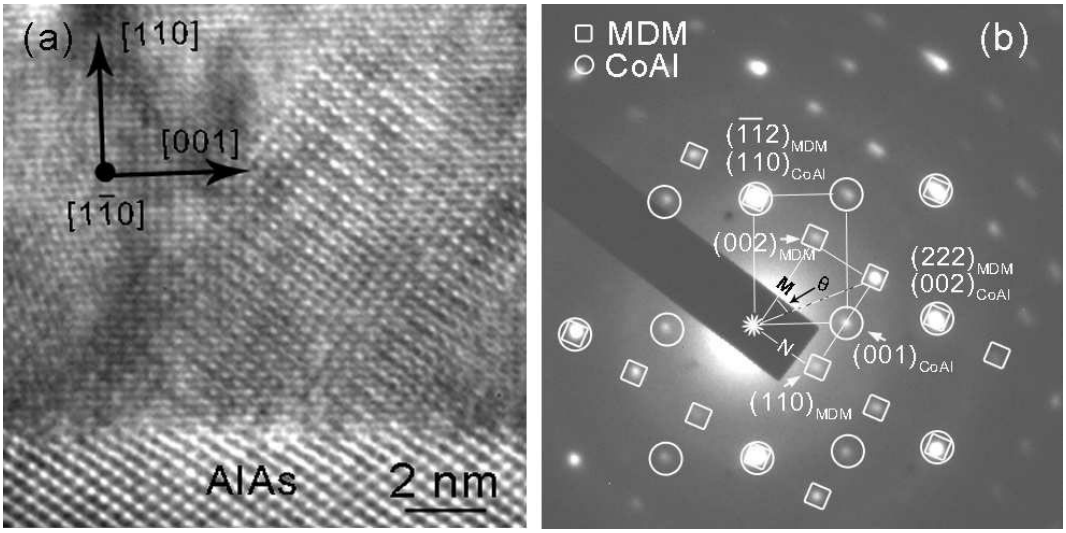

Figure 7.12: (a) Cross-sectional HRTEM micrograph the heterostructure along the $[1\bar{1}0]$ direction and (b) the corresponding SAED pattern with only the intermetallic film selected. The spots marked with circles and squares belong to those from CoAl and MDMs, respectively.

Figure 7.12(a) highlights the lattice image of the MDMs, which is characterized by a point grid interference pattern. The MDMs arise from the interface and extend through the whole layer to the surface. No plastic relaxation related defect is found at the domain boundary as well as along the interface. Rather than distribute randomly in the metal layer, which is an implication of the local disordering, MDMs have a unique orientation relationship with respect to the surroundings, representing that they are formed at the nucleation stage of the layer and propagate with the growth of CoAl.

For a better understanding of the microstructural properties of the metal film, electron diffraction is performed with only the metal film selected to rule out the affect of the substrate. Figure 7.12(b) illustrates a mixture of two sets of diffraction patterns corresponding respectively to B2/bcc type CoAl (marked by circles) and MDMs (marked by squares). The rectangular grid pattern from MDMs gives the ratio of the spot spacing $M/N = 1.40 \pm 0.05$ and the angle $\theta = 35.1 \pm 0.3°$, which agree well with the theoretical values of the [110] diffraction pattern of a bcc lattice structure: 1.414 and 35.26°, respectively. Therefore, the reflections from MDMs can be indexed according to bcc structure as can be seen. By selecting its $(222)_{MDM}$ reflection superimposing $(002)_{CoAl}$, the lattice constant is calculated to be equal to $\sqrt{3}a_{CoAl}$ giving a value of 0.495 ± 0.005 nm.

The epitaxial orientation relationships between MDM and CoAl and the substrate

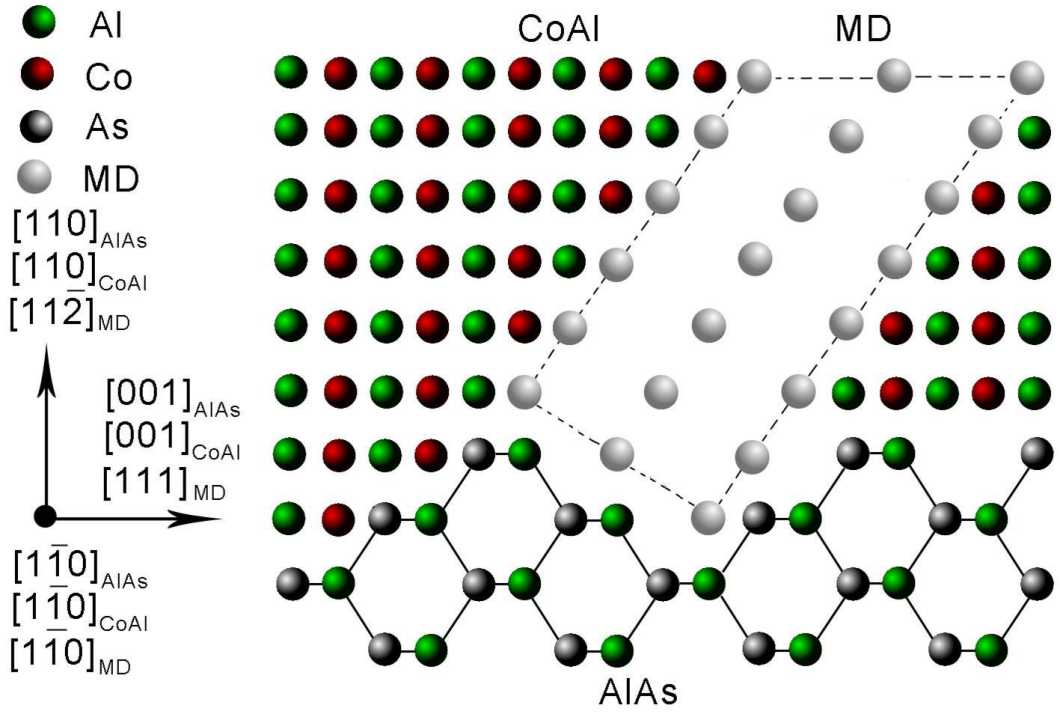

Figure 7.13: Projectional view of the atomic model of the heterosystem along the $[1\bar{1}0]$ direction.

are determined from HRTEM images and diffraction patterns as following:
for side facets to the CoAl matrix:

$$[1\bar{1}0](110)_{MDM}||[1\bar{1}0](11\bar{2})_{CoAl},$$

for bottom surface to the substrate:

$$[1\bar{1}0](001)_{MDM}||[1\bar{1}0](111)_{AlAs}.$$

Subsequently, an atomic model is built for a straightforward visibility of the interface configuration. Figure 7.13 illustrates the projectional view of the model along the $[1\bar{1}0]$ direction, in order to compare with the HRTEM image in Figure 7.12(a). MDM is originated from the {111} facets with its square (001) planes parallel to the hexagonal (111) close-paced planes of AlAs. For the interface with totally different symmetries on both sides, the low-energy interfaces are often discussed in terms of the geometry, mostly based on structural coincidences between the adjoining crystal lattices. The perfect match along the $[11\bar{2}]_{AlAs}||[110]_{MDM}$ direction between the MDM and AlAs, as well as along the $[111]_{AlAs}||[001]_{MDM}$ between the MDM and CoAl, obviously offers a good reason for the present orientation relationship. Besides, it's worth noting that not every facet at the interface would lead to the formation of MDM, and CoAl is also possible to be formed with the expected orientation relationship $[001](110)_{CoAl}||[001](110)_{AlAs}$.

7.4.3 Discussion

The (110) oriented CoAl films are suffered from a strong diminishment of the ordered B2 phase. There are two factors accounting: 1) the diffusion induced order-disorder transition and 2) the emergence of MDMs originated from the facets at the interface. In contrast, CoAl alloys grown on GaAs (001) under the same condition display a much higher volume fraction of B2 phase, mainly because they have an atomically abrupt interface and accordingly no existence of MDMs. The reason for the differences in the interface property of the (001) and (110) oriented heterostructure is not clarified yet. The roughening of AlAs (110) surface at the initial stage of CoAl epitaxial growth is probably due to the special atomic configuration of the (110) surface.

Chapter 8

Summary and outlook

Summary The aim of the present work is to systematically investigate the microstructural properties of (110) oriented heterostructures on GaAs substrates. In contrast to the GaAs (001) surface, GaAs (110) has a nonpolar surface characterized by an inequilateral rectangular surface mesh, and therefore, (110) oriented heterostructures reveal a completely different mechanical behavior compared to its well-studied (001) counterpart. In this thesis, three heterosystems with distinct materials grown on GaAs (110) are investigated by various techniques of TEM. Special interests are addressed to the interface configurations, which determine the epitaxial orientation, misfit strain accommodation mechanisms and the related defect structure.

Fcc-type (Al,Ga)As/AlAs/GaAs multilayer structure on GaAs (110) displays a simple epitaxial orientation relationship: (Al,Ga)As [001](110)||GaAs [001](110). The strain relaxation follows two stages for this low mismatched system due to the reduced number of active slip systems. The first stage involves relaxation along [001] direction by the formation of planar defects via the $\langle 110\rangle\{111\}$ slip system. Partial relaxation in the perpendicular $[1\bar{1}0]$ direction is achieved with the activation of the $\langle 011\rangle\{131\}$ slip system at the second stage. An interesting finding is that all the plastic relaxation is inhibited by the introduction of more SPSL into the system. This is partially explained by the small individual layer thickness hindering the homogeneous dislocation nucleation and partially by the lower dislocation mobility due to a large number of interfaces and epilayers with different strain states. In order to verify the effect of the SPSL against dislocation expansion, artificial defects are intentionally introduced by nano-indentation. The reaction between the dislocation and the interfaces shown in the BF image of the indented sample, demonstrate that SPSL is a reasonable way of stabilizing the heterostructure again plastic relaxation.

As a unique model of heteroepitaxy, hcp-type MnAs on GaAs (110) system is characterized by their totally different crystal symmetries and large lattice mismatches between the epilayer and the substrates. The epitaxial orientation is determined as: MnAs $[11\bar{2}0](1\bar{1}00)||$GaAs$[1\bar{1}0](110)$, representing anisotropic lattice mismatches of -7.5% and 0.7% along the $[11\bar{2}0]$ and [0001] direction, respectively. MnAs grows on GaAs (110) via a SK-mode. The strain corresponding to the 0.7% lattice misfit is accommodated elastically along the [0001] direction. For the perpendicular $[11\bar{2}0]$ direction, the mismatch stress is relived by the formation of a periodic array of perfect misfit dislocations, which are characterized by a Burgers vector of $a/3[11\bar{2}0]$ with a stand-off position in MnAs lattice. The elastic distortion is confined at the interface within a thickness of about 3.4 nm, which is the consequence of the compensation of the strain fields from the respective dislocations in the periodic array. Based on the HRTEM image of the coherent part between misfit dislocations, an interfacial atomic configuration is proposed and verified by the good agreement between the simulations and experimental images. In addition, we have investigated the overgrowth of GaAs on MnAs films. The growth proceeds via a Volmer-

Weber mode. A high density of stacking faults and twins are present in the overgrown GaAs films. Their formation mechanism is discussed with respect to the deposition errors during the adsorption of atoms on {111} facets of GaAs nuclei.

Ordered B2-type intermetallic CoAl alloys are realized on (001) and (110) oriented GaAs substrates for comparison. The epitaxial orientation relationship in CoAl/GaAs (001) is identified as CoAl [110](001) || GaAs [110](001). Bcc phase appears in the CoAl epilayer, which is the disordered version of the B2 crystal lattice type. The disordering is induced partially by the epitaxial strain and partially by the diffusion of point defects, including vacancies and Co atoms. Variations in the growth temperature between 100 and 300°C reveal that the degree of diffusion induced disordering and the volume fraction of the disordered bcc phase increase with increasing temperature due to the higher diffusivity and larger concentrations of vacancies and Co antisite defects. Interface reactions are observed in the sample fabricated at 300°C resulting in the formation of CoAs precipitates at the interface. These precipitates contribute to the plastic relaxation of the 1.2% lattice mismatch between the CoAl film and the GaAs substrate and lead to the diminishment of the strain-induced order-disorder transition.

(110) oriented CoAl layers are grown under the same conditions as (001) oriented samples with the highest degree of ordering. The epitaxial orientation relationship is CoAl [001](110) || GaAs [001](110). A much smaller fraction of B2-type CoAl is observed in the metal layer as compared to its (001) counterpart. The diminishment is explained by the diffusion induced order-disorder transition and the emergence of misoriented domains. The formation of such domains is originated from {111} facets developed along the interface roughness.

Future work MnAs undergoes magnetoelastic phase transitions accompanying with discontinues volume changes at about 318 K, where the lattice parameter **a** decreases abruptly by about 1% and **c** remains essentially unchanged. Such property leads to an inaccuracy in the residual strain measurement because of the possible specimen heat-up by high-energy electrons in the microscope. A temperature controllable TEM measurement is therefore necessary to rule out these disturbances, where the specimen temperature can be preserved at a given value. Furthermore, it would be very interesting to observe the dislocation evolution (microstructure and movement) with the changing temperature.

Since the magnetic property of CoAl is closely related to the disordering of the metal layer, it will be very helpful if we can analyze quantitatively the volume fraction of the disordered phase and its temperature dependence. The volume fraction of the disordering can be obtained by measuring the intensity of the superlattice reflection (001) as compared to the (002) reflection in the SAED pattern with the same area selected. By using the temperature controllable TEM, the correlation between the disordering and the temperature can be acquired. In addition, a smooth interface can be reached for (110) oriented CoAl by optimizing the growth parameters. If the formation of the misoriented domains can be prohibited, the comparison of the disordering in the CoAl with different orientations will be interesting.

Bibliography

[1] D. V. Lang, C. H. Henry. Phys. Rev. Lett. 35, 1525 (1975)

[2] Y. Seki, H. Watanabe, and J. Matsui. J. Appl. Phys. 49, 822 (1978)

[3] I. Zutic, J. Fabian, S. D. Sarma. Rev. Mod. Phys. 76, 323 (2004)

[4] S. A. Wolf, D. D. Awschalom, R. A. Buhrman, J. M. Daughton, S. von Molnar. M. L. Roukes. A. Y. Chtchelkanova, D. M. Treger. Science 294, 1488 (2001)

[5] W. A. Harrison, E. A. Kraut, J. R. Waldrop, R. W. Grant. Phys. Rev. B. 18, 4402 (1978)

[6] H. Kroemer, K. J. Polasco, S. C. Wright. Appl. Phys. Lett. 36, 763(1980)

[7] D. Sun, E. Towe, P. H. Ostdiek, J.W. Grant, G. J. Vansuch. IEEE J. of Selected Topics in Quantum Electronics 1, 674 (1995)

[8] T. Mizuno, N. Sugiyama, T. Tezuka, T. Numata, S. Takagi. Symp. VLSI 97 (2003)

[9] A. Dimoulas, E. Gusev, P. C. McIntyre, M. Heyns. Advanced Gate Stacks for High-Mobility semiconductors, Springer, Heidelberg, Germany, 2007

[10] F. Reiher, A. Dadgar, J. Blaesing, M.Wieneke, A. Krost. J. Cryst. Growth 312, 180 (2010)

[11] G. A. Prinz. Phys. Today. 48, 58 (1995)

[12] D. Kolovos-Vellianitis, C. Herrmann, L. Daeweritz. K. H. Ploog. Appl. Phys. Lett. 87, 092505 (2005)

[13] Y. Ohno, R. Terauchi, T. Adachi, F. Matsukura, H. Ohno. Phys. Rev. Lett. 83, 4196 (1999)

[14] J. R. Arthur. J. Appl. Phys. 39, 4032 (1968)

[15] A. Y. Cho. J. Appl. Phys. 41, 782 (1970)

[16] G. Scoles. Atomic and molecular beam methods, Oxford University Press, New York, USA, 1988

[17] M. A. Herman, W. Richter, H. Sitter. Epitaxy: physical principles and technical implementation. Springer-Verlag, Berlin, Germany, 2004

[18] L. Daeweritz. Rep. Prog. Phys. 69, 2581 (2006)

[19] S. Iyer, H. Morkoc, H. Zabel, N. Otsuka. Comments Cond. Matter Phys. 15, 1 (1989)

[20] J. H. Van der Merwe. Crit. Rev. Solid State Mater. Sci. 17, 187 (1991)

[21] J. A. Venables, G. D. T. Spiller, M. Hanbuecken. Rep. Prog. Phys. 47, 399 (1984)

[22] Y. Nabetani, N. Yamamoto, T. Tokuda, A. Sadaki. J. Cryst. Growth 146, 363 (1995)

[23] R. Hull and E. A. Stach. Curr. Opin. Solid State Mater. Sci. 1, 21 (1996)

[24] R. Hull and J. C. Bean. Crit. Rev. Solid State Mater. Sci. 17, 507 (1992)

[25] D. J. Dunstan. J. Mater. Sci.: Mater. Electr. 8, 337 (1997)

[26] J. W. Edington. Practical electron microscopy in materials science. N. V. Philip's Gloeilampenfabrieken, Eindhoven, Netherland, 1976

[27] L. Reimer. Transmission electron microscopy: physics of image formation and microanalysis. Springer-Verlag, Berlin, Germany, 1984

[28] M. Gao, J. M. Zuo, R. D. Twesten, I. Petrov, L. A. Nagahara and R. Zhang. Appl. Phys. Lett. 82, 2703 (2003)

[29] Http://courses.eas.ualberta.ca/eas421/lecturepages/microstructures.html

[30] D. Hull and D. J. Bacon. Introduction to dislocations. Pergamon Press, New York, USA, 1984

[31] S. C. Jain, A. H. Harker, R. A. Cowley. Phil. Mag. A. 75, 1061 (1997)

[32] C. A. B. Ball, J. H. Van der Merwe. Dislocations in solids. Elsevier, Amsterdam, Holland, 1983

[33] J. W. Matthews, A. E. Blakeslee. J. Cryst. Growth 27, 118 (1974)

[34] P. M. J. Maree, J. C. Barbour, J. F. van der Veen, K. L. Kavanagh, C. W. T. Bulle-Lieuwma and M. P. A. Viegers. J. Appl. Phys. 62, 4413 (1987)

[35] A. Keely, G. W. Groves and P. Kidd. Crystallography and crystal defects. Wiley, Weinheim, Germany, 2000

[36] A. Trampert. Physica E 13, 1119 (2002)

[37] R. Hull, J. C. Bean, Y. H. Xie. Proc. Mater. Res. Soc. 37, 153 (1991)

[38] W. Wegscheider, H. Cerva. J. Vac. Sci. Technol. B. 11, 1056 (1993)

[39] M. Dynna, A. Marty, B. Gilles, G. Patrat. Acta. Mater. 45, 257 (1997)

[40] D. Halley, Y. Samson, A. Marty, P. Bayle-Guillemaud, C. Beigne, B. Gilles, J. E. Mazille. Phys. Rev. B 65, 205408 (2002)

[41] X. Zhang, D. W. Pashiley. J. Mater. Sci: Mater in Electron. 7, 361 (1996)

[42] V. Gopal, A. L. Vasiliev, and E. P. Kvam. Proceeding of MRS Spring, USA, 2001

[43] A. Trampert, K. H. Ploog. Cryst. Res. Technol. 35, 793 (2000)

[44] A. Trampert, F. Schippan, L. Daeweritz, K. H. Ploog. Appl. Phys. Lett. 78, 2461 (2001)

[45] A. Trampert, O. Brandt, H. Yang, K. H. Ploog. J. Phys. III France 7, 2309 (1997)

[46] F. Ernst, P. Pirouz. J. Appl. Phys. 64, 4526 (1987)

[47] F. Ernst, P. Pirouz. J. Mater. Res. 4, 834 (1989)

[48] K. Y. Cheng, K. C. Hsieh, J. N. Baillargeon. Appl. Phys. Lett. 60, 2892 (1992)

[49] F. Glas. J. Appl. Phys. 62, 3201 (1987)

[50] V. M. Kaganer, B. Jenichen, F. Schippan, W. Braun, L. Daeweritz, K. H. Ploog. Phys. Rev. Lett. 85, 341 (2000)

[51] D. W. Pashley. Thin Films 1, 59 (1964)

[52] A. Armigliato, S. Frabboni and G. C. Gazzadi. Appl. Phys. Lett. 93, 161906 (2008)

[53] D. B. Williams and C. B. Carter. Transmission electron microscopy: imaging. Plenum Press, New York, USA, 1996

[54] S. Y. Tong, A. R. Lubinski, B. J. Mrstik, M. A. Van Hove. Phys. Rev. B 17, 3303 (1978)

[55] W. D. Nix. Metall. Trans. A 20, 2217 (1989)

[56] R. Hull, J. C. Bean, L. Peticolas, D. Bahnck. Appl. Phys. Lett. 59, 964 (1991)

[57] X. Zhang, D. W. Pashley, J. H. Neave, P. N. Fawcett, J. Zhang, B. A. Joyce. J. Cryst. Growth. 132, 331 (1993)

[58] X. Zhang, D. W. Pashley, J. H. Neave, P. N. Fawcett, B. A. Joyce. J. Cryst. Growth. 131, 300 (1993)

[59] X. Zhang, D. W. Pashley, J. H. Neave, L. Hart, B. A. Joyce. J. Appl. Phys. 78, 6454 (1995)

[60] N. Oyama, E. Ohta, K. Takeda, K. Shiraishi, H. Yamaguchi. Surf. Sci. 433-435, 900 (1999)

[61] D. Maroudas, L. A. Zepeda-Ruiz, W. H. Weinberg. Surf. Sci. 411, 865 (1998)

[62] K. Okajima, K. Takeda, N. Oyama, E. Ohta, K. Shiraishi, T. Ohno. Jpn. J. Appl. Phys. 39, 917 (2000)

[63] R. Hull, J. C. Bean, L. Peticolas, D. Bahnck, B. E. Weir, L. C. Feldman. Appl. Phys. Lett. 61, 2802 (1992)

[64] R. Hey, A. Trampert, P. Santos. Phys. Stat. Sol. (c). 3, 651 (2006)

[65] R. Hey, U. Jahn, Q. Wan, A. Trampert. Phys. Stat. Sol. (c). 5, 2917 (2008)

[66] R. Hey, A. Trampert, U. Jahn, O. D. D. Couto Jr., P. Santos. J. Cryst. Growth. 301-302, 158 (2007)

[67] M. Yoshita, H. Akiyama, L. N. Pfeiffer, K. W. West. Appl. Phys. Lett. 81, 49 (2002)

[68] S. Sharan, J. Narayan, J.C.C. Fan. J. Electronic Mater. 20, 779 (1991)

[69] S. Medach, C. M. Hu, Ch. Heyn. Physica E 13, 1204 (2002)

[70] Y. Takagi, H. Yonezu, S. Uesugi and N. Ohshima. Jpn. J. Appl. Phys. 36, 187 (1997)

[71] T. Kawai, H. Yonezu, Y. Ogasawara. J. Appl. Phys. 74, 7257 (1993)

[72] W. Hagen, H. Strunk. Appl. Phys. 17, 85 (1978)

[73] A. Misra, J. P. Hirth, H. Kung. Phil. Mag. A 82, 2935 (2002)

[74] X. Han, N. M. Ghoniem. Phil. Mag. 85, 1205 (2005)

[75] A. Misra, J. P. Hirth, R.G. Hoagland. Acta Mater. 53, 4816 (2005)

[76] M. A. Phillips, B. B. Clemens, W. D. Nix. Acta Mater. 51, 3157 (2003)

[77] J. S. Koehler. Phys. Rev. B 15, 547 (1970)

[78] W. Mader, D. Knauss. Acta Metal. Mater. 40, 207 (1992)

[79] D. K. Satapathy, B. Jenichen, V. M. Kaganer, W. Braun, L.Daeweritz, K. H. Ploog. J. Vac. Sci. Technol. B 22, 2079 (2004)

[80] D. K. Satapathy, V. M. Kaganer, B. Jenichen, W. Braun, L.Daeweritz, K. H. Ploog. Phys. Rev. B 72, 155303 (2005)

[81] H. Okamoto. Binary alloy phase diagram. American society of metals, Metals Park, OH, USA, 1990

[82] B. T. M. Willis, H. P. Rooksby. Proc. Phys. Soc. London B 67, 290 (1954)

[83] T. W. Kim, H. S. Lee, J. Y. Lee, H. C. Jeon, T. W. Kang. J. Cryst. Growth 292, 62 (2006)

[84] V. H. Etgens, E. Eddrief, D. H. Mosca, M. Marangolo, J. M. George. J Mag. Mag. Mater. 226, 1577 (2001)

[85] L. Wan, J. Shangguan, H. Luo, Y. Huang, B. Tang. Eur. Phys. J: Appl. Phys. 38, 231 (2007)

[86] N. Mattoso, E. Eddrief, J. Varalda, A. Ouerghi, D. Demaille, V. H. Etgens. Phys. Rev. B. 70, 115324 (2004)

[87] M. Tanaka, K. Saito, T. Nishinaga. Appl. Phys. Lett. 74, 64 (1999)

[88] Y. Morishita, K. Iida, J. Abe, K. Sato. Japan. J. Appl. Phys. 36, 1100 (1997)

[89] M. Moreno, A. Trampert, B. Jenichen, L. Daeweritz, K. H. Ploog. J. Appl. Phys. 92, 4672 (2002)

[90] K. I. Cho, W. K. Choo, J. Y. Lee, S. C. Park, T. Nishinaga. J. Appl. Phys. 69, 237 (1991)

[91] D. Halley, Y. Samson, A. Marty, P. Bayle, C. Beigne, B. Gilles, J. E. Mazille. Phys. Rev. B. 65, 205408 (2002)

[92] W. Mader. Z. Metallkd. 83, 7 (1992)

[93] S. V. Kamat, J. P. Hirth, B. Carnahan. Mat. Res. Soc. Symp. Proc. 103, 55 (1988)

[94] M. Y. Gutkin, A. E. Romanov. Phys. Stat. Sol. (a), 144, 39 (1994)

[95] Caculated based on the elastic coefficients of MnAs (M. Doefler, K. Baerner. Phys. Stat. Sol. (a), 17, 141 (1973))

[96] L. A. Giannuzzi, P. R. Howell, H. W. Pickering, W. R. Bitler. J. Electron. Mater. 22, 639 (1993)

[97] L. A. Tietz, C. Barry Carter. J. Am. Ceram. Soc. 75, 1097 (1992)

[98] K. Rajan. Appl. Phys. Lett. 58, 287 (1991)

[99] Y. T. Chou, C. S. Pande, H. C. Yang. J. Appl. Phys. 46, 5 (1975)

[100] S. Sanvito, N. A. Hill. Phy. Rev. B 62, 15553 (2000)

[101] M. Ramsteiner, H. Y. Hao, A. Kawaharazuka, H. J. Zhu, M. Kaestner, R. Hey, L. Daeweritz, H. T. Grahn, K. H. Ploog. Phys. Rev. B 66, 081304 (2002)

[102] L. Allard, A. K. Datye, T. A. Nolan, S. L. Mahan, R. T. Paine. Ultramicroscopy 37, 153 (1991)

[103] Y. Ikuhara, P. Pirouz, S. Yadavalli, C. P. Flynn. Phil. Mag. A 72, 179 (1995)

[104] J. G. Zhu, S. Mckernan, C. J. Palmstrom, B. C. Carter. Mat. Res, Soc. Symp. Proc. USA, 1990

[105] A.D. Giddings, T. Jungwirth, B.L. Gallagher. Phys. Rev. B 78, 165312 (2008)

[106] E. Bauer. Z. Kristallogr. 110, 372 (1958)

[107] D. K. Satapathy. Ph.D thesis, Humboldt University, Berlin, Germany, 2005

[108] J. Sadowski, J. Kanski, L, Ilver, J. Johansson. Appl. Surf. Sci. 166, 247 (2000)

[109] F. Ernst, P. Pirouz. J. Appl. Phys. 64, 4526 (1988)

[110] Y.P. Lee, K.W. Kim, J.Y. Rhee, V. Yu, V. Kudryavtsev. Phys. Rev. B. 59, 546 (1999)

[111] R.N. Sacks, L. Qin, M. Jazwiecki, S. A. Ringle, M. B. Clevenger, D. Wilt, M. S. Goorsky. J. Vac. Sci. Technol. B 17, 1289 (1999)

[112] N. Maeda, M. Kawashima, Y. Horikoshi. J. Appl. Phys. 78, 6013 (1995).

[113] Q. F. Xiao, E. Brueck, Z. D. Zhang, F. R. de Boer, K. H. J. Buschow. Physica B 339, 228 (2003)

[114] N. I. Kulikov, A. V. Postnikov, G. Borstel, J. Braun. Phys. Rev. B 59, 6824 (1999)

[115] M. Tanaka, T. Nishinage, N. Ikarashi, H. Shimada. J. Appl. Phys. 75, 885 (1994)

[116] M. Tanaka, N. Ikarashi, H. Sakakibara, K. Ishida, T. Nishinage. Appl. Phys. Lett. 60, 835 (1992)

[117] W. D. Goodhue, H. Q. Le, G. D. Johnson, J. W. Bales. J. Vac. Sci. Technol. B 10, 783 (1992)

[118] P. Stadelmann. Electron microscopy image simulation, EPFL, Switzerland

[119] Y. Mishin, D. Farkas. Phil. Mag. A 75, 169 (1997)

[120] Y. Mishin, D. Farkas. Phil. Mag. A 75, 187 (1997)

[121] K. Selte, A. Kjekshus. Acta Chem. Scand. 25, 6 (1971)

[122] P. S. Lyman, C. T. Prewitt. Acta Crystallogr. Sec. B: Struc. Sci. 40, 14 (1984)

[123] G. Ayrault, G. Ehrlich. J. Chem, Phys. 60, 281 (1973)

[124] J. W. Cowly, A. F. Moodie. Acta Cryst. 10, 609 (1957)

[125] F. Birch. Phys. Rev. 71, 809 (1947)

[126] P. Paufler. Physikalische Kristallographie. Akademie-Verlag, Berlin, Germany, 1986

[127] http://www.veeco.com

List of Figures

List of Tables

Acknowledgments

First of all, I am thankful to Prof. Henning Richert for been given the opportunity to carry out my doctoral research at PDI.

I owe my deepest gratitude to Dr. Achim Trampert. Without your consistent help, encouragement and excellent guidance in the last four years, nothing in this work would have been possible.

I am grateful to Dr. Esperanza Luna for all the meaningful discussions about the research and critical comments on my papers. Your support and inspiring words when I was down really mean a lot to me.

I would like to thank Dr. Rudolf Hey and Mrs. Claudia Hermann for providing high-caliber samples for my investigations. Fruitful discussions with Dr. Hey are also appreciated.

It is my pleasure to thank Mr. Jonas Berggren, my officemate and birthday buddy. Thank you for being my translator for such a long time, even in most cases being "forced". Thank you for the friendship, for all the sharing and encouragement. Hey, we finally did it.

I am indebted to many of my colleagues who support me: Dr. Uwe Jahn, Dr. Biswarup Satpati, Mr. Hartmut von Kiedrowski, Mrs. Astrid Pfeiffer, Dr. Rocío Ranchal, Ms. Marlene Zander, Mr. Steffen Breuer. Life becomes much easier for me because of all of you.

I would also like to thank the Chinese community in our institute: Dr. Lifeng Bian, Dr. Shujie Jiao, Dr. Guofang Fan, Dr. Cunxu Gao, Dr. Jiansu Yang, Dr. Kwang-Ru Wang, Dr. Chang-Ning, Huang, Dr. Xiang Kong and Mr. Mingjian Wu. The parties and gossips just made my days here a little bit less boring.

I want to express my gratitude to my parents: Weijin Wan and Jiannong Zhou. Your continuous caring and support have proved to be extraordinarily valuable for me. Finally, I would like to express my deepest love to my girlfriend: Yuan Ran. Thank you for your understanding and your patience. Without your unfailing love, I would have never survived. This work is dedicated to you.

Part of this work have already been published

R. Hey, U. Jahn, **Q. Wan**, A. Trampert. *Quantum well and cavity structures grown on (110) GaAs by MBE.* Phys. Stat. Sol. (c) **5**, 2917 (2008)

Q. Wan, R. Hey, A. Trampert. *Local disordering in epitaxially strained CoAl films grown on GaAs (001).* J. Appl. Phys. **108**, 033518 (2010)

Q. Wan, R. Hey, A. Trampert. *Atomic ordering in intermetallic CoAl alloys epitaxially grown on GaAs (001).* Proceedings of the 16th International Conference on Microscopy of Semiconducting Materials, Oxford (UK) 2009. J. Phys.:Conf. Ser. **209**, 012023 (2010)

Q. Wan, A. Trampert. *Atomic configuration of the MnAs/GaAs (110) interface analyzed by high-resolution electron microscopy.* J. Phys. Chem. C **115**, 529 (2011)

Berlin, den April 23, 2014 Qian Wan

Selbständigkeitserklärung

Hiermit erkläre ich, die vorliegende Arbeit selbständig ohne fremde Hilfe verfaßt und nur die angegebene Literatur und Hilfsmittel verwendet zu haben.

Ich habe mich an keiner anderen Universität um einen Doktorsgrad beworben und besitze auch keinen entsprechenden Doktorsgrad.

Ich erkläre die Kenntnis der dem Verfahren zugrunde liegenden Promotionsordnung der Mathematisch-Naturwissenschaftlichen Fakultät I der Humboldt-Universität zu Berlin.

Berlin, den April 23, 2014 Qian Wan